# Realistic MHD simulations of spots on cool main-sequence stars

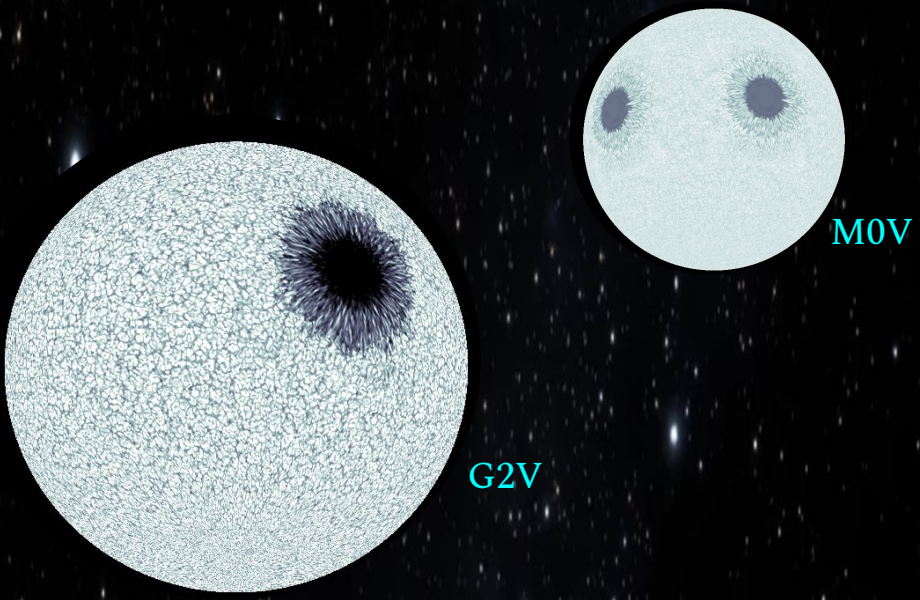


Mayukh Panja

International Max Planck Research School
for Solar System Science
at the University of Göttingen

# Realistic MHD simulations of spots on cool main-sequence stars

Dissertation
zur Erlangung des mathematisch-naturwissenschaftlichen Doktorgrades

"Doctor rerum naturalium"

der Georg-August-Universität Göttingen

im Promotionsstudiengang Physik
der Georg-August University School of Science (GAUSS)

vorgelegt von

**Mayukh Panja**

aus Kolkata, India

Göttingen, 2020

Betreuungsausschuss

Prof. Dr. Sami K. Solanki
Max-Planck-Institut für Sonnensystemforschung, Göttingen, Germany

Prof. Dr. Laurent Gizon
Institut für Astrophysik, Georg-August-Universität Göttingen, Germany

Dr. Robert Cameron
Max-Planck-Institut für Sonnensystemforschung, Göttingen, Germany

Mitglieder der Prüfungskommision

Referent: Prof. Dr. Sami K. Solanki
Max-Planck-Institut für Sonnensystemforschung, Göttingen, Germany

Korreferent: Prof. Dr. Ansgar Reiners
Institut für Astrophysik, Georg-August-Universität Göttingen, Germany

Weitere Mitglieder der Prüfungskommission:

Prof. Dr. Hardi Peter
Max-Planck-Institut für Sonnensystemforschung, Göttingen, Germany

Dr. Natalie Krivova
Max-Planck-Institut für Sonnensystemforschung, Göttingen, Germany

Prof. Dr. Laurent Gizon
Institut für Astrophysik, Georg-August-Universität Göttingen, Germany

Prof. Dr. Ariane Frey
Physikalisches Institut, Georg-August-Universität Göttingen, Germany

Tag der mündlichen Prüfung: 11-12-2020

**Bibliografische Information der Deutschen Nationalbibliothek**

Die Deutsche Nationalbibliothek verzeichnet diese Publikation in der Deutschen Nationalbibliografie; detaillierte bibliografische Daten sind im Internet über `http://dnb.d-nb.de` abrufbar.



Printed in Germany

**Cover Image:** Intensity images of starspots and quiet star regions generated from the radiative MHD simulations presented in this thesis, patched together and wrapped around a spherical surface to create artificial images of stellar surfaces. The limb darkening effect has not been included in these images.

# Contents

# Prologue

What does a star look like? Given that the observable universe is estimated to have roughly $10^{11}$ galaxies, each of which is populated by $10^{11}$ stars, this fundamental astrophysics question is surprisingly difficult to answer. The sheer vastness of space limits what we can see and the most powerful of telescopes have been able to resolve the surface features of just one star - the Sun. Luckily, the Sun is close enough to be observed to a high degree of detail and decades of thorough observations have revealed that a stellar surface can harbour a myriad of magnetic features spanning a wide range of length and timescales - tiny bright points that last a few minutes to giant dark spots that survive an entire rotational period. Unfortunately, for other stars the only existing approach to glean any information is to solve difficult inverse problems that often rely on apriori assumptions. This means, we have, at best, uncertain information about their large scale structures. Even the most conspicuous of solar features, its dark spots, observed since the invention of the telescope, have not been directly observed on other stars. Naturally, computer models that solve the equations of radiation magnetohydrodynamics, which allow us to artificially mimic the physical conditions of the outer layers of different types of stars, have proved to be extremely useful. Such models have been used, not only to reproduce and provide physical explanations for many of the observed features on the Sun, but to also simulate the small scale magnetic and hydrodynamic features of other stars. However, the simulation of magnetic spots on stars other than the Sun is territory that is yet to be charted. In this thesis, I compute the first simulations of spots on other stars and present a unified theory connecting the thermodynamic and radiative properties of magnetic spots on cool main-sequence stars.

# Summary

Sunspots are cool, dark features on the solar surface consisting of two distinct parts - the inner dark umbra and its surrounding brighter, filamentary penumbra. Strong nearly vertical fields found in the umbra locally suppress overturning convective motion while the more inclined fields of the penumbra support the outward Evershed flow. The fine structure of sunspots has been studied in much detail with the help of both ground and space-based telescopes.

Our knowledge about starspots, in comparison, is very limited. This is mainly because other stellar surfaces are at best poorly resolved. Nonetheless, inversions of lightcurves and in particular of spectropolarimetric time series have allowed us to map the large scale temperature and magnetic field in-homogeneities on other stars. However, the derived properties of spots on stars very similar to the Sun display strong differences to sunspots, suggesting that the properties of starspots derived from stellar observations may not be so reliable. The fine structure of starspots is still unknown and how similar, or dissimilar, they are to spots on the Sun remains to be answered. In this thesis, we have attempted to make headway into these unsolved astrophysical problems.

In **Chapter 1**, I have briefly covered the existing body of knowledge on the photospheric physics of different types of stars, sunspots and spots on other stars. I have also described the MURaM code which has been used for the radiative MHD computations presented in this thesis.

In **Chapter 2**, I have presented the first-ever, realistic simulations of the photospheric structure of starspots for a range of cool main-sequence stars, namely the spectral types-M0V, K0V, and G2V. I explored several fundamental properties like umbral intensity contrast, temperature, and magnetic field strength as functions of spectral type. The simulations show that there is an increase in spot contrast with the increase in stellar surface temperature, which is consistent with observations. The umbral field strength is determined by the depth at which the optical surface forms and the surface pressures of the host stars and it depends much less strongly on spectral type. I discussed in detail the physics behind the trends seen in temperature and magnetic field.

In **Chapter 3**, I synthesized three spectral lines from the simulated starspot atmospheres - two in the visible and another in the infrared wavelength. I then studied the center-to-limb variations of the emergent spectra. I combined synthetic line profiles of umbrae, penumbrae, and quiet star regions calculated at various viewing angles to create disk integrated line profiles which were used to estimate the effects of spots on stellar radial velocity.

While constraining the initial conditions for our starspot simulations presented in Chapter 2, I found that interchange instabilities were affecting some of the magnetic flux tubes. In **Chapter 4**, I present the results of a detailed, separate study on this. I performed

numerical experiments with magnetic flux tubes of different curvatures and tested their susceptibility to the fluting instability. I found that the subsurface structure of sunspot flux tubes play a role in penumbra formation and flux tubes which are highly curved tend to be more vulnerable to penetration by flute-like intrusions of the surrounding gas.

Finally in **Chapter 5**, I have summarized the main conclusions of this thesis and discussed future directions of research the work in thesis has opened up.

# Zusammenfassung

Sonnenflecken sind kühle, dunkle Stellen auf der Sonnenoberfläche, die aus zwei verschiedenen Teilen bestehen, der inneren dunklen Umbra und der umgebenden, aus helleren Filamenten gebildeten Penumbra. Starke, vorwiegend vertikale Felder in der Umbra unterdrücken lokal die Konvektion, während die stärker geneigten Felder in der Penumbra den nach außen gerichteten Evershed-Fluss unterstützen. Die Feinstruktur der Sonnenflecken wurde mit Hilfe von bodengebundenen und weltraumgestützten Teleskopen eingehend untersucht.

Unser Wissen über Sternflecken ist im Vergleich dazu sehr begrenzt. Dies liegt hauptsächlich daran, dass die Oberflächen anderer Sterne sehr schwer aufzulösen sind. Inversionen von Lichtkurven und spektropolarimetrische Daten haben es uns jedoch ermöglicht, die großskaligen Inhomogenitäten von Temperatur und Magnetfeld auf anderen Sternen abzubilden. Die Feinstruktur von Sternflecken ist noch unbekannt und wie ähnlich oder unähnlich sie Flecken auf der Sonne sind, ist noch nicht beantwortet. In dieser Arbeit haben ich versucht, Fortschritte bei der Lösung dieser herausragenden astrophysikalischen Probleme zu machen.

In **Kapitel 1** gehe ich kurz auf den aktuellen Wissensstand über die Physik der Photosphäre verschiedener Arten von Sternen, Sonnenflecken und Flecken auf anderen Sternen ein. Ich beschreibe auch den MURaM-Code, der für die in dieser Arbeit präsentierten Strahlungs-MHD-Simulationen verwendet wurde.

In **Kapitel 2** stelle ich die ersten realistischen Simulationen der photo- sphärischen Struktur von Sternflecken für eine Reihe kühler Hauptreihensterne vor, nämlich die Spektraltypen M0V, K0V und G2V. Ich untersuche verschiedene grundlegende Eigenschaften, wie den Intensitätskontrast der Umbra, die Temperatur und die Magnetfeldstärke, als Funktionen des Spektraltyps. Die Simulationen zeigen, dass der Kontrast der Flecken mit steigender Temperatur der Sternoberfläche zunimmt, was mit den Beobachtungen übereinstimmt. Die Feldstärke der Umbra wird bestimmt durch die Tiefe, an der sich die optische Oberfläche gebildet wird, und durch den Druck an der Oberfläche der betreffenden Sterne. Ich diskutiere ausführlich die physikalischen Prozesse, welche für die Trends in Temperatur und Magnetfeld verantwortlich sind.

In **Kapitel 3** synthetisiere ich zwei Spektrallinien aus unseren simulierten Sternflecken-Atmosphären - eine im sichtbaren, die andere im infraroten Wellenlängenbereich. Ferner untersuche ich die Variation der erhaltenen Spektren vom Zentrum bis zum Rand der Sternscheibe. Ich kombiniere synthetische Linienprofile für Umbrae, Penumbrae und ruhige Sternregionen, die unter verschiedenen Beobachtungswinkeln berechnet wurden, zu integrierten Linienprofilen, mit denen ich die Auswirkungen von Flecken auf die stellaren Radialgeschwindigkeiten abschätzen kann.

Während wir die Anfangsbedingungen für unsere in Kapitel 2 vorgestellten Stern-

fleckensimulationen bestimmten, stellten wir fest, dass einige der magnetis- chen Flussröhren von der Austauschinstabilität (fluting instability, oder interchange instability) beeinflusst werden. In **Kapitel 4** führen wir dazu eine detaillierte, separate Studie durch. Ic führe numerische Experimente mit magnetischen Flussröhren unterschiedlicher Krümmung durch und testen deren Anfälligkeit für die Austauschinstabilität. Wir stellen fest, dass die Struktur der Flussröhren der Sonnenflecken unter der Oberfläche eine Rolle bei der Entstehung der Penumbrae spielt, außerdem sind stark gekrümmte Flussröhren anfälliger für das rillenartige Eindringen des umgebenden Gases.

Abschließend fasse ich in **Kapitel 5** die wichtigsten Schlussfolgerungen dieser Arbeit zusammen und erörtere zukünftige Forschungsrichtungen, welche durch die Arbeit in dieser Dissertation eröffnet werden.

# 1 Introduction

The work presented in this thesis explores the thermodynamic, radiative and magnetic properties of spots on stars of different spectral types on the main-sequence, through numerical radiative magnetohydrodynamic (MHD) simulations. However, before a discussion of the simulations of starspots performed in this thesis ensues, the following questions, which provide the backdrop of this work, must be addressed -

1) How are stars classified into spectral types? What is the main-sequence? (Section 1.1)

2) Starspots are manifestations of concentrated magnetic fields embedded in granular convection. What drives granular convection? How does a star's spectral type affect the hydrodynamics of granular convection? (Section 1.2)

3) How does magnetic field affect granulation? What have we learned from past simulations of stellar surfaces that included magnetic fields? (Section 1.3)

4) What do we know about the fundamental properties of sunspots and spots on other stars? (Section 1.4)

I will begin with a discussion of the different spectral types stars are classified into, and the Hertzsprung-Russell (HR) diagram - concepts that will be frequently invoked in this chapter.

## 1.1 Classification of stars - The HR Diagram

Stars are giant luminous balls of gas that are bound together by their own gravity. Their luminosity is powered by nuclear reactions at their core, that were triggered by a gravitational collapse creating extreme conditions of temperature and pressure. The luminosity ($L$) of a star with radius $R$ is given by,

$$L = (4\pi R^2)\sigma T_{eff}^4, \tag{1.1}$$

where $T_{eff}$ is the temperature of the star if it were to radiate like a blackbody and $\sigma$ is the Stefan-Boltzmann's constant.

Luminosity and $T_{eff}$ are both measurable quantities and in an effort to better understand stellar evolution, luminosity is often plotted against $T_{eff}$ in what is known as the Hertzsprung-Russell (HR) diagram, as shown in Figure 1.1. Stars are also grouped into

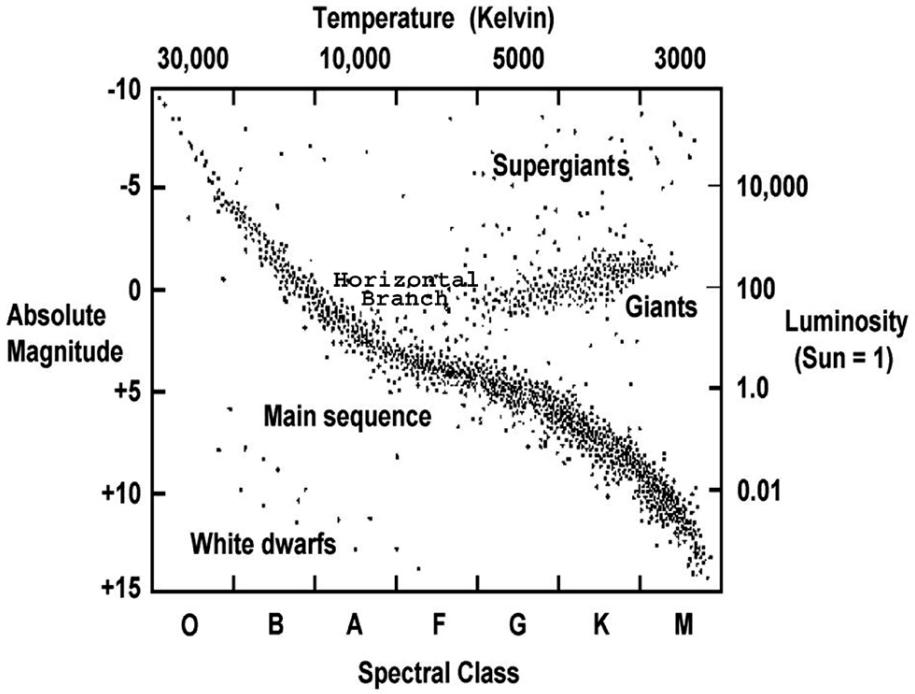


Figure 1.1: Hertzsprung-Russell (HR) diagram, with each point representing a separate star. In this thesis, we are concerned with the spectral types G, K and M that lie on the main-sequence. Image source: chandra.harvard.edu/edu/formal/variable_stars/bg_info.html

spectral types in accordance with the Morgan-Keenan system, in which they are assigned a temperature class and a luminosity class, based on the characteristics of their spectral lines. In this system, the temperature class of a star is determined by the strength of its absorption lines, while the pressure broadening (a high surface pressure would be caused by a high surface gravity, which is related its size) of its spectral lines is used to assign it a luminosity class. For example, the Sun is a G2V star, where G indicates a broad temperature range of roughly 5000 - 6000 K, and 2 indicates its sub-temperature group. It has a luminosity class of V, which tells us it is in the main-sequence. A star's spectral type, naturally, is also indicative of its position in the HR diagram. A position of a star on the HR diagram tells us much more than just its luminosity and temperature; it reveals information about its mass, size, internal structure and stage of its life. A casual look at eqn. 1.1 tells us that a cold and luminous star will have a much larger radius than a warmer but fainter star. It is also a star's mass that determines the gravitational force it exerts on itself, and through much of its lifetime, a star is kept in equilibrium by the competing forces of its own gravity and the thermal and radiation pressure created by the nuclear reactions at its core that also make it luminous. One can derive, starting from the stellar structure equations, simple scaling laws that relate the mass ($M$), radius ($R$), luminosity ($L$) and internal temperature ($T_{\text{Internal}}$)of a star. This exercise, which involves a series of radical assumptions, yields the following approximate relations for a star (see Appendix A: for a full derivation)

$$T_{\text{Internal}} \propto \frac{M}{R}, \tag{1.2}$$

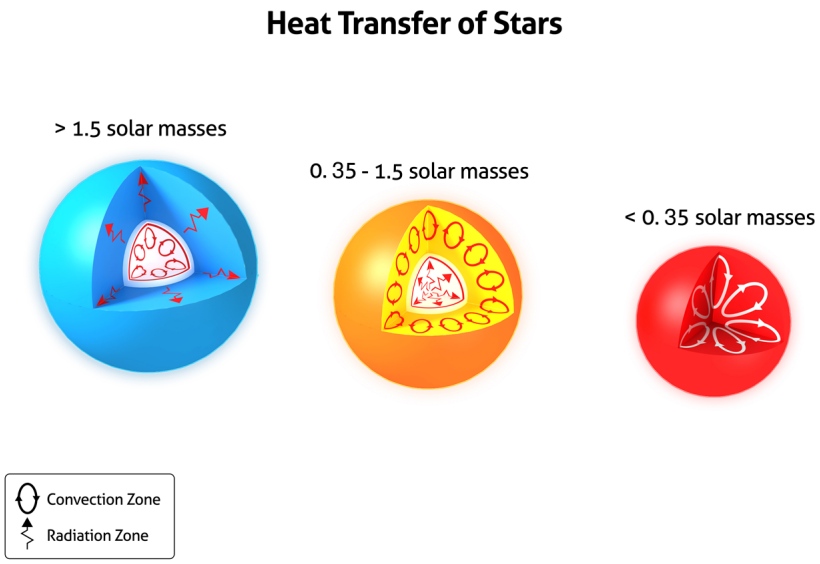


Figure 1.2: Mode of heat transport in stars with stellar mass. Image adapted from: www.sun.org - http://www.sun.org/encyclopedia/stars, CC BY-SA 3.0

and

$$L \propto M^3 \text{.}^* \tag{1.3}$$

The stars discussed in this thesis have internal temperatures in the same order-of-magnitude and therefore eqn. 1.2 can be further simplified to a better approximation for cool main sequence stars:

$$M \propto R. \tag{1.4}$$

As one can see, the mass and size of a star are intimately connected to its internal temperature and luminosity. The mass of a star also critically decides its structure and evolution, which I will proceed to illustrate, in broad terms, in the following paragraphs.

A star is born when a gravitational instability in the protostellar cloud causes mass to lump together, which triggers further accumulation of mass. As the star contracts under its own mass, the gravitational energy heats up the star. For stars that exceed a certain mass threshold, this process continues until the core reaches the temperature and pressure to support nuclear fusion which converts hydrogen into helium. Now the star has enough radiation pressure to counteract its own gravity and this stable luminous ball of gas is a part of the main-sequence. A star spends a significant portion of its life in the main-sequence. Once a star is depleted of its hydrogen, its core contracts under its own weight, until the temperature and pressure are high enough that nuclear fusion, "burning" hydrogen, restarts in a shell surrounding its core. The increased radiation pressure expands its

*This is a relation derived purely theoretically using order of magnitude approximations to demonstrate the intimate connection between $L$ and $M$. In reality, $L \propto M^{\alpha}$, where $\alpha$ is a piecewise step function of the mass of the star. Mass-luminosity relations derived empirically (Demircan and Kahraman 1991) and calculated from observations (Griffiths et al. 1988, Eker et al. 2015) place $\alpha$ between 2.4 and 4.8 (see Table 1 of Wang and Zhong (2018)). It is interesting that despite the simplistic nature of the derivation, the obtained value of $\alpha = 3$ lies well within the range of observed values.

outer layer and the star enters the red-giant phase of its life cycle. Depending on the star's mass, it either meets it end through an explosive supernova or throws off most of its outer shell in the form of a strong wind and then cools down to a white dwarf.

A vast majority ($\approx$ 90%) of the stars in the observable universe lie on the main-sequence, a narrow diagonal band, stretching from the top left corner to the bottom right corner of the HR diagram. As we move up along the main-sequence we sample stars of increasingly larger radii and larger masses. A main-sequence star has a core that converts hydrogen into helium by nuclear fusion. As illustrated in Figure 1.2, the mode of transport of this generated energy depends, again, on the stellar mass. Stars with low mass ($< 0.35 M_\odot$) are fully convective (Chabrier and Baraffe 1997), while stars with mass in the range $0.35 M_\odot - 1.5 M_\odot$ have an inner radiative zone and an outer convective zone. Stars heavier than $1.5 M_\odot$ have an inner convective zone and an outer radiative zone.

In this thesis, we are concerned with the spectral types G2V, K0V, and M0V. All of them have masses in the range $0.35 M_\odot$ to $1.5 M_\odot$ and therefore they have outer convective zones. They have comparable surface gravities and their surface temperatures lie in the range 4000 - 6000 K. I will discuss next, the surface layers of these stars, where the convection zone meets the outermost radiating layer, with a particular focus on granular convection and how its properties vary with spectral type. It is important to note that in all of the discussions that will follow, it will be assumed that matter is in thermodynamic equilibrium. For a very entertaining explanation of what thermodynamic equilibrium is and to witness in vivid imagery what happens at the atomic level inside a star, I implore you to read the excerpt provided in the next page, from *"The internal constitution of stars."* by Eddington (1930).

## 1.2 Granular Convection

This thesis is an improvement upon previous simulations that studied stellar granular convection and small scale magnetic features embedded in granules. It is therefore, imperative that I discuss the theoretical aspects of near surface convection in stars and previous work that provides the framework for this thesis.

Convection is a mode of energy transport where the motion of fluid parcels itself transports heat energy. In a gravitationally stratified stellar atmosphere, for convection to set in, the vertical gradient in temperature must be greater than the adiabatic temperature gradient.

$$\frac{\partial T}{\partial z} > \frac{\partial T}{\partial z}_{adiabatic}. \tag{1.5}$$

What does it mean when an atmosphere is said to be adiabatically stratified ? Imagine a parcel of gas sitting at the bottom of the convection zone, slightly hotter than its surroundings. By virtue of being hotter it will be less dense than the background and naturally buoyant. As it rises up through the stratified stellar interior, this parcel of gas encounters an increasingly vacuous background and expands as its higher internal pres-

*The Inside of a Star.*

17. The inside of a star is a hurly-burly of atoms, electrons and aether waves. We have to call to aid the most recent discoveries of atomic physics to follow the intricacies of the dance. We started to explore the inside of a star; we soon find ourselves exploring the inside of an atom. Try to picture the tumult! Dishevelled atoms tear along at 50 miles a second with only a few tatters left of their elaborate cloaks of electrons torn from them in the scrimmage. The lost electrons are speeding a hundred times faster to find new resting-places. Look out! there is nearly a collision as an electron approaches an atomic nucleus; but putting on speed it sweeps round it in a sharp curve. A thousand narrow shaves happen to the electron in $10^{-10}$ of a second; sometimes there is a side-slip at the curve, but the electron still goes on with increased or decreased energy. Then comes a worse slip than usual; the electron is fairly caught and attached to the atom, and its career of freedom is at an end. But only for an instant. Barely has the atom arranged the new scalp on its girdle when a quantum of aether waves runs into it. With a great explosion the electron is off again for further adventures. Elsewhere two of the atoms are meeting full tilt and rebounding, with further disaster to their scanty remains of vesture.

As we watch the scene we ask ourselves, Can this be the stately drama of stellar evolution? It is more like the jolly crockery-smashing turn of a music-hall. The knockabout comedy of atomic physics is not very considerate towards our aesthetic ideals; but it is all a question of time-scale. The motions of the electrons are as harmonious as those of the stars but in a different scale of space and time, and the music of the spheres is being played on a keyboard 50 octaves higher. To recover this elegance we must slow down the action, or alternatively accelerate our own wits; just as the slow-motion film resolves the lusty blows of the prize-fighter into movements of extreme grace—and insipidity.

And what is the result of all this bustle? Very little. Unless we have in mind an extremely long stretch of time the general state of the star remains steady. Just as many atoms are repaired as are smashed; just as many bundles of radiation are sent out as are absorbed; just as many electrons are captured as are exploded away. The atoms and the electrons for all their hurry never get anywhere; they only change places. The aether waves are the only part of the population which do actually accomplish something; although apparently darting about in all directions without purpose they do in spite of themselves make a slow general progress outwards.

(Eddington 1930, pp. 19 – 20).

Figure 1.3: Excerpt from Arthur Eddington's "The internal constitution of stars"

sure tries to adjust to the constantly thinning environment around it. If we assume that the journey of this parcel has been adiabatic, that is, it did not exchange any heat with it surroundings, the cooling of the gas inside the parcel will be strictly from the loss of pressure. Let us consider the case, where the surrounding gas at the new elevation of the parcel is cooler than the gas inside the parcel. The parcel would be still hotter and less dense than its surroundings and would continue to rise. This would be possible, only if the vertical gradient in temperature of the background medium is steeper than the adiabatic drop in temperature inside the parcel. This has been expressed mathematically in eqn. 1.5.

It is often convenient to state the criterion for convection in terms of entropy. Entropy

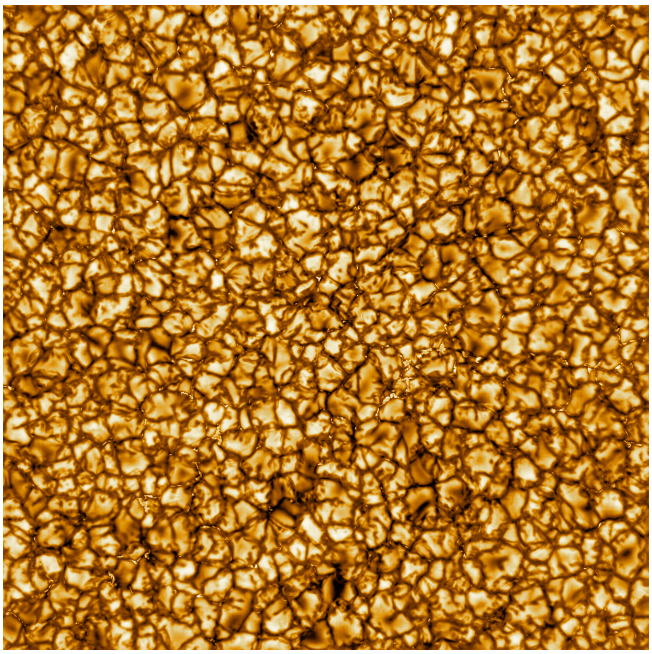

Figure 1.4: An image of the solar surface taken at a resolution of 30km by the Daniel K. Inouye Solar Telescope (DKIST).

is a state function which is defined in classical thermodynamics as:

$$dS = \frac{dQ}{T}, \tag{1.6}$$

where dQ is the amount of heat energy absorbed or expended by the system, and T the temperature. Naturally any adiabatic system, in this case, our parcel of gas rising through the atmosphere, is also isentropic as its cooling is solely due to the drop in pressure and not mediated through an exchange of energy with its surroundings ($dQ = 0$). For a system that is superadiabatic, the change in entropy will naturally be non-zero, and the convective instability criterion can be formulated as

$$\frac{dS}{dz} < 0. \tag{1.7}$$

It is advantageous to restate the criterion for convection in terms of entropy because any heat exchange a parcel of gas lives through, leaves an imprint on its entropy. For example, once our gaseous blob reaches the stellar surface and "sees the universe", it loses heat energy through radiation and therefore loses some its entropy.

Convection in a star occurs over multiple length scales, the largest being the global mode while the smallest scale manifests in the surface layers, in the form of granules. Granules, as shown in Figure 1.4, are bright cells of buoyant hot gas, bordered by dark lanes where the gas, after cooling off, sinks back into the star. The thin layer, where radiative cooling takes place, induces a sharp vertical gradient in entropy and drives the near-surface, vigorous convection. Further the departure from adiabaticity, or sharper the gradient in entropy, more vigorous is the convection.

The characteristic length scale of granules and their velocities can be estimated from simple first principle calculations (see Nordlund et al. (2009) for a more detailed discussion). Since the size of granules should be congruent with mass conservation, it is reasonable to expect that the horizontal extent of granules should be dependent on the vertical length scale over which thermodynamic properties change, that is the average pressure scale height ($H_p$) near the surface. The pressure scale height is given by

$$H_p = \frac{P}{\rho g}.$$

Using the arguments above and invoking the ideal gas law, we can write

$$\text{granule size} \propto \frac{T}{g}. \tag{1.8}$$

This means as we as we go deeper into a star, the size of granules increases, with increasing temperature. As we move from the left to right on the HR diagram along the main-sequence (which I do in this thesis) we witness a decrease in surface temperature and an increase in surface gravity. This would mean granules would become monotonically smaller from the G2V star to the M0V star.

Another conspicuous property of granules, is their temperature contrast, that is the temperature difference between upflows and downflows. From mixing-length theory the amount of heat energy transported upwards ($F_{\text{conv}}$) by a unit volume of fluid can be approximated as:

$$F_{conv} \approx \rho c_p (T_{up} v_{up} - T_{dn} v_{dn}). \tag{1.9}$$

Here $\rho$ is the density, $c_{\text{p}}$ is the specific heat capacity at constant pressure, $T_{\text{up}}$ and $T_{\text{dn}}$ are the temperatures of the upflowing and downflowing plasma respectively, and $v_{\text{up}}$ and $v_{\text{dn}}$ are the upflow and downflow velocities. Assuming that $v_{up}$ and $v_{dn}$ are of the same order of magnitude, one can replace these terms by $v_{vert}$ and rewrite eqn. 1.9 as,

$$F_{conv} \approx \rho c_p v_{vert} (T_{up} - T_{dn}). \tag{1.10}$$

Now, all of the net energy that is carried up by convection must be radiated away. Therefore we can write,

$$\rho c_p v_{vert} (T_{up} - T_{dn}) \approx \sigma T_{eff}^4,$$

or,

$$v_{vert} (T_{up} - T_{dn}) \propto \frac{T_{eff}^4}{\rho}. \tag{1.11}$$

This result has powerful predictive abilities. Let us look at the stars we are concerned with - G2V, K0V and M0V. $T_{eff}$ decreases from the G2V to the M0V star, while $\rho$ increases. This means the product of granule velocity and temperature contrast would be the highest in the G2V case and lowest in the M0V case.

Although these arguments are very simplistic, they are useful in developing a qualitative understanding of granular convection across the HR diagram. For a thorough quantitative analysis, one must resort to numerical simulations, the history of which I will

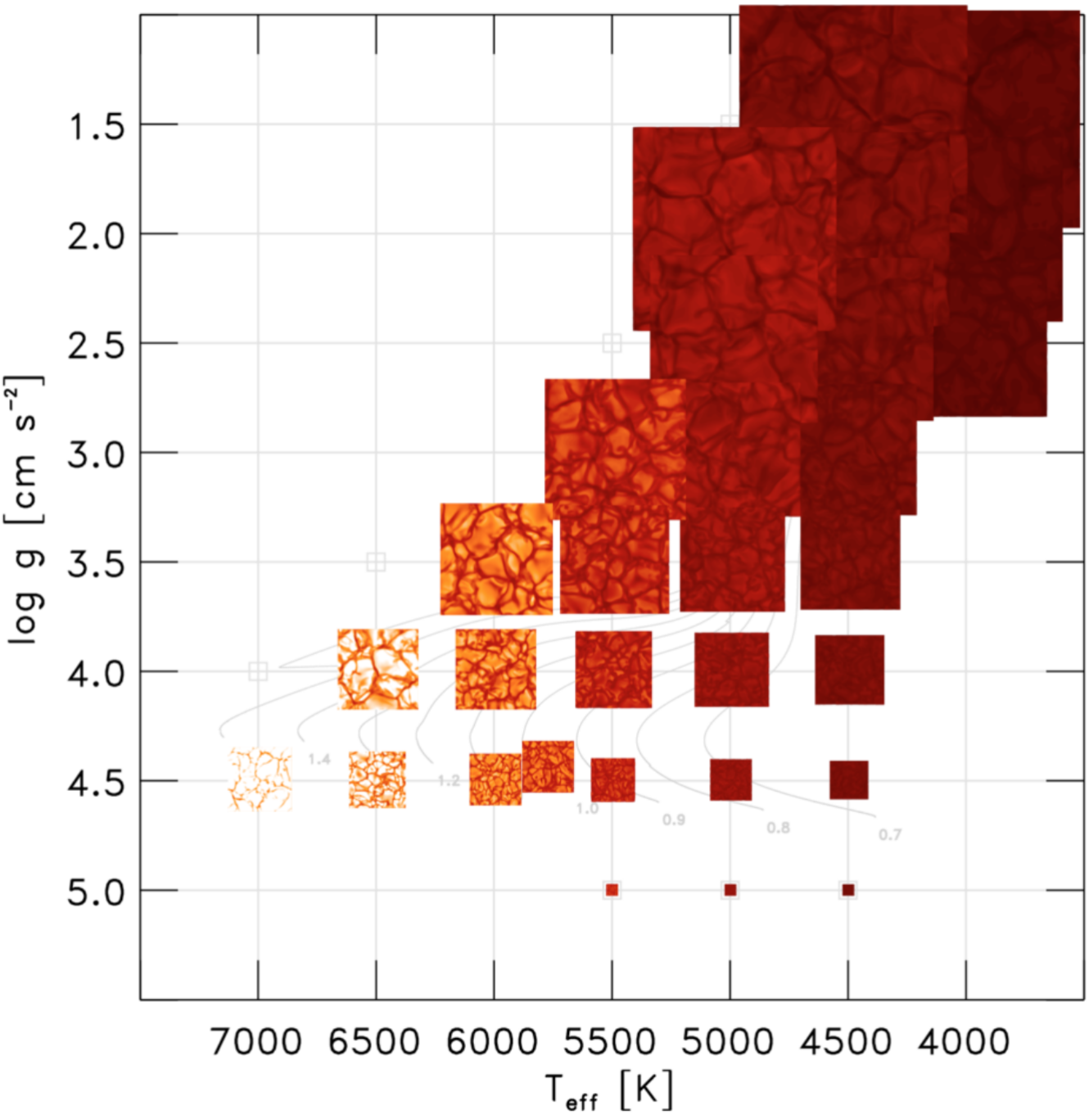


Figure 1.5: White-light intensity images of granulation across the HR diagram. The grey lines show evolutionary tracks for different stellar masses. Image created by Zazralt Magic with the STAGGER code.

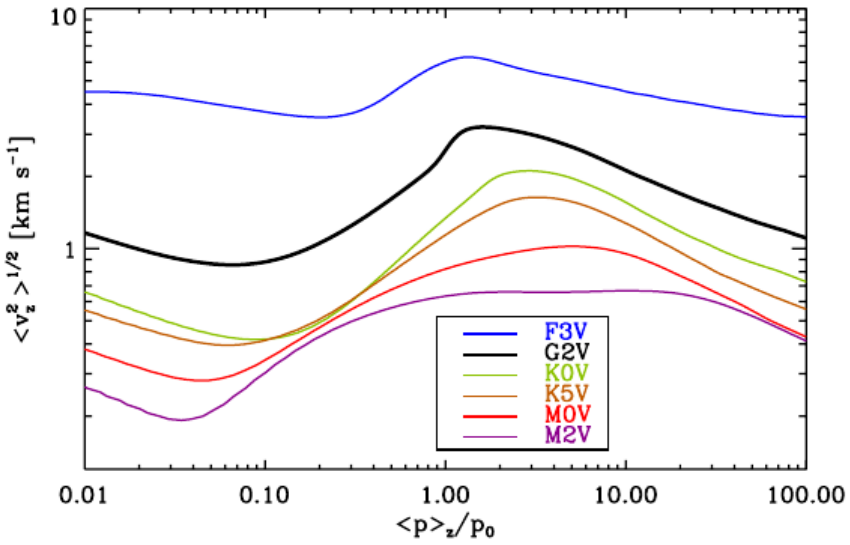


Figure 1.6: R.M.S (Root mean square) of the vertical component of the flow velocity on surfaces of constant geometrical depth, plotted against normalized pressure, for different spectral types. This figure is a reproduction of Figure 6a of Beeck et al. (2013a). Credit: Beeck et al. 2013, A&A, 558, A48, reproduced with permission ©ESO

briefly present in the following paragraphs.

The first simulations of a stellar surface were of the Sun's granulation, computed in the early 1980s by Nordlund (1982, 1984, 1985). These early simulations, despite the limited computing resources available at the time, provided crucial insight into photospheric physics and their effect on spectral lines. Soon after, Nordlund and Dravins (1990b) extended their solar simulations to other sun-like stars. This seminal work produced the first images of stellar surface granulation and established the role of temperature dependence of opacity in shaping stellar granular structure. The continuum opacity of cool main-sequence stars is governed by $H^-$ opacity and in the temperature range 4000 - 8000 K , the opacity ($\kappa$) scales as $T^9$. This means the variation of opacity with depth would be strongly dependent on the surface temperature of the star, and as a consequence the thickness of the radiative cooling layer, which is the driver of near surface convection, would also vary with spectral type. In hot F stars, the cooling occurs over a very thin slice and as a result the highest temperature contrast is close to the surface. Such hot stars exhibit "naked" granules, while in cooler stars, where the radiative cooling is spread out over a larger vertical extent, the granulation is "veiled" granulation with the highest temperature contrast of the granules being reached underneath the visible surface.

Since then, a few other radiative magnetohydrodynamic (rad-MHD, henceforth) codes - Co5BOLD (Freytag et al. 2012), STAGGER (Stein and Nordlund 1998, Magic et al. 2013a, Trampedach et al. 2013), MURaM (Vögler et al. 2005, Rempel et al. 2009b, Beeck et al. 2013a,b) and Stellar-Box (Wray et al. 2015), have been used to perform stellar surface simulations on different spectral types. It was shown by Beeck et al. (2012) that the Co5BOLD, STAGGER, and MURaM codes, despite their differences in numerical

approaches, exhibit overall similar behaviour.

These independent investigations have led to an emergence of a cohesive picture of stellar granulation. In Figure 1.5 (image created by Zazralt Magic using the STAGGER code), the variation of emergent white-light intensity across the HR diagram is shown. The most visible feature of granular convection - granule size, is indeed determined by the competing effects of surface temperature and surface gravity as predicted by equation 1.8. An increase in log g results in smaller granules whereas an increase in $T_{eff}$ increases granule sizes. This creates an interesting scenario for red giants ($T_{eff}$ - 4000 - 4500 K, log g - 1.5 - 2.0), where despite their low temperatures, they have massive granules (comparable to the stellar radius!) because of the drastic reduction in log g. The contrast between granules and intergranular lanes is also a function of $T_{eff}$. Higher the stellar temperature, higher is the contrast, confirming the very early results of Nordlund and Dravins (1990b). In Figure 1.6 (image taken from Beeck et al. (2013a)), the variation of upflow speeds with depths, for different spectral types are shown. There are three important takeaways from this plot -

1) The upflow speeds show a monotonic decrease from the hottest (F3V) to the coolest star (M2V). Given that temperature contrast also reduces from F3V to M2V, note that the relation given in equation 1.11, despite its simplicity, turns out to be quite useful.

2) For every spectral type, the upflow speeds reach a peak and then gradually become slower as we move deeper down. However the sharpness of the peaks varies with spectral type, with the sharpness gradually decreasing from F3V to M2V.

3)The maximum speed is reached at different depths. For the F3V star it is at the surface, whereas for the colder M0V star it is at a depth where the pressure is 10 times that of the surface. This and the point discussed above, is related to the vertical extent of the layer over which radiative cooling takes place, which is again, as discussed before, determined by the temperature dependence of opacity.

In this section I have discussed in detail how stellar near-surface convective properties vary with spectral type. The following section will be a discussion of what happens when we throw magnetic fields into the mix.

## 1.3 Small-scale magnetic fields

Needless to say, it is, at present, impossible to observe small-scale ($< or \approx$ granular lengthscales) magnetic features on stars other than the Sun. However, it is possible to study their collective effect from disk-integrated spectra. Therefore, when we talk about magnetic fields on other stars, we often associate it with a filling factor which tells us how much of the disk surface is covered by magnetic field. I have described some of the difficulties of measuring magnetic fields in the Introduction of Paper - I, later in this thesis. For a detailed review of stellar magnetic field measurement techniques see the reviews by Berdyugina (2005) and Reiners (2012).

However, I will focus my discussions on how individual small-scale magnetic flux tubes interact with convection and radiation. This is important because I later make the assumption that starspots are essentially large magnetic flux tubes that are embedded in stellar photospheres. Therefore, many of the results that came out of previous studies

where smaller magnetic flux tubes interacted with granular convection and radiation, are relevant and applicable to the work presented in this thesis.

Magnetic flux tubes have two effects on the plasma they are embedded in - a) They inhibit convective motions which inhibit the flow of heat energy to the solar surface. This causes a reduction in temperature and therefore also a reduction in opacity b) Magnetic pressure displaces some of the gas and decrease the local density. The combined effect of reduced opacity and density causes a depression in the optical surface, known as the Wilson depression. This exposes the inner hot walls of the flux tube and if the circumference of the flux tube is small enough, for geometrical reasons, the radiation from the hot walls dominates over the radiation coming from the dark floor of the evacuated space above the optical surface and this makes the overall magnetic element brighter. For smaller flux tubes, even the floor is bright as it is heated by the radiation coming from the bright walls. The brightness depends on the strength of the magnetic field, which determines the Wilson depression and therefore how much of the inner hot wall we are seeing. Also it is crucial that the magnetic flux tube has a small area and this is why pores are dark and not bright. This effect, known as the hot-wall effect, is a well studied area in solar physics (Spruit 1976, Keller et al. 2004, Steiner 2005). I can condense the above discussion into two key points:

1) Individual magnetic elements can be bright or dark, depending on their size. Only small magnetic elements can be bright.

2) The degree of brightness depends on the Wilson depression, which in turn depends on the magnetic field strength.

Although there have been numerous efforts towards modelling stellar convection, stellar surface simulations that include both magnetic fields and radiative transfer have been sparse and only been done by two codes so far - MURaM (Beeck et al. 2011a, 2015a) and Co5BOLD (Steiner et al. 2014, Salhab et al. 2018a). The MURaM group simulated the spectral types - F3V, G2V, K0V, K5V, M0V and M2V, while the Co5BOLD group simulated the types - F5V, G2V, K2V and K8V. The findings from these two sets of papers can be summarized as follows:

1) The introduction of magnetic field changes the net outgoing radiative flux and therefore the $T_{\rm eff}$ of a star.

2) As we have discussed before, the amount of brightening crucially depends on the Wilson depression, which is a function of pressure scale height, density, and temperature dependence of opacity, and therefore also a function of spectral type. For the same magnetic field strength, the brightening increases from the K to the F models. See Figure 1.7 for a visual explanation.

3) The M star models show no bright points as their Wilson depression is extremely small. This leads to a net decrease in $T_{\rm eff}$.

As I have demonstrated in the last two sections, the temperature dependence of opacity, pressure scale height and density are the key factors that not only shape granulation but also the physics of magnetic flux tubes embedded in them. We should obviously look out for the significance of these factor later when we analyse our starspot simulations.

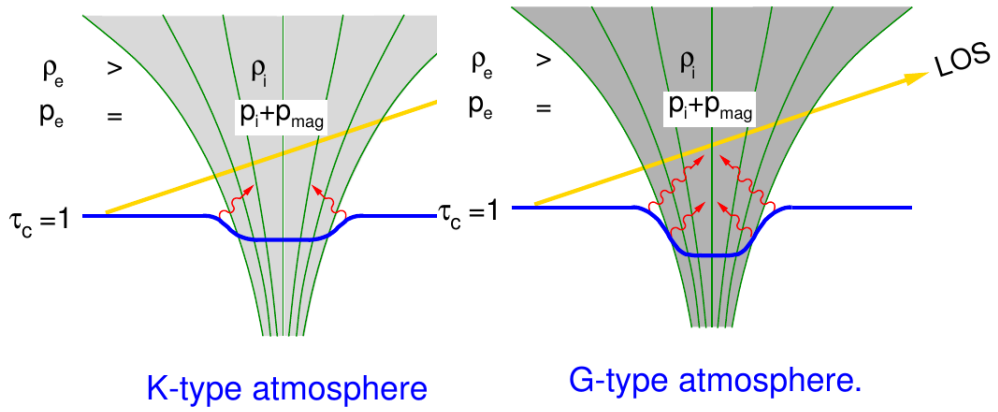


Figure 1.7: Cartoon showing magnetic flux sheets in two different stellar atmospheres. Note the difference in the depression of the optical surface and the resulting increase of the hot wall effect in the G star. Image Credit: Oskar Steiner

## 1.4 Sunspots

A discussion on starspots can not begin without a description of spots on the Sun, which is what I will do in this section. While discussing sunspots in the context of stellar spots, it is important to bear in mind that starspots have not been directly imaged and even a rudimentary understanding of their basic structure does not exist (again, see Berdyugina (2005)). Therefore I will confine my discussion to the basic properties of sunspots.

A sunspot is a cool ($\approx$ 4500 K in the umbra compared to the photospheric temperature of 5800 K), therefore dark ($\approx$ 20% of the quiet sun intensity, in the umbra) structure on the solar surface, composed primarily of two morphologically distinct regions- a dark central region called the umbra, and a brighter ($\approx$ 75% of the quiet sun intensity) filamentary structure surrounding the umbra, called the penumbra. The umbra is dark because it is a region of strong magnetic fields which quench convective motions that would have otherwise transported heat energy to the solar surface. The penumbral region has magnetic fields that are highly inclined and harbours a flow, known as the Evershed flow, directed away from the umbra. In this section, I will provide an overview of the existing body of knowledge on the fundamental properties (morphology, temperature, magnetic field and flows) of the umbra and the penumbra.

### 1.4.1 The Umbra

The umbra forms the central dark core of a spot. It has typically a brightness of around 20-30% (Solanki 2003) of the quiet Sun and magnetic field strengths in the range 1.5 to 3.7 kG (Livingston 2002). It was suggested very early on (von Klüber 1948), and later confirmed by other studies (Martinez Pillet and Vazquez 1993, Kopp and Rabin 1992), that a local relationship exists between the darkness at a given point inside the

umbra and the magnetic field strength at that point. Stronger magnetic fields are better at inhibiting convection therefore results in lower temperatures. The umbral brightness and its magnetic field strength are also related to the size of the sunspot. Larger spots have darker umbrae (Mathew et al. 2007, Schad 2014a) and they also harbour the strongest magnetic fields (Livingston 2002, Schad and Penn 2010, Kiess et al. 2014). If, and how, the temperature and magnetic field strength of umbrae depend on the phase of the solar cycle has been the subject of much debate. Albregtsen and Maltby (1978) reported that sunspots are the darkest, early on in the solar cycle and sunspots emerging later become increasingly bright. However, Norton and Gilman (2004) found contradicting results of sunspot brightness decreasing with the advent of the solar cycle, and then increasing again in the latter half. Mathew et al. (2007) conducted a study on 160 spots and arrived at the conclusion that umbral brightness is not significantly correlated with the phase of the solar cycle. Several studies since then (Watson et al. 2011, Rezaei et al. 2015, Penn and Livingston 2006) have reported a decrease in umbral field strength and often an associated increase in brightness as the cycle progresses. Schad (2014a), the study covering the largest number of sunspots (7530) found no evidence of a long term decrease in magnetic field strength. As of now, the debate stands unresolved. Fortunately, even if the umbral temperature and field strength were to have a solar cycle dependence, the reported yearly rates of change are weak enough that, for the purpose of this thesis we can ignore any such variations.

The umbra is not a homogeneous structure; in fact it is populated by bright umbral dots (see Watanabe (2014) for a review). MHD simulations have suggested that these bright dots are sites of very localized magnetoconvection and their brightness is caused by upflows bringing up hot material from greater depths (Schüssler and Vögler 2006). These simulations further predicted that umbral dots should have a a dark core that would form higher up in the atmosphere where the upflow loses its inertia and turns over. Significant headway was made when observations confirmed the presence of upflows in umbra dots (Bharti et al. 2007, Riethmüller et al. 2008). These upflows were surrounded by localized downflows (Riethmüller et al. 2013) lending support to the theory proposed by Schüssler and Vögler (2006). Although Bharti et al. (2007) and Rimmele (2008) found the dark cores predicted by MHD simulations, the umbral dots they analysed were located close to the periphery of the umbra and could have been remnants of light bridges. The studies of centrally located umbral dots by Riethmüller et al. (2013) and Louis et al. (2012a) did not find any substructures.

From an energy balance point of view the convective nature of the umbra is not at all surprising. Given that the umbra carries about 20 % of the heat flux of the quiet sun, a mean flow of the order of a few 100 m/s can be expected. Tiwari et al. (2015), did find a height dependent downflow of a few 100 m/s in the umbra in their 3D inversion, despite using the line core at $\tau = 1$ of the umbra as their reference wavelength for calculating the Doppler shifts. Recently, Löhner-Böttcher et al. (2018a) attempted to study the absolute velocities in the umbra using the Ti I 571.4 nm line, which forms in the deep photosphere, and found a height dependent flow as well. Deep in the umbral photosphere they measured an upflow of few 10s of m/s while higher up they measured downflows. Whether the umbra harbours a mean flow is a question that is yet to be resolved.

#### 1.4.1.1 The Wilson Depression

The presence of strong magnetic fields in the umbra reduces the temperature and gas pressure. This leads to a drop in opacity and density and allows us to see deeper into the photosphere. This depression of the optical surface is termed as the Wilson Depression. Measuring the Wilson depression is a difficult task and initial estimates, using methods based on geometry produced a wide range of values - 400 to 2000km (Solanki 2003). Recently, using a new technique which minimizes the divergence of the 3D magnetic field vector, Löptien et al. (2020) puts the value of the Wilson depression between 400 and 700km. They also found out, unsurprisingly, that strong magnetic fields cause larger Wilson depressions.

### 1.4.2 The Penumbra

The penumbra is a display of magnetoconvective processes in all their glory. It is composed of numerous bright filaments (sometimes also called *intraspines*) which are separated by narrow dark lanes (also called *spines*) (Moore 1981). The terms *spine* and *intraspine* were first introduced by Lites et al. (1993), who also found that the *spines* are regions of stronger and more vertical magnetic fields, while the *intraspines* have fields that are horizontal and weaker. The bright filaments have thin dark cores (not to be confused with the much broader dark *spines* that separate the bright filaments) running along their centres. The dark cores, which are about 100 km wide, are visible only at high resolution and were first reported by Scharmer et al. (2002), and subsequently further studied by Bellot-Rubio et al. (2007) and Langhans et al. (2007a). The tip of the filament that is on the umbral side, also known as penumbral grain, is usually brighter than the rest of the filament and often migrate inwards into the umbra (Muller 1976, Sobotka et al. 1999).The first complete picture of a penumbral filament, with detailed descriptions of their flows and magnetic field structures, was provided by Tiwari et al. (2013), using spatially coupled 2D inversions (also see van Noort et al. (2013)). They also found that penumbral filaments are nearly identical to each other and do not show much variation of their properties.

#### 1.4.2.1 The Evershed flow

The penumbra is much more dynamic and lacks the reticent, sage-like demeanour of the umbra. Its convective nature was discovered by Evershed (1909), who found that spectral lines coming from the disk-side penumbra show a blueshift, while those coming from the limb-side penumbra show a redshift. For sunspots located at the disk centre, spectral lines originating from the penumbra did not show strong Doppler shifts. He concluded that the penumbra harbours a flow that is directed radially outwards from the umbra.

The Evershed flow is intricately connected to, and driven by the magnetic field geometry of the penumbra. Recent high resolution observations with the aid of realistic MHD simulations have helped form a coherent picture of how the Evershed flow interacts with the inclined magnetic field of the penumbra and shapes its structure and appearance. Here I will attempt to explain the physics of the penumbra by following the journey of the Evershed flow.

The Evershed flow rears its head from underneath the photosphere as a vertical upflow at the umbral edge of a penumbral filament. As it is carrying hot, dense material, it lends a bright tear-drop shaped glow to the tip of the filament. Its inertia helps it move further up the atmosphere, pushing up the optical surface in the process. As it moves up it cools down and begins to tread the inclined path laid out by the horizontal fields of the penumbra. As a consequence of the optical surface being pushed up, the Evershed flow, now rapidly losing its heat by radiation, leaves behind a cool dark lane (the thin dark core of the bright filaments) in its wake. The flow, as it moves along the dark core of the bright filament, keeps losing mass from either side. Finally, as it reaches the end of the filament and the outer edge of the penumbra it has become dense enough to sink back into the Sun. As it dives back into the Sun, it pulls down the magnetic field lines with it, creating fields of the opposite polarity. Clearly, this process is very similar to overturning convection in granules, except the flows are asymmetric and are guided by strong horizontal fields. (Westendorp Plaza et al. 1997, Scharmer et al. 2002, Heinemann et al. 2007, Langhans et al. 2007b, Zakharov et al. 2008, Rempel et al. 2009b,a, Rempel 2011a, Borrero and Ichimoto 2011, Franz et al. 2016, Borrero et al. 2017, Siu-Tapia et al. 2018).

Although much of the physics of the penumbra has been laid bare, what leads to its formation is still shrouded in mystery. The general consensus is that the presence of horizontal fields leads to penumbra formation. This can be either as a result of a) horizontal fields emerging from below the photosphere (Leka and Skumanich 1998, Guglielmino et al. 2014) or b) field lines from above being pushed down (Murabito et al. 2016). Observations that show the appearance of the penumbra in the chromosphere (Romano et al. 2013, Shimizu et al. 2012) before it appears on the surface have bolstered the second theory. So far, in MHD simulations (Rempel 2011a) respectable penumbral proportions are achieved by artificially modifying the upper boundary condition; the horizontal component of potential configuration is multiplied by a factor of 2. Clearly, this is an area of research that is still ripe for picking.

#### 1.4.2.2 Light Bridges

Rogue penumbral filaments often intrude into the umbra (Louis et al. 2012, Benko et al. 2018a) and divide a sunspot into two or more parts. Such penumbral intrusions are called lightbridges. Lightbridges are not necessarily penumbral intrusions; they can simply be granulation invading a spot (for example, Lagg et al. (2014)), or form during spot formation when the emerged flux is coalescing together (Cheung et al. 2010, Toriumi et al. 2015). Lightbridges have recently come to the fore for nesting very strong transient magnetic fields. When they form between two umbrae of opposite polarities, the colliding Evershed flows create turbulent conditions that facilitate the formation of very strong magnetic fields (Okamoto and Sakurai 2018, Hotta and Toriumi 2020, Castellanos Durán et al. 2020).

To summarize, sunspots offer us the unique opportunity to study magnetoconvective processes at play. Clearly, radiative-MHD simulations have helped unearth much of the physics described above and additionally have produced intensity images that are often indistinguishable from actual observations of sunspots (see Figure 1.8).

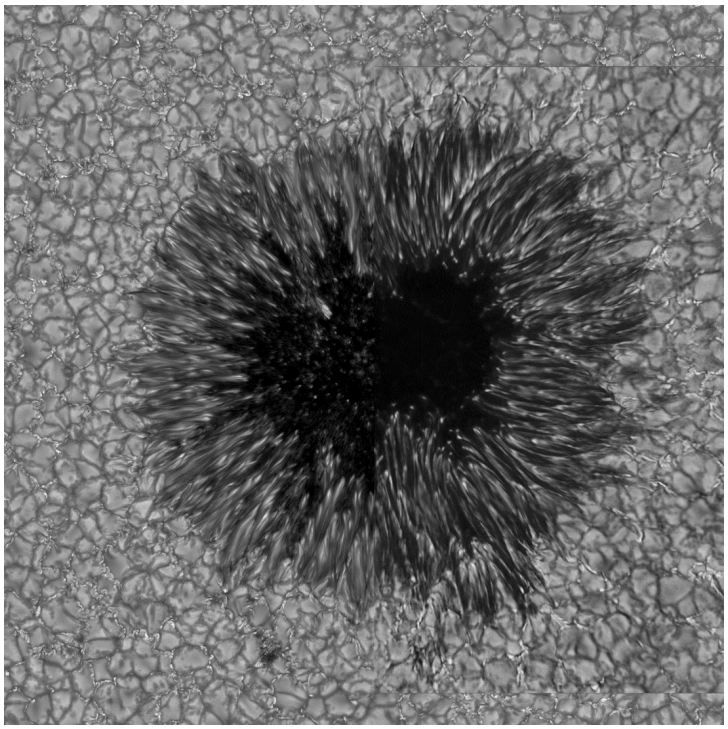

Figure 1.8: The left half of the image is a simulated sunspot, created (by Matthias Rempel) using the rad-MHD code MURaM, while the right half is an actual observed sunspot (F. Wöger, National Solar Observatory). The composite image was created by Matthias Rempel.

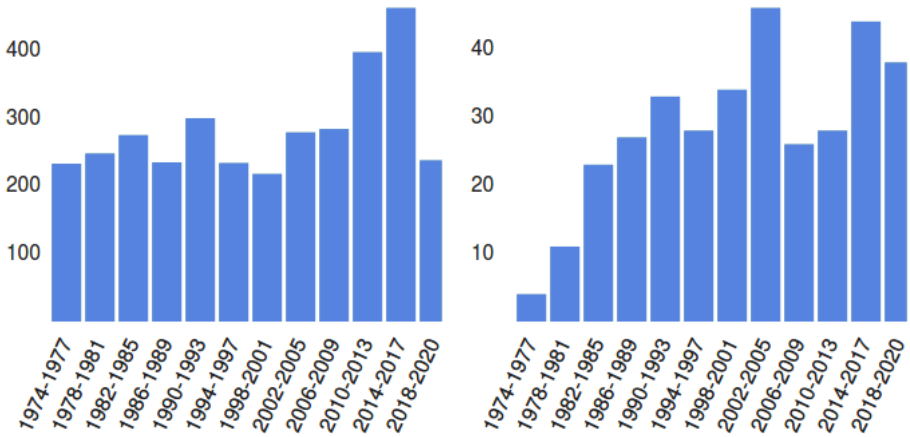


Figure 1.9: Left: Number of refereed papers published with sunspot(s) in their title. Right: Number of refereed papers published with starspot(s) in their title.

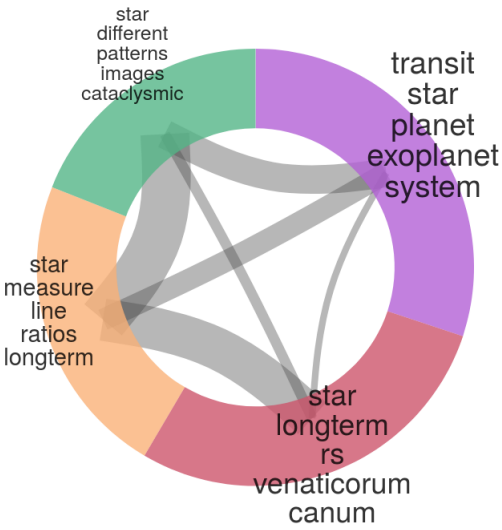


Figure 1.10: The "starspot(s)" paper network generated using ADS (ui.adsabs.harvard.edu). All 342 papers published on starspots divided into groups based on the references they share. The size of a wedge of a given colour is proportional to the number of papers published in that group. The thickness of the gray bands indicate the number of references two different groups have in common.

## 1.5 Starspots

The field of starspots is still in its nascency. Figure 1.9 shows a comparison between the number of papers published with the word sunspot (or sunspots) in the title, and the number of papers published with the word starspot (or starspots) in the years 1974-2020. The number of papers published on starspots are still roughly an order of magnitude less than the papers published on sunspots. A primary reason for this is that spots on other stars are very hard to resolve and individual starspots have not been directly observed. There is little to no knowledge about their morphology or fine structure. However, different inversion techniques have been used to retrieve large scale surface inhomogeneities of other stars, which allows us to study the average properties of what could be either very large starspots or clusters of spots.

Figure 1.10 divides papers published on starspots into groups based on the references they share. The names of the groups are created by searching for unique, shared words in the group's paper titles. The group names are indicators of the broad subtopics that papers on "starspots" fall in (for details see `https://ui.adsabs.harvard.edu/help/actions/visualize#paper-network`). As you can see, a significant chunk of the research done on starspots is in the context of exoplanets. The other major areas of research on starspots are directed towards measuring individual starspot properties (keywords - "measure", "line ratios"), their distribution on stellar disks ("patterns", "images"), and RS Canum Venaticorum (RS CVn) stars. The word "longterm" appears in two different groups. In this section, I will first list the different types of techniques used to detect and/or characterize starspots and then discuss the collective knowledge we have gained from these diverse techniques, using Fig: 1.10 as a rough guide.

### 1.5.1 Starspot Observation Methods

1. **Lightcurves** - The modulations seen in the lightcurve of a star can be attributed to inhomogeneities on the stellar surface. Using a trial and error method, it is possible to model the distribution and darkness of spots that would cause the observed photometric variations (Budding 1977, Vogt 1981b). However, one major disadvantage of this method is that the solutions are generally rather simple (typically 2 or 3 spot models) and are often not unique.

2. **(Zeeman) Doppler Imaging** - In fast rotating stars, each wavelength point in a rotationally broadened spectral line profile corresponds to a specific longitude on the star's disk. Inversion techniques based on this principle, when applied to stellar Stokes I profiles, can be used to retrieve temperature maps of a stellar surface (Vogt and Penrod 1983, Goncharskii et al. 1977a). Unlike lightcurve inversions, this technique can also constrain starspot latitudes - polar spots will only affect the line core, whereas equatorial spots will affect the entire line profile. However, Doppler imaging requires high resolution spectral data and can only map the surfaces of fast rotating stars. The same principle, when applied to Stokes V profiles, can be used to infer magnetic field inhomogeneities on a stellar surface (Semel 1989a, Donati et al. 1989, Brown et al. 1991). A criticism of the Doppler Imaging technique is that may produce polar spots as artefacts. Chromospheric activity and antisolar differential rotation can both flatten photospheric line cores and therefore mimic the signature of polar spots (Johns-Krull 1996, Bruls et al. 1998).

3. **Interferometry** - A recent advancement in mapping of stellar surfaces was the imaging of a spotted star achieved using optical interferometry (Roettenbacher et al. 2016). A major advantage of this method is that the resolution is set by the distance between the telescopes and not by the telescope diameter. Furthermore, interferometry can unambiguously detect polar spots, the detection of which is not reliable by Doppler Imaging.

4. **Line-depth ratios (LDR)** - This technique compares the depths of temperature sensitive lines against those that are insensitive to temperature variations and can detect temperature differences as small as 10K on a stellar surface (Gray 1996, Catalano et al. 2002a). This does not provide any information about starspot location and is typically very useful when used in conjunction with a mapping technique.

5. **Molecular Bands Modeling** - The surfaces of G and hotter stars are too hot for most molecules to form. Therefore any presence of molecules on these stars must come from cooler features. Since there is little knowledge about stellar atmospheres, the modeling of the molecular bands is done by combining spectra of different standard stars (Huenemoerder and Ramsey 1987a, Neff et al. 1995a, O'Neal et al. 1996a). For example, the spectra of a spotted G star can be modeled as a superposition of the spectra of an inactive G star (representing the quiet star) and an inactive M star (representing the spots). This method, like LDR, cannot be used to produce a stellar surface map; it returns spot temperature and filling factor.

6. **Planetary Transits** - When a planet traverses a stellar disk, it might occult spots

on the star. Such an occultation would cause an "emission bump" in the U-shaped (caused by the transiting planet) dip of the lightcurve. This allows us to achieve a very high resolution, since at any given point in time we are sampling only the area of the stellar disk hidden by the transiting exoplanet (Mancini et al. 2013, Morris et al. 2017). However the effectiveness of this method depends on chance - the area of the stellar disk covered depends on (1) the angle between our line of sight and the orbital plane of the transiting planet and (2) the inclination of the orbital plane of the planet to the rotation axis of the star.

### 1.5.2 Spot characteristics: Temperature and Magnetic Field

Berdyugina (2005) compiled a list of starspot temperatures measured till then, and plotted the spot temperature contrasts ($T_{phot}$ - $T_{spot}$) versus the corresponding stellar photospheric temperatures. She found that the higher the photospheric temperature is, the higher is the temperature difference between the spot and its surrounding photosphere. The physical reasons for this trend are still not clear and we will attempt to understand the physics behind this trend in this thesis. Berdyugina (2005) had speculated that cooler stars might have larger penumbrae and therefore lower spot temperature contrasts.

Mancini et al. (2013) updated the plot of Berdyugina (2005) and included spot temperature contrasts measured using planetary transits. It seems that planetary transits and lightcurve inversions often produce spot temperatures that are higher than those obtained by modeling molecular bands. It is quite possible that molecules form only in the umbra of spots and therefore fitting their spectra produce higher spot contrasts.

The magnetic field strength of an individual starspot is yet to be measured. Zeeman Doppler Imaging is the most common technique that is used to map the large scale distribution of magnetic fields on stellar surfaces. For reviews of magnetic fields measured on stars other than the Sun see Strassmeier (2009) and Donati and Landstreet (2009). One inherent flaw of the ZDI technique is that it is better at measuring magnetic fields in the brighter regions of a star. For example, see the surface temperature and magnetic field maps of II Pegasi (Carroll et al. 2007) where the colder regions hardly show any magnetic field. This makes ZDI somewhat unsuitable for measuring starspot magnetic fields. Recently Afram and Berdyugina (2015) computed synthetic Stokes profiles of molecular lines to gauge their potential to measure starspot field strengths on F,G, K and M stars. Subsequently Afram and Berdyugina (2019), using molecular and atomic lines simultaneously, measured the magnetic field strengths in starspots on 9 M-dwarfs and found them to lie in the range 3-6 kiloGauss.

Although the measurement of magnetic field strengths of individual starspots have not been possible yet, a significant body of work exists on average magnetic fields on stellar surfaces. While on the Sun the average unsigned field strength is only a few 10s of Gauss, average field strengths in the kiloGauss range have been measured on M stars (Reiners et al. 2009, Shulyak et al. 2019). It is not quite clear whether these high average field strengths are more indicative of the field strengths of facular regions or of starspots.

### 1.5.3 RS Canum Venaticorum (RS CVn) stars

For an uninitiated reader, it might seem odd that such a significant chunk of research on starspots is directed towards RS CVn stars. These are typically close binary systems and consisting of a subgiant that has evolved off the main sequence and a main sequence star. The gravitaitonal interaction between the two stars makes them very fast rotators. In particular the subgiant component, due to its larger radius, shows very large surface rotation velocities. Their fast rotation makes them prime targets to be studied using techniques that rely on the Doppler effect. RS CVn binaries are also highly variable and their lightcurves typically show a lot of modulation, which makes them suitable candidates for lightcurve inversions. An added advantage is that the star's companion can often occult starspots producing an "emission" bump in the lightcurve. A significant chunk of our knowledge about starspots has come from observing RS Cvn stars (see reviews by Hussain (2002), Berdyugina (2005), Strassmeier (2009)).

### 1.5.4 Spot Distribution and Lifetimes

Sunspot studies spanning several centuries have revealed some fundamental properties about the distribution and lifetimes of spots on the sun:

1. Sunspots do not appear near the poles of the Sun. They appear in a latitude belt within 30 degrees of the equator (Solanki 2003).

2. If they have a longitudinal preference is unclear with studies contradicting each other. While Berdyugina and Usoskin (2003) claim the Sun has active longitudes 180 degrees apart, Pelt et al. (2006) argue that this result is a mere artifact of their analysis technique. However there is plenty of evidence for nesting of spots, that is, sunspot groups appearing in locations where sunspots existed previously (see Işık et al. (2020) and references therein).

3. Individual sunspots are very small compared to the solar disk and collectively they can cover up to 1 % of the visible hemisphere during cycle maxima.

4. Sunspots typically last for a few days to a few weeks. Their lifetime has been shown to be correlated with their size. Larger spots live longer (Petrovay and van Driel-Gesztelyi 1997).

It was found early on that none of these properties are necessarily true for spots on other stars. Starspots, to begin with, do not seem to have constraints on their latitude of occurrence. Polar spots and spots in high latitudes are commonly observed for giants and subgiants that rotate rapidly (Strassmeier et al. 1991, Donati et al. 1992, Hatzes and Vogt 1992). In some young T Tauri stars, spots have been observed at both high and low latitudes simultaneously (Strassmeier et al. 1994, Collier Cameron and Unruh 1994). Further, some cool stars are definitely known to have active longitudes (Olah et al. 1991, Järvinen et al. 2005, Lanza et al. 2009, García-Alvarez et al. 2011). While sunspots cover a tiny fraction of the solar disk, spots on other stars are frequently known to cover a significant fraction of the stellar surface, sometimes even up to 80 % (see figure 10 of Berdyugina

(2005)). Such a high coverage of the stellar surface by magnetic fields (if indeed correct) would seem to imply islands of relatively field-free gas surrounded by a magnetic ocean.

The lifetimes of starspots are important for a few reasons - (1) they can provide insight about the dynamo processes that generate them, (2) spot lifetimes should be reflective of the diffusive timescales and therefore convective velocities on stellar surfaces, and (3) better constraints of starspot lifetimes will assist in disentangling starspot signatures from exoplanet signatures. Spot lifetimes are usually studied using lightcurves and sometimes Doppler Imaging. I will list below some of the major findings about starspot lifetimes. For an early review on spot lifetimes see Hussain (2002); for a more recent review see Section 13 of Strassmeier (2009).

1. Starspots, both on single giants and fast rotating RS CVn binaries, can last for several years. It is quite possible that spots disintegrate and emerge at the same "active longitude", giving the impression that a single active region persists over a long time. On some RS CVn binaries, active longitudes have lasted for decades (see Hussain (2002) and references therein). Doppler Imaging has also revealed polar spots that have been known to last for several years (for example, Vogt et al. (1999)). Basri and Shah (2020) caution us to be careful about "active longitudes" retrieved from lightcurves alone, as they may be mere artifacts of the inversion process.

2. There has been a renewed interest in starspot lifetimes as they are also of importance to planet hunters. Recently Giles et al. (2017) found that starspot lifetimes depend on the stellar effective temperature; spots last longer on cooler stars. Namekata et al. (2019) studied individual spots on 5356 solar-like stars using lightcurves and puts spot lifetimes on these stars between 10 and 350 days. Basri and Shah (2020) argue that the lifetimes derived by Namekata et al. (2019) should be reinterpreted as the evolution of a dip in a lightcurve only tells us how long an asymmetry in spot distribution lasts.

### 1.5.5 Spots and exoplanets

A widely used method of detecting exoplanets is to look at the radial velocity variations of a star (Mayor and Queloz 1995). A planet revolving around a star will make the star wobble about its axis. When the wobble is along our line-of-sight, it will introduce Doppler shifts in the emergent spectra of the star. However, for this method to be effective, one must rule out that variations in radial velocity (RV) are not due to the dynamics on the stellar surface itself. Starspots, unfortunately, often produce RV signals that are indistinguishable from exoplanet signals and has led to false detections of planets (for example, see Robertson et al. (2014)). There are several ways starspots can induce changes in the RV of a star:

1. Spectral lines emerging from fast rotating stars undergo significant rotational broadening. The presence of starspots in one hemisphere will cause of loss of photon flux and will break the symmetry between red and blue shift. The first attempt to quantify this was by Saar and Donahue (1997) who assumed the spot to be at 0 K. Hatzes (2002a) improved on this and assumed a spot temperature difference of 1200 K with the photosphere. Desort et al. (2007) showed that RV shifts depend on the spectral line being used and computed RV using the full HARPS spectrum.

2. Soon it was realized that starspots inhibit convection locally and their spectrum is redshifted compared to the local convective blueshift and this further affects the RV. This effect has been modelled several times (Lagrange et al. 2010, Lanza et al. 2010, Dumusque et al. 2014a).

3. Starspots, if they are anything like sunspots, should harbour flows of their own. The penumbra harbours upflows, downflows and flows perpendicular to the line-of-sight (at disc centre). This should further affect the convective blueshift. Since we do not have simulations or observations of individual spots on other stars, this affect has not been studied yet.

As one can see, our knowledge on starspots is very limited compared to what we know about sunspots. Although we have made some progress about the properties of large -scale stellar surface structures, we know very little about individual spots on other stars. In this thesis, we aim to fill in this gap and study starspot fine structure using radiative-MHD simulations.

## 1.6 The MURaM code

In this section, I will briefly describe the MURaM code used for the radiation magnetohydrodynamic simulations presented in this thesis. Magnetohydrodynamics (MHD) describes the motion of an electrically conducting fluid as affected by the presence of magnetic fields, and the strength and behaviour of these magnetic fields as affected by the motions of the said fluid. The fluid is composed of charged particles, often of different kinds, and to be able to use the abstraction of MHD which describes their macroscopic behaviour one must first make a few assumptions. The relevant lengthscales must be much larger than the ion gyroradius and their mean free path. Our timescales of interest must be much longer than the mean free time between collisons and the ion gyroperiod.

One can construct the MHD equations by postulating a set of laws that conserve mass, momentum, energy and magnetic flux. The MURaM code solves the MHD equations in conservative form, which ensures that certain fluxes are always conserved. The spatiotempral evolution of a physical quantity that is conserved is described by -

$$\frac{\partial(quantity)}{\partial t} + \nabla \cdot (flux\ of\ quantity) = source - sink.$$

Here I will describe the MHD equations in conservative form, as solved by MURaM. $\rho$, $\mathbf{v}$, $e$, $p$, $\mathbf{B}$ are density, velocity, energy per unit volume, pressure, and magnetic field respectively. Note that the following equations will not have explicit diffusive or viscous terms; MURaM uses artificial diffusivities for the variables $\rho$, $\mathbf{v}$, $e$, and $\mathbf{B}$ (see Rempel et al. (2009b) for the implementation of the diffusivity scheme).

The equation of continuity which states that mass in conserved is given by,

$$\frac{\partial \rho}{\partial t} + \nabla \cdot (\rho \mathbf{v}) = 0. \tag{1.12}$$

The equation of motion can be written down by balancing the forces acting on a parcel of fluid of constant volume -

$$\rho \frac{\partial \mathbf{v}}{\partial t} + \rho(\mathbf{v} \cdot \nabla)\mathbf{v} = -\nabla p + \frac{1}{4\pi}(\nabla \times \mathbf{B}) \times \mathbf{B} + \rho \mathbf{g} \tag{1.13}$$

The LHS,

$$\rho\frac{\partial \mathbf{v}}{\partial t} + \rho(\mathbf{v}\cdot\nabla)\mathbf{v} \equiv \rho\frac{D\mathbf{v}}{Dt} \tag{1.14}$$

represents the acceleration of the fluid parcel caused by the forces acting on it. The terms on the RHS, starting from the left, stand for the gradient in pressure, the Lorentz force, and the gravitational pull. Multiplying equation 1.12 by $\mathbf{v}$ and combining with 1.14, the LHS of 1.13 can be rewritten as:

$$\rho\frac{\partial \mathbf{v}}{\partial t} + \rho(\mathbf{v}\cdot\nabla)\mathbf{v} = \frac{\partial(\rho\mathbf{v})}{\partial t} + (\rho\mathbf{v}.\nabla)\mathbf{v} + \mathbf{v}\nabla\cdot(\rho\mathbf{v}) = \frac{\partial(\rho\mathbf{v})}{\partial t} + \nabla\cdot(\rho\mathbf{v}\mathbf{v}), \tag{1.15}$$

where $\mathbf{vv}$ is the dyadic product. Clearly the quantity being conserved here is momentum. We can rewrite the equation of motion as:

$$\frac{\partial(\rho\mathbf{v})}{\partial t} + \nabla\cdot\left[\rho\mathbf{v}\mathbf{v} + \left(p + \frac{|\mathbf{B}^2|}{8\pi}\right)\underline{\mathbf{1}} - \frac{\mathbf{B}\mathbf{B}}{4\pi}\right] = \rho\mathbf{g}. \tag{1.16}$$

where $\mathbf{BB}$ is a dyadic product, $\underline{\mathbf{1}}$ is a $3\times 3$ unit matrix.

The energy equation conserves total energy per unit volume ($e$), where $e = e_{\text{internal}} + e_{\text{kinetic}} + e_{\text{magnetic}}$.

$$\frac{\partial e}{\partial t} + \nabla\cdot\left[\mathbf{v}\left(e + p + \frac{|\mathbf{B}^2|}{8\pi}\right) - \frac{\mathbf{B}(\mathbf{v}\cdot\mathbf{B})}{4\pi}\right] = \rho\mathbf{g}\cdot\mathbf{v} + Q_{\text{rad}}. \tag{1.17}$$

The energy per unit volume of the system can change when there is a source/sink of energy or work is done on/by the fluid. In the LHS of the equation, the $\nabla\cdot\mathbf{v}\left(p + \frac{|\mathbf{B}^2|}{8\pi}\right)$ term represents the work done by the pressure forces (fluid and magnetic), and $\nabla\cdot\left(\frac{\mathbf{B}(\mathbf{v}\cdot\mathbf{B})}{4\pi}\right)$ represents the work done by the Lorentz force. In the RHS, $\rho\mathbf{g}\cdot\mathbf{v}$ is the work done by gravity and $Q_{\text{rad}}$, which accounts for the radiative heating and cooling processes, is a source or sink term depending on its sign. Note that heat transport by conduction has been ignored as it does not play an attention worthy role in the photosphere.

The evolution of the magnetic field is given by the magnetic induction equation,

$$\frac{\partial \mathbf{B}}{\partial t} + \nabla\cdot(\mathbf{v}\mathbf{B} - \mathbf{B}\mathbf{v}) = 0, \tag{1.18}$$

where $\mathbf{vB}$ and $\mathbf{Bv}$ are dyadic products. In order to close this system of equations, equations of states relating $\rho$ and $e_{\text{int}}$ to $T$ (temperature) and $p$ (pressure) are used. For this, tabulated values, calculated using the OPAL equation of state are used (Rogers et al. 1996).

### 1.6.1 Calculating $Q_{\text{rad}}$

The MHD equations are coupled to the radiation scheme through the $Q_{\text{rad}}$ term in the energy equation. $Q_{\text{rad}}$ captures the contribution of radiative heating and cooling processes. We first calculate the time-independent radiative transfer equation for frequency $\mu$, which is given by,

$$\frac{dI_\mu}{d\tau_\mu} = S_\mu - I_\mu. \tag{1.19}$$

$S_\mu$ is the source function and $I_\mu$ is the specific intensity. $d\tau_\mu$ is the optical thickness of the path element, and is the product of the length of the path element (ds) and the absorption coefficient ($\kappa$). Under the assumption of local thermodynamic equilibrium (LTE), $S_\mu$ is equal to the Planck function. The radiative flux ($\mathbf{F}_\mu$) is then calculated by integrating the specific intensity over all ray directions. $Q_{\text{rad}}$ is now calculated as

$$Q_{\text{rad}} = \int_\mu (\nabla \cdot \mathbf{F}) d\mu \tag{1.20}$$

# 2 3D Radiative MHD simulations of starspots

The contents of this chapter were authored by Mayukh Panja, Robert Cameron, and Sami K. Solanki and published in the April 2020 edition of The Astrophysical Journal (Panja et al 2020 ApJ 893 113, DOI: https://doi.org/10.3847/1538-4357/ab8230).

## Abstract

There are no direct spatially resolved observations of spots on stars other than the Sun and starspot properties are inferred indirectly through lightcurves and spectropolarimetric data. We present the first self-consistent 3D radiative MHD computations of starspots on G2V, K0V and M0V stars, which will help to better understand observations of activity, variability and magnetic fields in late-type main-sequence stars. We used the MURaM code, which has been extensively used to compute "realistic" sunspots, for our simulations. We aim to study how fundamental starspot properties such as intensity contrast, temperature and magnetic field strength vary with spectral type. We first simulated in 2D, multiple spots of each spectral type to find out appropriate initial conditions for our 3D runs. We find that with increasing stellar effective temperature, there is an increase in the temperature difference between the umbra of the spot and its surrounding photosphere, from 350K on the M0V star to 1400K on the G2V star. This trend in our simulated starspots is consistent with observations. The magnetic field strengths of all the starspot umbrae are in the 3-4.5 kG range. The G2V and K0V umbrae have comparable magnetic field strengths around 3.5 kG, while the M0V umbra has a relatively higher field strength around 4 kG. We discuss the physical reasons behind both these trends. All of the three starspots develop penumbral filament-like structures with Evershed flows. The average Evershed flow speed drops from 1.32 km $s^{-1}$ in the G2V penumbra to 0.6 km $s^{-1}$ in the M0V penumbra.

## 2.1 Introduction

What do spots on stars other than the Sun look like? How dark are they and how strong are their magnetic fields? The lack of direct spatially resolved observations of other stars makes it difficult to answer such questions. Some properties of starspots can be inferred using lightcurves and spectropolarimetric data. The most prevalent methods used to infer information about starspot temperatures and filling factors are lightcurve inversions

(Vogt 1981a), molecular bands modelling (Huenemoerder and Ramsey 1987b, Neff et al. 1995b, O'Neal et al. 1996b, 2004), line depth ratios, (Gray 1996, Catalano et al. 2002b) and Doppler imaging (Goncharskii et al. 1977b, Vogt and Penrod 1983). Recently, planetary transit lightcurves have also been used to gain information about starspot properties (Mancini et al. 2013, Espinoza et al. 2018). All of these methods, with the exception of molecular lines, suffer from the drawback that they can only detect spots that are large enough to leave an imprint on disk integrated quantities. Even for sufficiently large spots, it is difficult to distinguish between temperature contributions from the umbra and the penumbra. Additionally, it is worthwhile to note that different techniques have been known to produce very different spot temperatures for the same star, a notable example being spots on the G1.5V sun-like star Ek Draconis. While Dorren and Guinan (1994) found a spot temperature of 5400 K using lightcurve modelling, Strassmeier and Rice (1998) and O'Neal et al. (2004) reported spot temperatures of 4800 K and 3800 K using Doppler Imaging and modelling molecular bands, respectively. A comprehensive discussion on the various methods of observations of starspots and their advantages and disadvantages can be found in the reviews by Berdyugina (2005) and Strassmeier (2009).

The measurement of magnetic field strengths on other stars is even more difficult as the lack of spatial resolution means the net circular polarisation tends to be cancelled out by oppositely directed magnetic fields. However, in rapidly rotating stars, if magnetic features of opposite polarities are sufficiently separated in longitude, the Doppler effect disentangles them in the Stokes V component of magnetically sensitive lines and this is exploited by the Zeeman Doppler Imaging technique to map magnetic fields on the stellar surface (Semel 1989b, Donati and Semel 1990). For slowly rotating stars if the line broadening due to the Zeeman effect is larger than the rotational broadening, and the surface coverage by such very strong fields is large enough, the magnetic field can be inferred from the amount of broadening (Gray 1984). For starspots, there is the added issue that, being dark, they provide little contribution to line profiles integrated over the stellar surface. This makes measuring their fields particularly challenging. However, molecular lines that form primarily inside starspots and have little contribution from quiet-star regions are being increasingly used to better constrain starspot magnetic field strengths (Afram, N. and Berdyugina, S. V. 2015, 2019). For a review of stellar magnetic field measurements, see Reiners (2012).

The review by Berdyugina (2005) compiled a list of starspot observations obtained by using various methods and, despite the many limitations placed on observations, she found a clear trend when she plotted starspot temperature contrast against stellar surface temperature. The cooler the star, the lower is the difference between the spot and quiet star temperature and the physical reasons for this are unclear.

All of the above-mentioned reasons point to the need for performing MHD simulations to better understand the physics of starspots and how it may differ from that of sunspots. Such simulations of thermal and magnetic structures of spots on other stars could also be useful to interpret observations and may even help in understanding the underlying stellar dynamo processes.

Although 3D radiative hydrodynamic simulations of near-surface layers for stars other than the Sun had been performed as early as 1990 by Nordlund and Dravins (1990a), the first stellar simulations including magnetic fields were performed by Beeck et al. (2011b) and Wedemeyer et al. (2013). Subsequently, Beeck et al. (2015a,b), studied the effects of

the magnetic field on surface properties such as intensity contrast and granulation structure in the spectral types F through M, using the MURaM code (Vögler et al. 2005). They further generated synthetic disk integrated spectral line profiles that can be compared with observations. Similar numerical studies using the CO$^5$BOLD code, investigating the effects of magnetic fields on surface processes in cool stars, have been carried out by Steiner et al. (2014) and Salhab et al. (2018b).

Spots on the Sun have been extensively simulated (Rempel et al. 2009a,b) using the MURaM code. These simulations have been fairly successful in reproducing the fundamental observed features of sunspots - a dark umbra dotted with bright umbral dots, surrounded by brighter penumbrae composed of filaments with thin dark cores, and the Evershed flow directed away from the umbral region towards the quiet Sun. Such simulations have been used to investigate the physical origins of many hitherto ill-understood observed properties of sunspots (Rempel 2011a,b, 2012, Rempel 2015, Siu-Tapia et al. 2018).

In this paper, we have used the MURaM code to perform the first-ever ab-initio simulations of spots on cool main-sequence stars other than the Sun, to investigate their fundamental properties, specifically - brightness relative to the stellar surface and magnetic field strength, as functions of stellar spectral type. As host stars we have considered a G2V, a K0V and an M0V star. Before carrying out 3D simulations, we first performed 2D computationally inexpensive simulations to navigate the parameter space with the intent of a) identifying suitable initial conditions for our final 3D runs and b) testing the sensitivity of our results to the variations in the initial conditions.

## 2.2 Simulations

We have used the MURaM (Max-Planck University of Chicago Radiative MHD) code (Vögler et al. 2005), which solves the MHD equations along with the radiative transfer equation and an equation of state that takes into account the effects of partial ionization. The version of the code used was the one employed by Beeck et al. (2013a,b, 2015a,b). Since we do not generate synthetic line profiles in this study, we used the grey approximation for the radiative energy transport.

Table 2.1 lists the dimensions and initial physical properties of the simulation boxes used for our 3D and 2D runs. We have simulated the spectral types - G2V, K0V, and M0V. The atmospheres of the M0V and K0V stars were obtained by starting from a solar atmosphere and changing the gravity (assumed constant throughout the computational domain) and entropy density of the plasma at the lower boundary until our desired effective temperatures were achieved. All the simulated stars are assumed to have solar metallicities.

### 2.2.1 3D Simulation Setup

We started our simulations with hydrodynamical runs of the three spectral types of stars. Once the hydrodynamical runs were sufficiently relaxed, we put in wedge-shaped magnetic flux tubes as initial conditions for the magnetic field. The horizontal extents of the inserted flux tubes at the optical surface were chosen such that they covered a similar num-

ber of granules in all of the different spectral types. Figure 2.1 shows the initial condition for the G2V starspot simulation.

The initial vertical field strength ($B_z$) of the flux tube is dependent only on geometrical height and is prescribed by:

$$\begin{aligned} B_z &= B_{bot} \exp \frac{-z}{\sigma}, & x \in [-w/2, w/2], \\ &= 0, & \text{otherwise.} \end{aligned} \tag{2.1}$$

Here $z$ is the height from the lower boundary, $x$ is the longer horizontal dimension, and $w$ is the width of the flux tube at every z, determined such that the vertical flux through every height is constant.

At $z = 0$ we set $B_z$ to $B_{bot}$ and at $z = h_{opt}$ (height of optical surface from lower boundary) , we set $B_z$ to $B_{opt}$, and this yields $\sigma$ to be

$$\sigma = h_{phot} / \log(\frac{B_{bot}}{B_{opt}}). \tag{2.2}$$

We choose $B_y$ (y being the shorter horizontal dimension) to be zero initially, everywhere. Thus the $\nabla \cdot B = 0$ constraint demands that $\frac{\partial B_x}{\partial x} + \frac{\partial B_z}{\partial z} = 0$ and we calculate $B_x$ as follows:

$$\frac{\partial B_z}{\partial z} = -\frac{B_{bot}}{\sigma} \exp \frac{-z}{\sigma} = -\frac{Bz}{\sigma}. \tag{2.3}$$

Therefore,

$$\frac{\partial B_x}{\partial x} = \frac{Bz}{\sigma}. \tag{2.4}$$

With $B_z$ being independent of x, and $\sigma$ being a constant, the integration is straightforward and

$$B_x = \frac{Bz}{\sigma} x, \tag{2.5}$$

with $B_x$ =0 at $x = 0$ (the centre of the flux tube).

Our choices of $B_{\rm bot}$ and $B_{\rm opt}$ have been tabulated in Table 2.2. Our 3D boxes extended to similar pressure scale depths and we chose similar values of $B_{\rm bot}$ for all the three stars - 15,14, and 15 kG for the G2V, K0V, and M0V stars respectively. We picked values of $B_{\rm opt}$ that one would naively guess from just the surface pressures – 3 and 3.2 kG for the G2V and K0V stars as they have comparable surface pressures. For the M0V star which has a surface pressure 5 times that of the G2V quiet star, a higher $B_{\rm opt}$ of 7 kG, which is roughly 3*sqrt(5), was chosen.

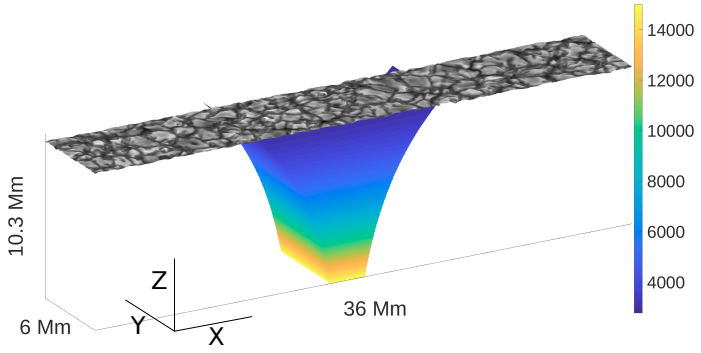


Figure 2.1: Initial magnetic structure for the G2V spot simulation. The depicted flux tube was introduced after the hydrodynamic run had achieved thermal equilibrium. The colours on the flux tube show $B_z$ in Gauss (see right colorbar). The gray surface shows the emergent bolometric intensity at the time the flux tube was inserted.

Table 2.1: Simulation Box Properties - 3D and 2D

| Spectral Type | | G2V | K0V | M0V |
|---|---|---|---|---|
| log g[a] | | 4.438 | 4.609 | 4.826 |
| $T_{eff}$ [K] | 3D | 5824.5 | 4809.5 | 3871.6 |
| | 2D | 5738.2 | 4894.3 | 3864.8 |
| Box Height [Mm] | 3D | 10.3 | 6 | 1.3 |
| | 2D | 7.3 | " | " |
| Photosphere [Mm] | 3D | 9.8 | 5.43 | 1.05 |
| | 2D | 6.4 | 5.44 | 1.04 |
| Box Length[b][Mm] | 3D | 36 | 27 | 10 |
| | 2D | " | " | " |
| # of $H_p$ [c](above,below) | 3D | 5, 11 | 8.2, 11.3 | 8.1, 8.2 |
| | 2D | 6.3, 9.3 | 4, 11.1 | 8.6, 8.0 |
| Resolution (hor,vert)[km] | 3D | 48, 17 | 36, 15 | 13.3, 4 |
| | 2D | 48, 21.5 | " | " |

[a] g is the surface gravity in $cm^2\ s^{-1}$
[b] All boxes have a length:width ratio of 6:1
[c] Number of pressure scale heights

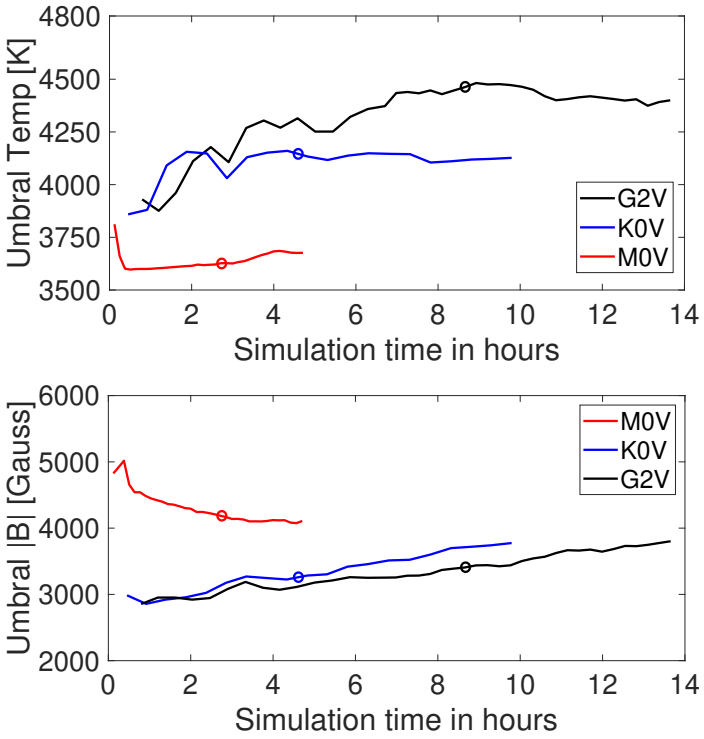


Figure 2.2: Evolution of average umbral temperatures (top) and average umbral magnetic field strengths (bottom) with time for the three simulated starspots. The circles mark the points in time when our snapshots were taken, which were after a similar number of granule lifetimes.

Table 2.2: Initial Magnetic Flux Tube Properties

| Spectral Type | | G2V | K0V | M0V |
|---|---|---|---|---|
| $B_{opt}$[kG] | 3D | 3 | 3.2 | 7 |
| | 2D (range) | 2.2 - 8.8 | 3.2 -12 | 3 - 12 |
| $B_{bot}$[kG] | 3D | 15 | 14 | 15 |
| | 2D (range) | 4 - 14 | 6 - 16 | 5 - 18 |

The magnetic field at the upper boundary was matched to a potential field configuration and the upper boundary was kept open to plasma flows. At the lower boundary, the flow velocity was artificially set to zero inside the flux tube, effectively "tying down" the flux tube to the lower boundary. This also mimics the physical effects of the flux tube extending below the lower boundary as heat flow by means of convection is prohibited.

#### 2.2.1.1 *Choosing a snapshot*

All of our simulated starspots are dynamical in nature, and they underwent several stages of evolution in the course of the simulation. After an initial highly dynamic phase, the

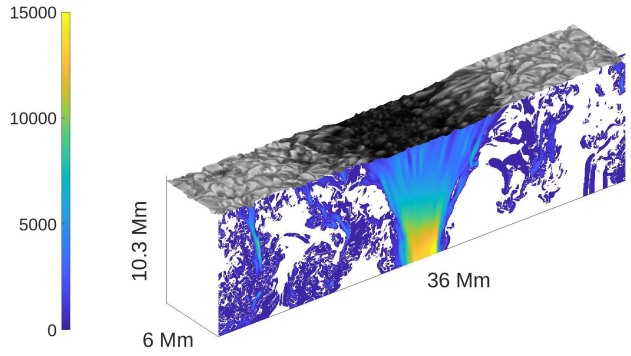


Figure 2.3: A 3D rendition of the simulated G2V star spot at the timestep of our analysis. The top grayscale surface shows the bolometric intensity and the vertical slice shows $B_z$. The corrugations of the top surface represent the variations in the geometric height of the optical surface ($\tau$ =1). The colorbar shows $B_z$ in Gauss.

magnetic flux tubes reach magnetostatic equilibrium with the surrounding fluid typically within the first hour of stellar run time. Subsequently, all of the three spots formed penumbral filament-like structures and the G2V and the K0V spots developed umbral dots. After a few additional hours, all of the flux tubes begin to get distorted underneath the surface by flute-like intrusions from the surrounding fluid. If allowed to develop for a sufficiently long time these intrusions manifest themselves at the optical surface as lightbridges. This process sets in at different times for the three spectral types, earliest for the M star and latest for the G star. Figure 2.2 shows the evolution of average umbral temperatures and average umbral magnetic field strengths of the three simulated spots with time.

We have chosen the time of our snapshots such that the umbral temperatures were well past their initial fluctuating phases and the spots had developed penumbral filament-like structures, but also sufficiently ahead of the umbrae of the spots getting too distorted by intruding lightbridges, for a meaningful analysis. A 3D rendition of the G2V starspot at the instance our snapshot was taken is depicted in Figure 2.3.

The G2V, K0V, and M0V snapshots were taken after 8.7, 4.6 and 2.7 hours of stellar runtime respectively. It is important to note that the timescales of granule evolution are different for different spectral types. A typical granule lifetime on the Sun is on average about 6 minutes whereas on the M0 star the granules last around 2.5 minutes. (Beeck et al. 2013b). Consequently, the snapshots were taken after a similar number of granule lifetimes - 80, 60 and 65 respectively for the G2V, K0V, and M0V stars.

### 2.2.2 2D Simulation Setup

The initial conditions used for the 2D simulations were the 2D analogs of the conditions used for the 3D runs, with the flux tubes being inserted in a 2D hydro-dynamical run. The computational ease afforded by having one less dimension allowed us to vary the two free parameters- $B_{\rm bot}$ and $B_{\rm opt}$, of the inserted flux tubes to simulate multiple spots for each spectral type. This allowed us to test the sensitivity of our results to changes in our chosen initial parameters. We simulated 24 spots in 2D, 8 for each spectral type. First, we kept $B_{\rm opt}$ constant (2.2, 3.2 and 3 kG for the G2V, K0V and M0V cases respectively) and

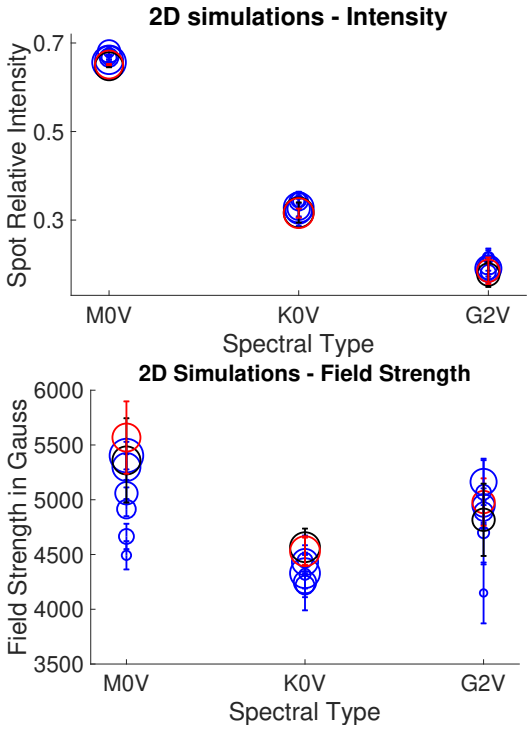


Figure 2.4: Upper Panel: Average umbral intensities, normalized by their quiet star intensities, of the 2D simulations, plotted against spectral type. Lower Panel: Average umbral field strengths at the optical surface. The size of the circles, in both the upper and lower panels, indicate the strength of $B_{\rm bot}$ while the color indicates the strength of $B_{\rm opt}$. Blue circles indicate runs with original $B_{\rm opt}$, while red and black correspond to runs where $B_{\rm opt}$ was increased by factors of 2 and 4 respectively. See Section 2.2 and the Appendix for more details.

explored a range of values of $B_{\rm bot}$. We started with $B_{\rm bot}$s of 4 (G2V), 6 (K0V) and 5 (M0V) kG and increased them roughly by a factor of 3, in steps of 2-3 kG. This constituted 6 of the 8 simulated spots for each spectral type. Then, keeping $B_{\rm bot}$ constant we increased $B_{\rm opt}$ by factors of 2 and 4. Table 2.2 lists our choices for $B_{\rm bot}$ and $B_{\rm opt}$. A detailed description of the 2D runs is given in the Appendix.

## 2.3 2D Results

Figure 2.4 summarizes the results obtained from our 2D simulations, where we have plotted the obtained umbral relative intensities($I_{\rm umbra}/I_{\rm quiet}$) and the average umbral magnetic field strengths at the stellar surface for the three different spectral types.

We see a steep decrease in umbral relative intensity (or increase in umbral contrast relative to the quiet star) with increasing $T_{\rm eff}$ in our 2D simulations. Interestingly, the relative intensities do not show much variation ($< 10\%$) within a spectral type when we change the initial magnetic field strengths of the flux tube. This is important as it demonstrates that the relative brightness of spots of a certain size is largely determined by the stellar surface properties and does not depend significantly on our choice of initial conditions.

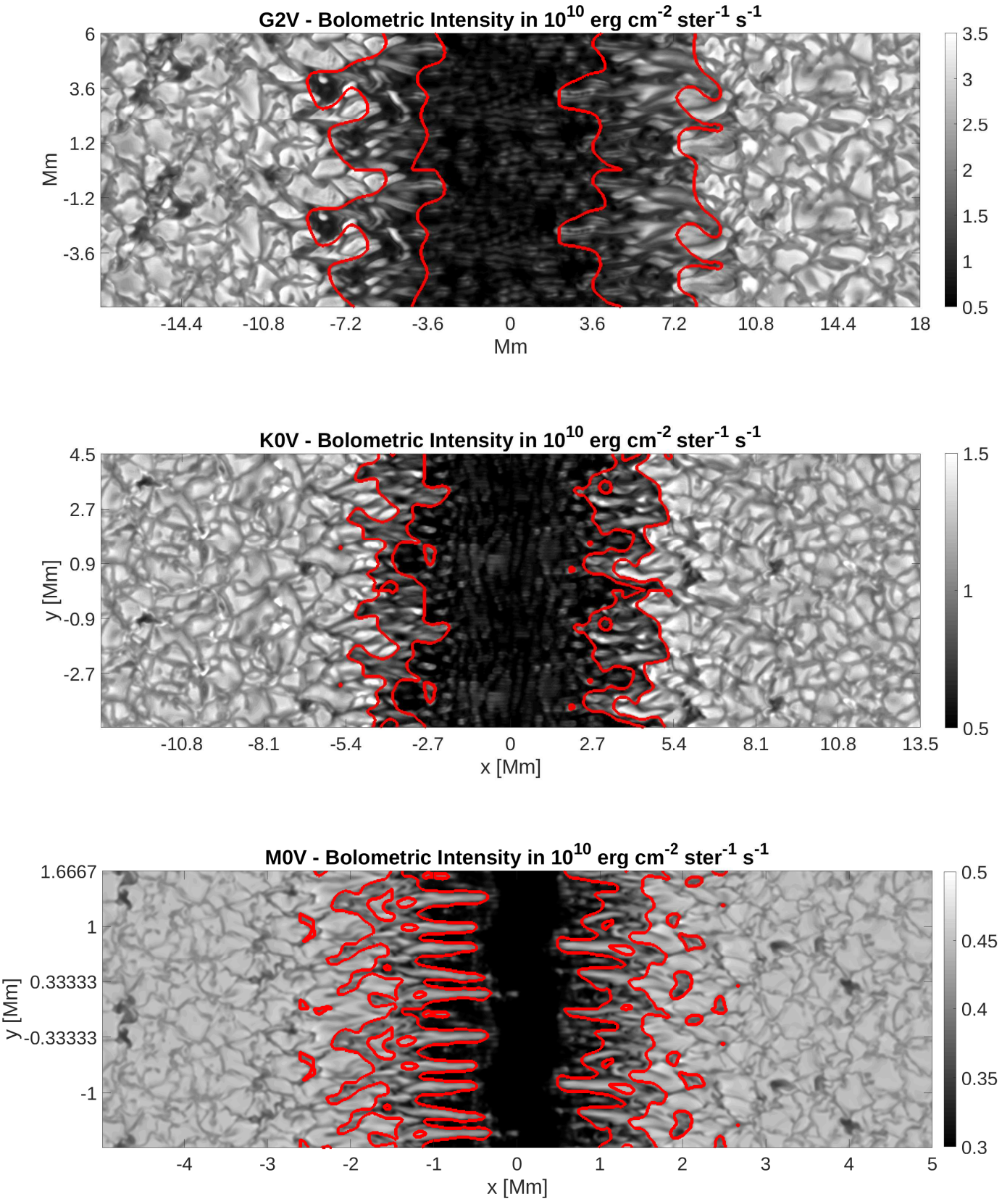


Figure 2.5: Bolometric intensity images of the simulated G2V, K0V and M0V starspots, repeated in the y-directon. The colorbar shows the intensity in units of $10^{10}$ erg cm$^{-2}$ ster$^{-1}$ s$^{-1}$. The red contours mark the boundaries of the penumbra.

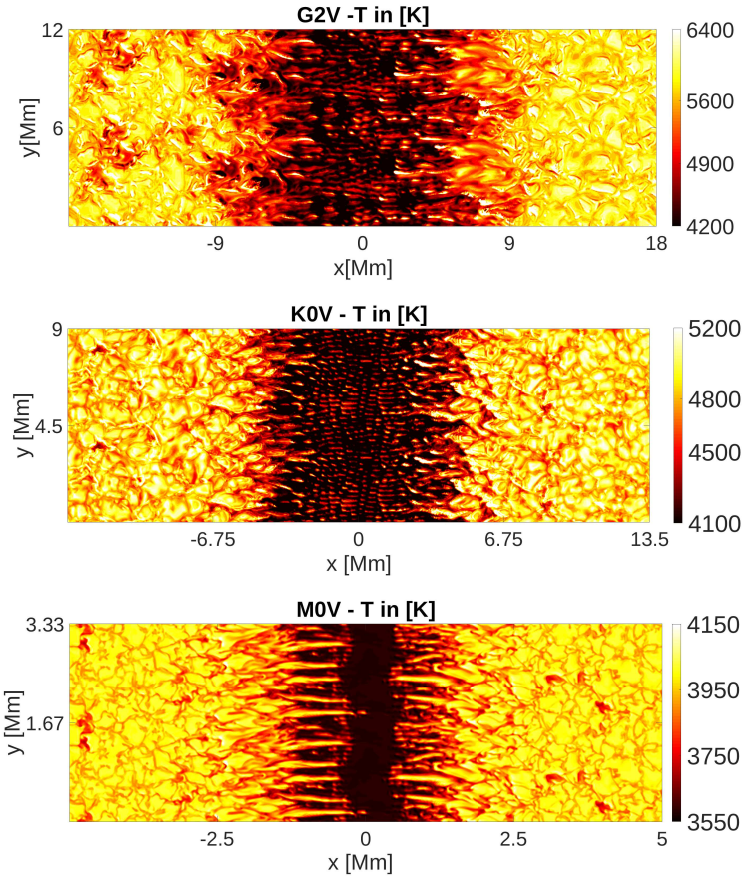


Figure 2.6: Temperature maps, in Kelvin (see colour bars at right of the individual panels), at the $\tau = 1$ surfaces of the three simulated stars - G2V, K0V and M0V.

This allows us to compare our results on spot brightness to observations with some degree of certainty.

All of the simulated spots have field strengths in the 4-6 kG range. The K0V spots, on average, have slightly lower umbral field strengths compared to the G2V and M0V spots, and the M0V spots reach the highest field strengths.The M0V umbral field strengths also have the maximum dependence on $B_{\rm bot}$ and therefore the widest distribution in field strength. Nevertheless, we find that the obtained umbral field strengths do not vary by more than 25% even when we change $B_{\rm bot}$ by a factor of 3 and $B_{\rm opt}$ by a factor of 4. Although the umbral field strengths obtained in our 2D simulations are higher than 3D simulations (Rempel et al. 2009b), their only weak dependence on initial conditions is reassuring. A detailed analysis of the 2D runs has been presented in the Appendix.

## 2.4 3D Results

### 2.4.1 Surface Properties

Figure 2.5 shows the bolometric intensity images of the three simulated spots. There are significant differences between the quiet star regions of the three spectral types, the most

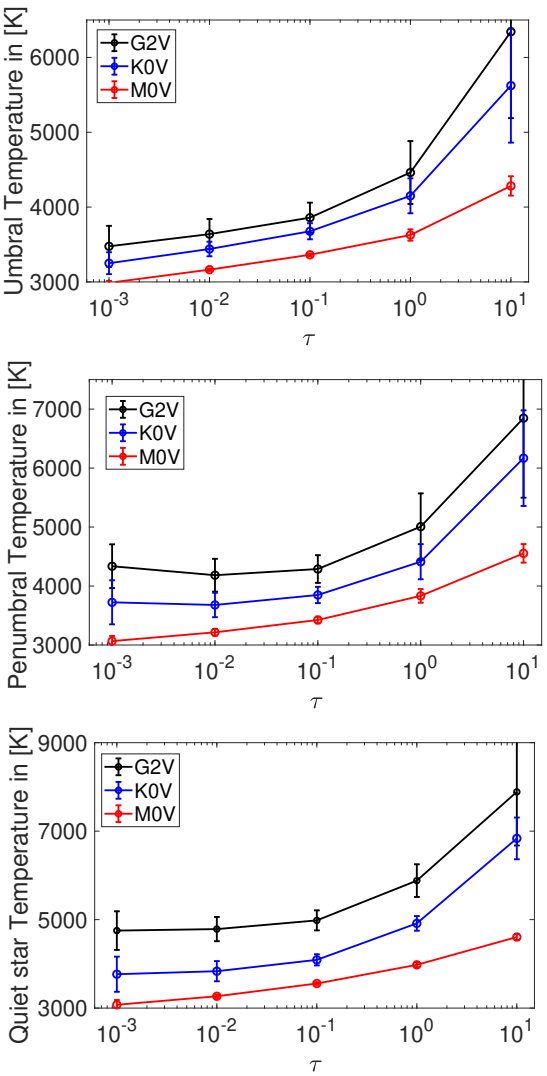


Figure 2.7: Top to bottom: Umbral, penumbral and quiet star temperatures, in Kelvin, averaged over different iso-$\tau$ surfaces. The error bars show the standard deviations of the computed averages.

.

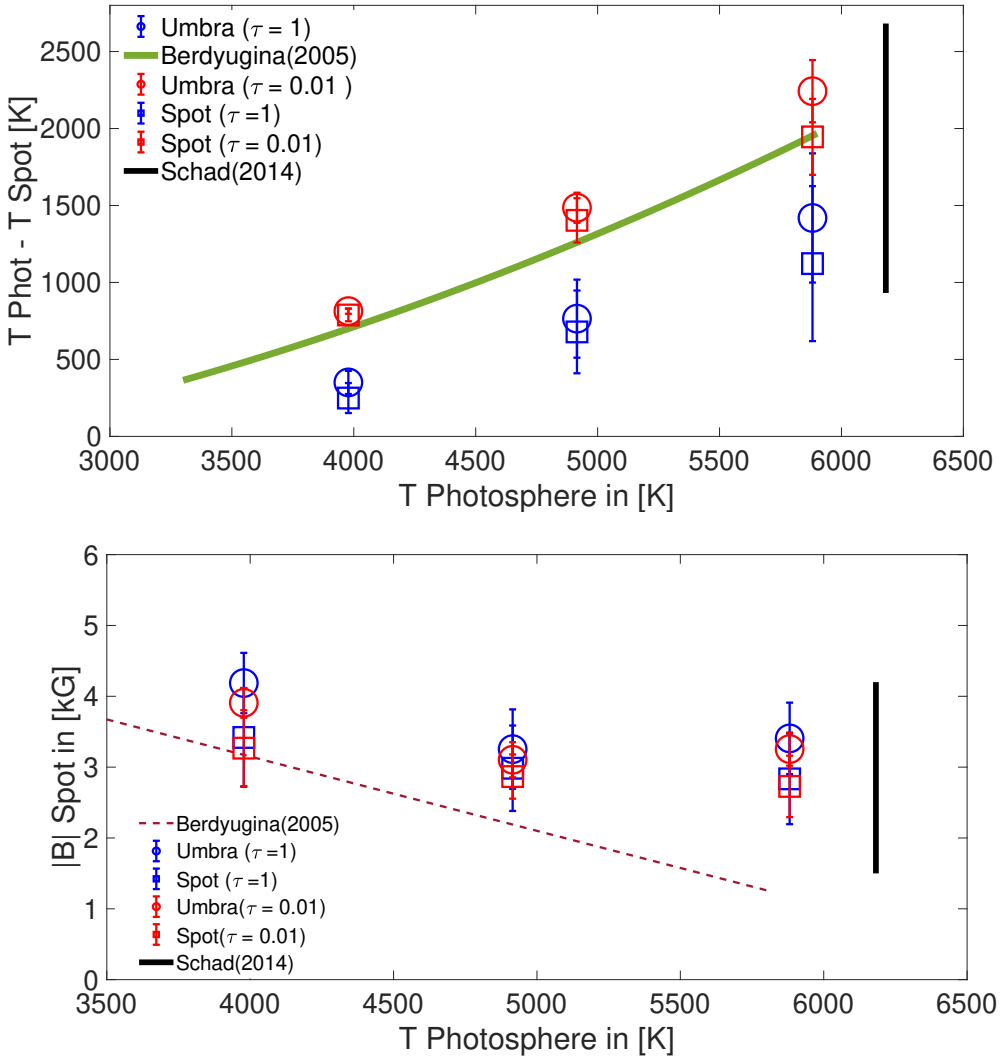


Figure 2.8: Top Panel: Spot (both with and without penumbra) temperature contrasts ($T_{quiet(\tau=1)} - T_{spot(\tau=1,0.01)}$) plotted against photospheric temperature ($T_{quiet(\tau=1)}$). Lower Panel: Spot (both with and without penumbra) magnetic field strengths plotted against photospheric temperature at different $\tau$ heights. The error bars show the standard deviations of the computed averages. The green line in the top panel has been reproduced from Figure 7 of Berdyugina (2005) and is a fit to observed starspot temperatures. The red dashed line in the lower panel has been reproduced from Figure 8 of Berdyugina (2005) and is a fit to magnetic field strengths measured on stellar surfaces. The black line in both the panels represent the range of umbral values (also includes pores) measured on the Sun taken from Schad (2014b) (lower panel, Figure 2).

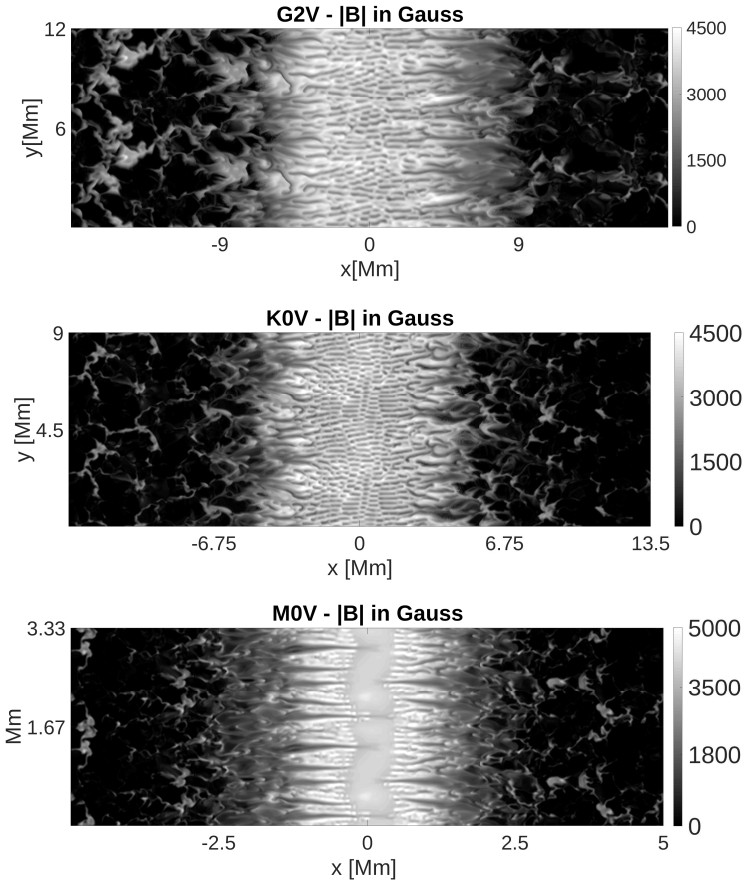


Figure 2.9: Magnetic field strengths, in Gauss, at the $\tau$=1 surfaces of the three simulated stars - G2V, K0V and M0V.

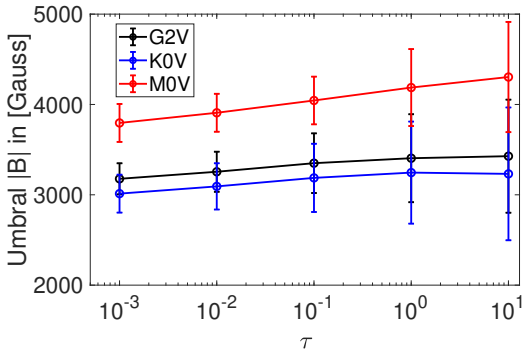


Figure 2.10: Umbral magnetic field strengths, averaged over different iso-$\tau$ surfaces. Black: G2V, Blue: K0V, Red: M0V. The error bars show the standard deviations of the computed averages.

.

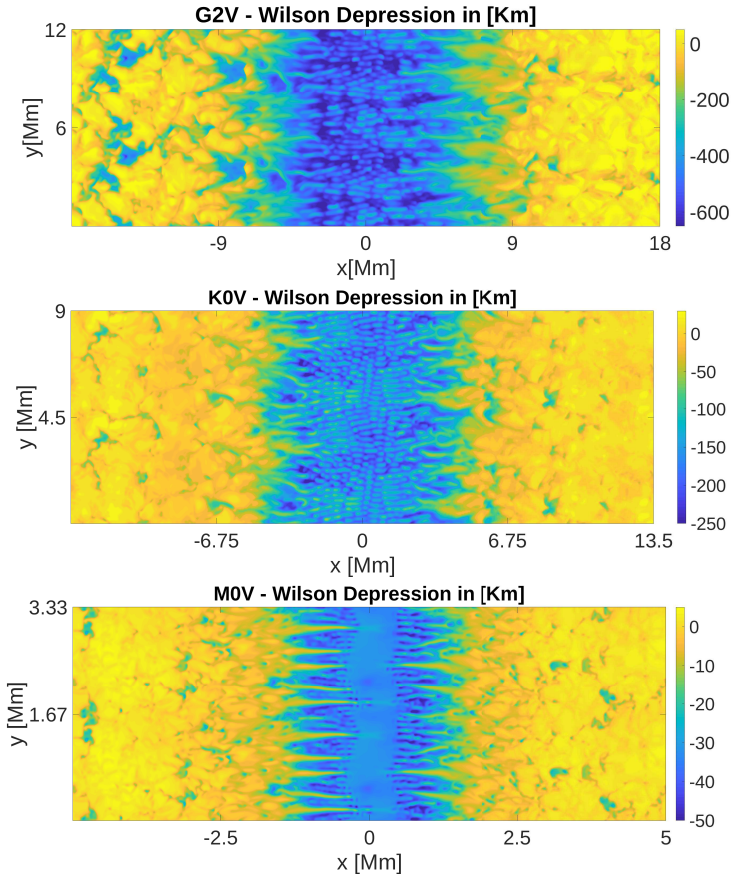


Figure 2.11: Geometric height maps of the $\tau$=1 surface, in km, of the the three simulated stars - G2V, K0V and M0V. Here, zero corresponds to the average height of the quiet star $\tau$=1 surface.

conspicuous of them being - 1) the contrast in the intensity between the granules and the intergranular regions is the most pronounced in the G star and is progressively lower in the cooler K and M stars, 2) the average granule size decreases from the G to the M stars and 3) there are almost no bright magnetic features on the M star. These findings are in line with the results of earlier studies focusing on quiet-star magnetoconvection simulations. Detailed analyses have been done by Beeck et al. (2013b, 2015a) and Salhab et al. (2018b), to which we direct the reader. It is important to note that even though we have performed grey simulations, our results for the quiet star regions are similar to the results obtained by both these sets of papers. Here we focus solely on spot properties.

#### 2.4.1.1 *Identifying the umbra*

For all of the three simulated starspots, we first smoothed the intensity images and then applied intensity thresholds to identify the penumbrae. The lower limits (upper limits) of the intensity thresholds, normalized by their average quiet star intensities were - 0.4 (0.8), 0.6 (0.85) and 0.8 (0.94) for the G2V, K0V and the M0V spot respectively. All points within the inner boundaries of the penumbrae were considered as part of the umbrae. We obtained these thresholds by trial and error, using visual inspection to determine what

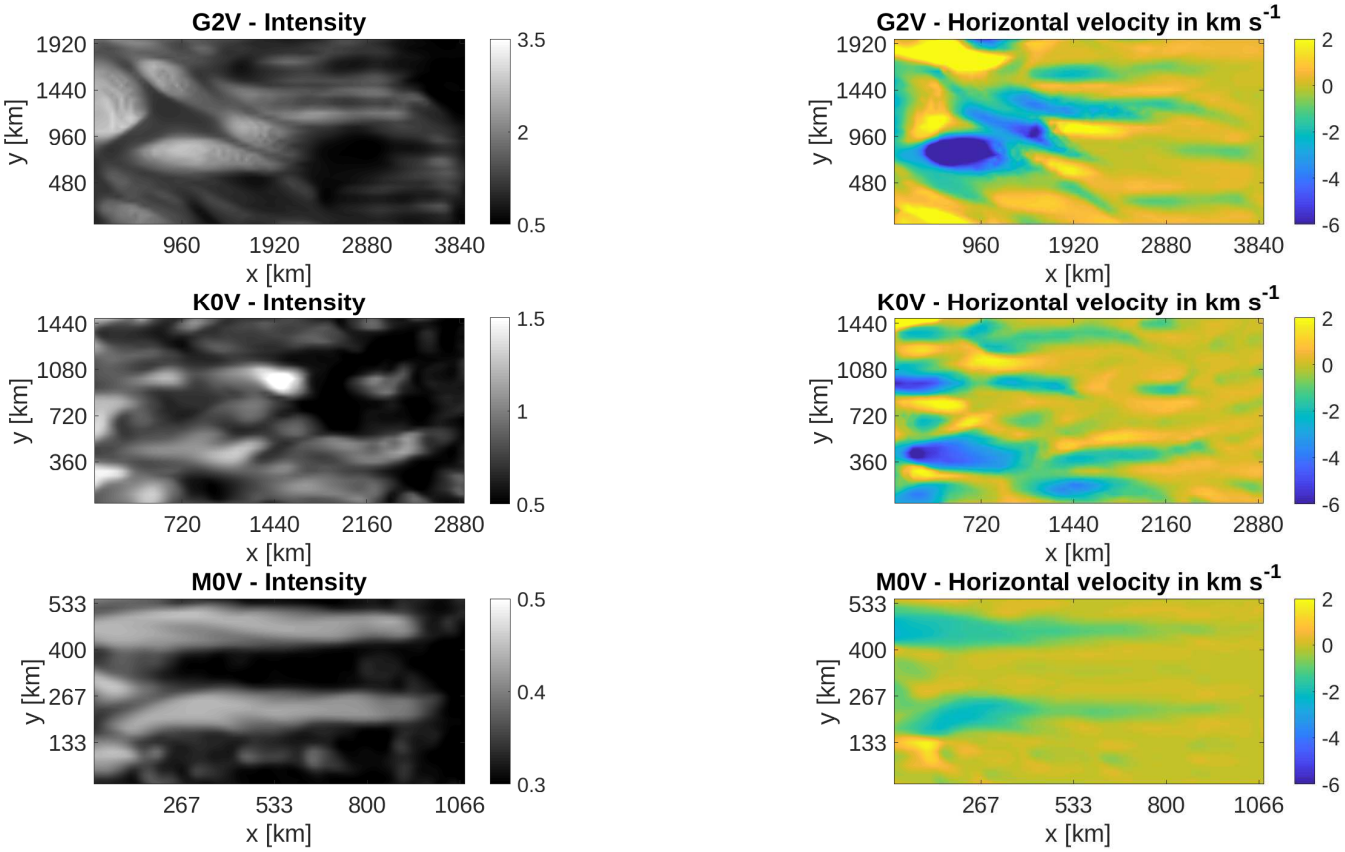


Figure 2.12: The panels on the left show intensity images of sections of penumbral regions, with the umbrae being to the right of the selected regions. The intensities are in units of $10^{10}$ erg cm$^{-2}$ ster$^{-1}$ s$^{-1}$ . The panels on the right show corresponding horizontal velocities in km s$^{-1}$ for the same regions. The color blue indicates flows going towards the left, and yellow indicates flows going towards the right.

thresholds work the best. The results of the intensity thresholds are shown in Figure 2.5, where the penumbral boundaries are marked in red.

Table 2.3: Spatial average of umbral properties.

| Star | $I_{umbra}/I_{quiet}$ | $\|B\|_{tau=1}$(G) | $T_{\tau=1}$(K) | $T_{eff}$(K) |
|---|---|---|---|---|
| G2V | 0.33 | 3406 | 4462 | 4610.8 |
| | (0.1) | (505) | (419.53) | (102.6) |
| K0V | 0.52 | 3254 | 4150 | 4262.5 |
| | (0.09) | (561.3) | (233.6) | (83.6) |
| M0V | 0.71 | 4187 | 3627 | 3622.8 |
| | (0.05) | (426) | (75) | (58.8) |

The averages were computed at the time of our snapshots, with the standard deviations displayed inside brackets.

#### 2.4.1.2 *Relative intensity and temperature of starspots*

Table 2.3 lists the spatially averaged umbral properties at the time of our selected snapshots. The most striking difference between the three simulated starspots is in the intensity contrast between the umbrae of the spots and the surrounding quiet star regions. The spot contrast decreases progressively from the G starspot to the M starspot. The $I_{\mathrm{Umbral}}/I_{\mathrm{Quiet}}$ ratios for the three stars are 0.3, 0.5 and 0.7 for the G, K, and M stars respectively. Not surprisingly, the temperature maps (Figure 2.6) correlate well with the intensity maps. Therefore, following the trend in intensity contrasts, the temperature differences between the spots and the quiet star regions decrease from spectral type G to M.

The umbral dots are noticeably numerous in the maps of G-star and K-star spot temperature and intensity maps than in those of the M-star spot. This points towards the existence of small-scale convective processes underneath the visible surface in the G and K spots. Such processes appear to be comparatively suppressed below the M star umbra.

In Figure 2.7, we have plotted the average umbral, penumbral and quiet stars temperatures at different $\tau$ levels. As expected, there is a monotonic increase in temperature with increasing $\tau$. For $\tau$ >1, the M0V atmospheres (spot and quiet star) show a more gentle increase with optical depth than the G2V and K0V atmospheres.

In the top panel of Figure 2.8, we have plotted the temperature differences between the quiet star photosphere at $\tau$=1 and the spot at the $\tau$ levels 1 (blue) and 0.01(red). Naturally, at $\tau$=0.01 the spots are colder and the temperature contrast between the quiet star photosphere at $\tau$=1 and the spot at $\tau$=0.01 is higher. In our simulations, the periodicity of our boundary conditions inhibits the growth of an expansive penumbra, as the field is forced to point vertically in the upper part of the box near its boundary in the x-direction (due to the virtual presence of another spot with the same polarity outside the domain). In addition, in slab geometry, the penumbra to umbra area ratio is always underestimated, for purely geometrical reasons. Thus, we estimate penumbra-to-umbra area ratios of approximately 1, 0.5, 1 for the G2V, K0V, and M0V spots respectively, while for the Sun observations typically give a ratio of 4-5 (Solanki 2003). This means that those spot temperatures which include contributions from the penumbra (boxes), although warmer, are not significantly different from umbral temperatures(circles). The green line shows a fit to observed starspot temperature contrasts and has been reproduced from Figure 7 of Berdyugina (2005). Simulated spot temperature contrasts at $\tau$ height 0.01, compare well with the fit to the observed data. However, the spot temperature differences at $\tau$=1 show a systematic offset to the line fitted to the observed data points. Note, however, that starspot temperature differences obtained from transit mapping are considerably smaller (e.g. Espinoza et al. (2018), Mancini et al. (2013)), even below the simulated temperature differences at $\tau$ = 1. In any case, the observations and simulations display a remarkably similar dependence of the temperature difference on the host star's effective temperature.

Assuming the solar umbra:penumbra area ratio of 1:4 to hold true for all the three simulated spectral types and using temperatures at $\tau$=1 obtained from our simulations, we predict spot temperatures of 4900 K, 4360 K and 3790 K and therefore quiet star to spot temperature contrasts of 980 K, 560 K, and 190 K for the G2V, K0V, and M0V spots respectively. Further, we can calculate spot to umbra temperature contrasts of 440 K (G2V), 210 K (K0V), and 160 K (M0V).

This increase in spot temperature contrast with stellar surface temperature is an effect

of the strong dependence of opacity on temperature in the near-surface layers of our simulated spectral types. The opacity dependence of temperature is also responsible for the increase in contrast seen between the granular and intergranular regions with increasing $T_{eff}$. We have expanded on this in the Discussion (Section 5).

#### 2.4.1.3 *Spot Magnetic Field Strengths*

Figure 2.9 depicts magnetic field strength maps at the optical surface of the three stars. At the time when we took the snapshots, the M-star spot had the highest umbral average field strength, around 4200 Gauss, and the G and K starspots have average umbral field strengths of around 3400 Gauss and 3200 Gauss respectively.The umbral magnetic field distribution is highly non-uniform in both the G and K spots and shows a lot of fine structure, which is related to the fine structure also seen in the surface temperature maps (Figure 2.6) and is caused by the presence of umbral dots.

Figure 2.10 shows the umbral magnetic field strengths averaged over different iso-$\tau$ surfaces. The M0V spot shows a slight but steady increase in field strength with increasing optical depth. The magnetic field strengths for the G and K spots do not show much variation with increasing $\tau$ and becomes almost constant below $\tau$=1.

In the bottom panel of Figure 2.8 we have plotted our obtained average spot field strengths at the heights where $\tau$ = 1 and 0.01. The red line is a fit to field strengths measured on different stars and has been reproduced from Figure 8 of Berdyugina (2005). It is important to note that the observations are of field strengths averaged over large portions of stellar surfaces and therefore have, probably large, contributions from magnetic fields outside starspots as well. Also, the linear fit in Figure 8 of Berdyugina (2005) does not include the solar umbral field strength. Therefore, it is not surprising that our simulation results do not agree very well, although the general trend does show some similarity.

#### 2.4.1.4 *Wilson Depression*

The presence of strong magnetic fields causes a reduction in the local gas pressure and consequently a reduction in the gas density. The reduction in temperature, because of the inhibition of convection, also causes a drop in the opacity. The absorption coefficient($\kappa\rho$), which is the product of the gas density and the opacity, naturally drops. This allows us to see deeper into the star within the starspot and this depression of the optical surface is called the Wilson depression. Figure 2.11 shows the depth of the Wilson depressions of the three spots. The optical surface of the G2V spot is the most depressed and the value of the Wilson depression in the umbra drops by roughly an order of magnitude from the G2V to the M0V spot. The average Wilson depressions of the G, K and M umbral regions are 515, 161 and 34 km respectively. This difference in Wilson depression is a combination of several factors - the difference in pressure scale heights among the stars, the plasma-$\beta$ ratio and the temperature dependence of opacity. We have explored this further in the Discussion.

#### 2.4.1.5 *Penumbral Filaments*

The periodicity of our boundary conditions in the horizontal directions implies that our positive spots effectively sit between two other spots of the same magnetic polarity. This

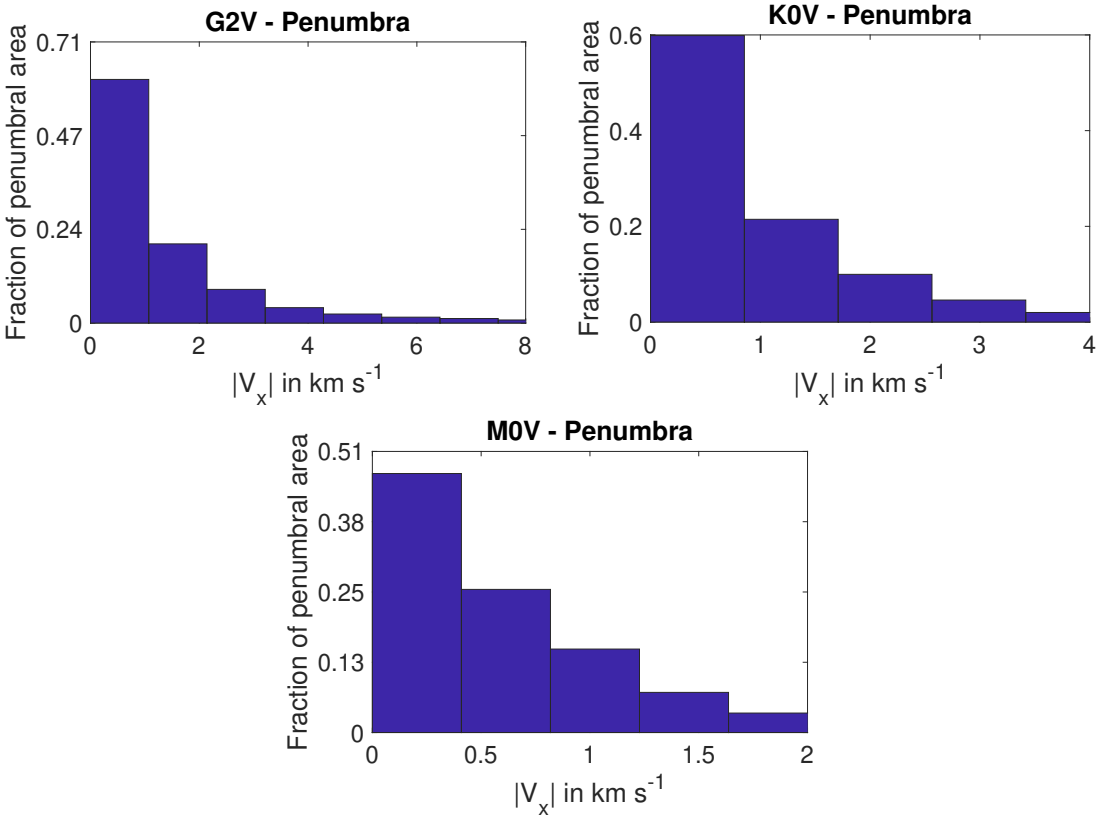


Figure 2.13: Histograms of Evershed flow speeds, in, from top to bottom, the G2V, the K0V and the M0V starspots, calculated using the areas marked as penumbrae in Figure 2.5.

hinders the full development of penumbrae in all three cases. Nevertheless, we present here some results from our obtained penumbrae.

The left-hand panel of Figure 2.12 shows the intensity images of segments from the penumbral regions, while the right-hand panel shows the associated horizontal flow velocities in the same regions. All of the three spots show penumbra like features. The K0V penumbral filaments are similar to filaments observed on the Sun - elongated with thin dark cores in the middle. The M0V filaments do not develop dark cores and are more homogeneous. The average intensities of the penumbral regions, normalized by their quiet star intensities, and their average Evershed flow speeds have been listed in Table 2.4. Like the umbra, the relative intensity of the penumbra increases from the G2V to the M0V star. Plotted in Figure 2.13 are the histograms of the Evershed flow speeds. For all the three spectral types, the distributions are skewed with only a very small fraction of the penumbra having high horizontal velocities. The G2V penumbral Evershed flows are the fastest with the maximum value reaching almost 8 km $s^{-1}$. In the K0V penumbra, they reach 4 km $s^{-1}$ while the M0V penumbra has the slowest Evershed flows with the maximum value reaching only $\sim$ 3 km $s^{-1}$. The average sound speed at the photospheres is roughly 8 km $s^{-1}$, 7 km $s^{-1}$ and 5 km $s^{-1}$ for the G, K and M stars, respectively. So, while penumbral flows on the G2V star reach supersonic speeds, penumbral flows on the K0V and M0V stars are always subsonic.

Table 2.4: Average penumbral properties with spectral type.

| Star | $I_{penumbra}$/$I_{quiet}$ | Evershed velocity(km $s^{-1}$) | $T_{tau=1}$(K) |
|---|---|---|---|
| G2V | 0.57 | 1.32 | 5007 |
| | (0.2) | (1.58) | (564) |
| K0V | 0.71 | 1.00 | 4412 |
| | (0.15) | (1.06) | (298)) |
| M0V | 0.88 | 0.59 | 3833 |
| | (0.07) | (0.52) | (115) |

The standard deviations are in brackets. The areas marked as penumbral regions in Figure 2.5 were used to compute the averages.

### 2.4.2 Subsurface Properties

Figures 14 to 19 show the variation of starspot properties with depth, averaged horizontally along the width of the simulation boxes.

We have shown only the first few relevant pressure scale heights in the following figures.

#### 2.4.2.1 *Temperature Structure*

Figure 2.14 shows the variation of temperature with depth. In the quiet star regions, there is a sharp vertical gradient in temperature with depth, at the photosphere of the G star, where the temperature rises from ~ 6000 K at the surface to ~ 9000 K within a span of half a pressure scale height. This gradient is weaker for the K star and smoothest for the M star. In the M star, the temperature rises by a mere 2000 K over 2 pressure scale heights, from ~ 4000 K at the photosphere to ~ 6000 K at a depth of 2 pressure scale heights. It is important to note that the opacity due to the ionization of $H^-$ is the main source of continuum opacity in the surface layers of cool main-sequence stars. The $H^-$ opacity shows a steep temperature dependence in the range 3000 - 8000 K and therefore, the vertical temperature gradient plays an important role in determining the observed intensity contrasts.

Inside the spots, the reduced temperatures also diminish the pressure scale heights and this is evident in Figure 2.14. Below a certain depth, the temperatures inside the spots of all three spectral types become indistinguishable from their surroundings.

#### 2.4.2.2 *Plasma-Beta and Convection*

The ratio of the gas pressure (P) to the magnetic pressure ($B^2/8\pi$), called the plasma-$\beta$ ratio, has been plotted in Figure 2.15. Inside all of the spots, the plasma-$\beta$ ratio is close to unity around the surface. The atmosphere above the M0V spot is less evacuated (the ratio is around 0.1 just above the surface) than the G2V spot, where the ratio drops to below 0.01 within a span of 2 pressure scale heights. This plays a role in the G2V spot having a much more depressed optical surface.

The depth dependence of the magnitude of the velocity field, $|v| = (v_x^2 + v_y^2 + v_z^2)^{\frac{1}{2}}$, averaged along the y-axis of the box is shown in the Figure 2.16. Convection is suppressed

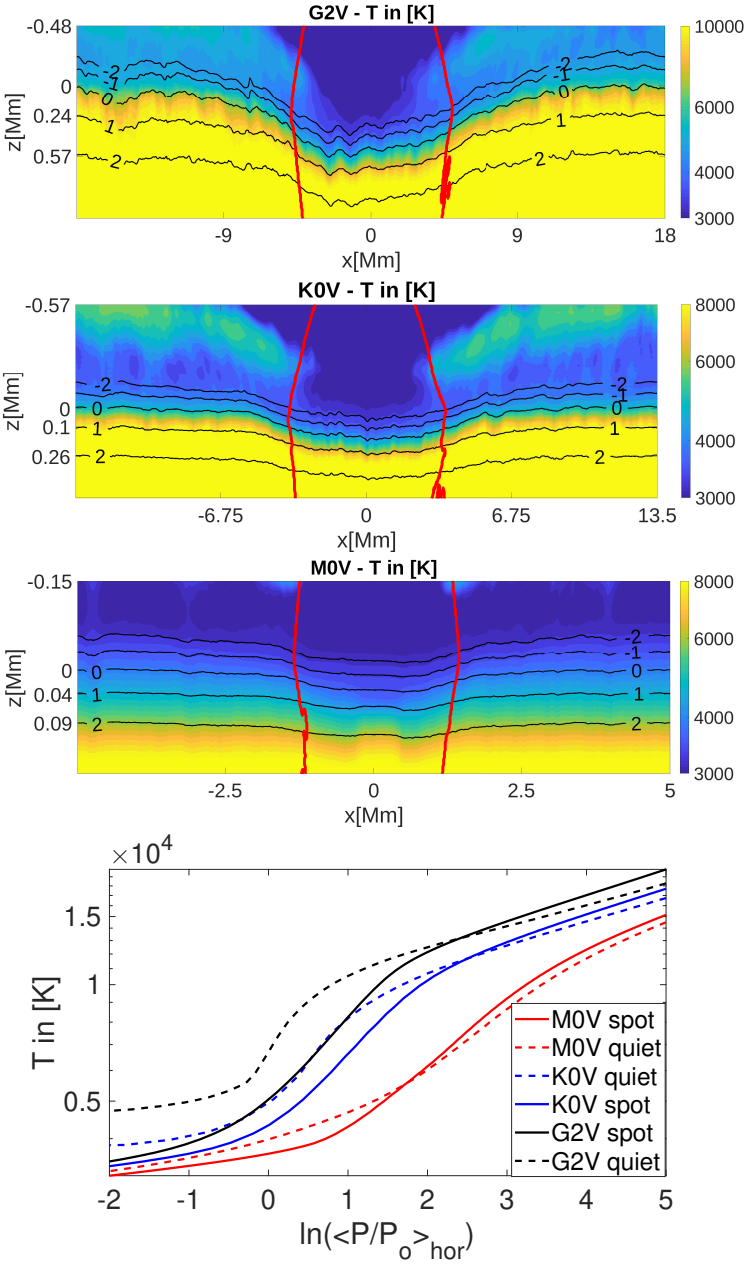


Figure 2.14: First 3 panels from the top: Temperatures, in Kelvin, plotted with depth, averaged horizontally over iso-z surfaces along the y-axis of the box. Overplotted on all of the figures are contours of $\log_e(< (\frac{p}{p_0}) >_y)$, where p is the pressure and $p_0$ is the pressure at $\tau = 1$ at every column of the atmosphere. The red contours mark the boundary of |B| = 2000 Gauss. The x-axes show the distances in Mm along the length of the box, while the z-axes mark the geometrical heights with respect to the optical surface. We have shown only the first few relevant pressure scale heights. Bottom panel: 1D horizontal averages (along x and y) of umbral and quiet star temperatures plotted against pressure scale height.

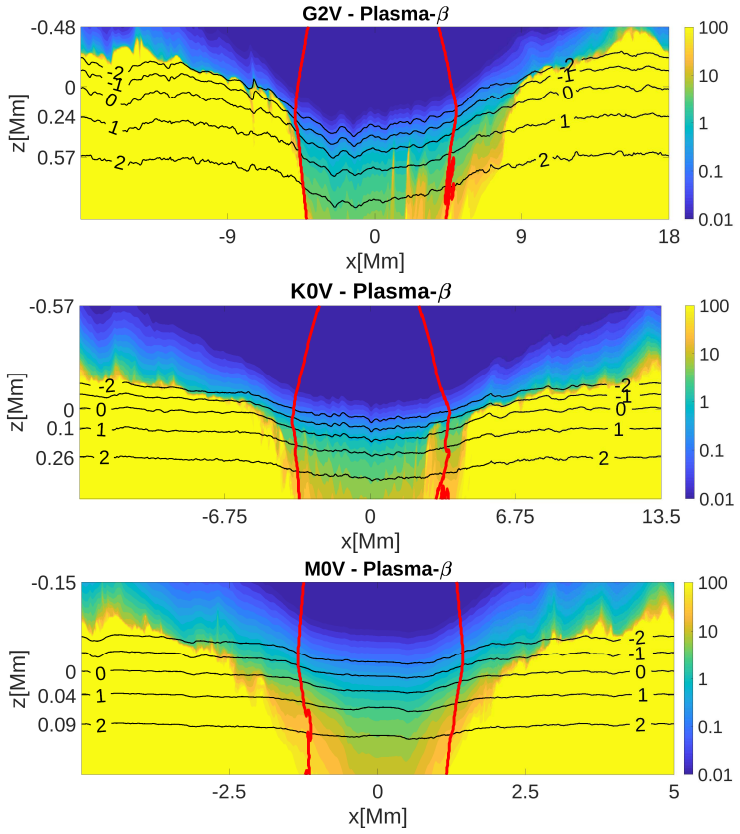


Figure 2.15: The, horizontally averaged, plasma-$\beta$ ratio - $\frac{8\pi P}{B^2}$. The black and red contours are the same as in Fig: 2.14.

because of the presence of strong magnetic fields and the average velocities inside the umbra drop roughly by a factor of 10, for all the three spots. The G spot has average photospheric velocities of around 4 km s$^{-1}$ and inside the umbra the convection is reduced to around 0.3 km s$^{-1}$. Similarly for the M star, the photospheric convective velocity of around 1 km s$^{-1}$ is reduced to less than 0.075 km s$^{-1}$. The K star has velocity fields of around 2.5 km s$^{-1}$ at the surface which are reduced to around 0.3 km s$^{-1}$ inside the spot umbra.

#### 2.4.2.3 *Radiation Field*

Figure 2.17 shows the horizontally averaged absorption coefficient($\kappa\rho$) of the stellar atmospheres. In the quiet star regions, we find that the transition from optically thin to thick takes place over a larger number of pressure scale heights for the cool M star, while for the G star this change is much more rapid. This is also reflected in the vertical component of the radiative flux which is plotted in Figure 2.18. The radiative flux has been normalized at every point by the final radiative flux leaving the box above the quiet star regions. This value rises from less than 1 % to nearly 100 % over a single pressure scale height for the quiet G2V atmosphere. The transition from radiative to convective energy transport is much more gradual for the cooler M star and takes place over several pressure scale heights. For the K star the transition rate lies between the M and G stars.

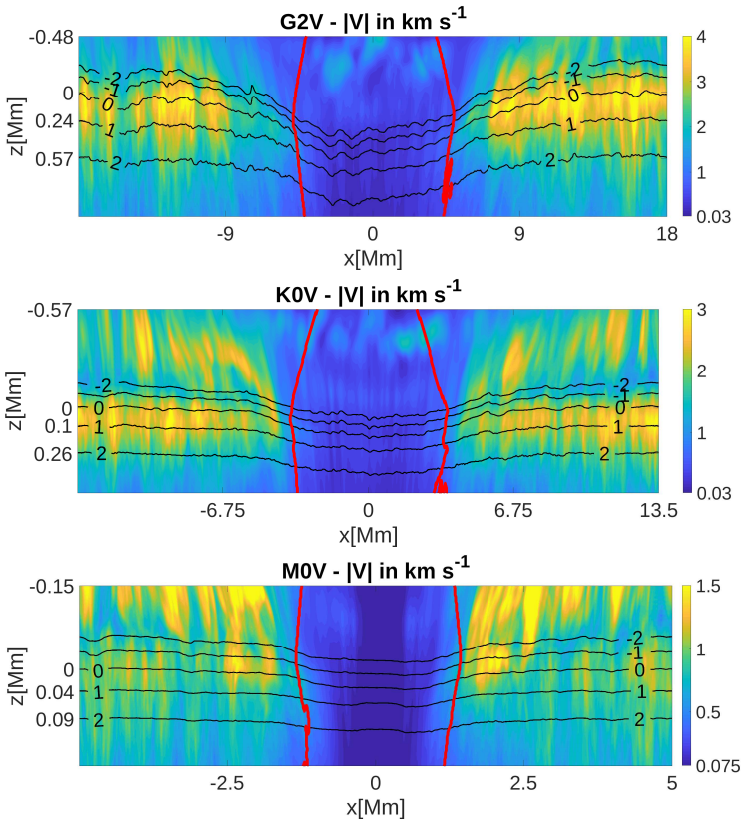


Figure 2.16: The, horizontally averaged, magnitude of the velocity field ($|v| = (v_x^2 + v_y^2 + v_z^2)^{\frac{1}{2}}$) in units of km s$^{-1}$. The black and red contours are the same as in Fig: 2.14.

In the quiet G2V atmosphere, the energy transport by radiation is negligible (< 1% of the flux leaving the box) at a depth of 1 pressure scale height, whereas in the spot atmosphere the radiative flux is already at 10% at a similar depth. Clearly, the radiative properties inside the G starspot are very different from the radiative properties of the G quiet star atmosphere. However, the differences between the M spot atmosphere and its surroundings are not that pronounced. The radiative properties of the K spot lie between the M and G starspots.

Figure 2.19 plots the radiative heating rates for the different stars with depth. In the G star the cooling is much more concentrated and intense near the photosphere, while the radiative cooling for the M star is spread out over a larger vertical extent. However inside the spots, the radiative cooling is spread out over almost 2 pressure scale heights for all of the spots. The spots are at much lower temperatures and therefore their cooling rates are lower as well.

## 2.5 Discussion

### 2.5.1 Spot Temperature Contrast

The results of our simulations reveal a clear pattern in starspot intensity contrasts. There is a monotonic decrease in contrast from the hottest to the coolest star. This is also seen in

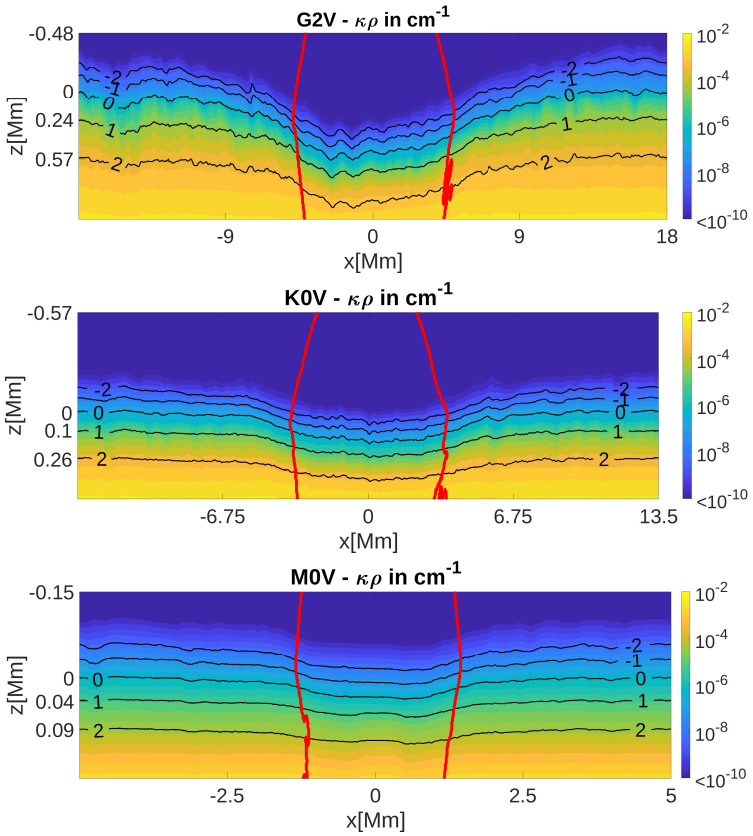


Figure 2.17: The absorption coefficient ($\kappa\rho$), averaged horizontally, computed in units of $cm^{-1}$. The black and red contours are the same as in Fig: 2.14.

the list of starspot temperature measurements compiled by Berdyugina (2005). This trend can be explained by the dependence of opacity on temperature. In the context of stellar near-surface simulations, this has been described by Nordlund and Dravins (1990a), Beeck et al. (2013a), Magic et al. (2013b), Salhab et al. (2018b). The opacity at the surface of cooler stars is largely governed by $H^-$ ions and in the temperature range 3000 - 6000 K, the $H^-$ opacity is approximately proportional to $T^9$ (Hansen and Kawaler 1994). Thus, the opacity of $H^-$ increases much more sharply with temperature in the hotter G2V surface (6000 K) in contrast to the cooler photospheres of K (5000 K) and M (4000 K) stars. Therefore, in the hotter G2V quiet star atmosphere, a slight increase in temperature with depth causes the opacity to rise sharply. This results in a sudden change from convective energy transport to radiative energy transport in the hotter G2V star within a span of half a pressure scale height, whereas this change, from convective to radiative energy transport, is the most gradual for the M0V case and is spread over nearly 2 pressure scale heights

When we introduce strong magnetic fields in the G2V star, the transport of energy upwards by convection is hindered. Since convection is the primary mode of heat transport below the photosphere in the G2V star, the temperature of the umbra is lowered substantially. As a consequence, the opacity falls sharply and the increased effectiveness of radiation also contributes to lowering the temperature. On the other hand, in the M0V star, where radiation already plays a substantial role in energy transport below the photo-

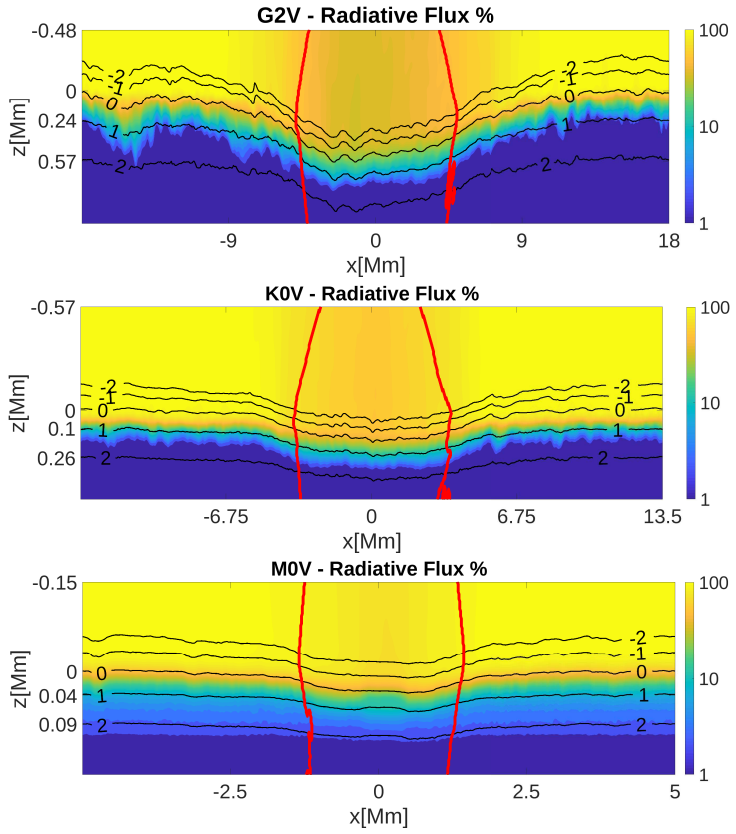


Figure 2.18: The vertical component of the radiative flux, expressed a percentage of the average radiative flux leaving the box above the quiet star regions. The black and red contours are the same as in Fig: 2.14.

sphere, the magnetic fields have a smaller impact on the energy transport. Also at 4000 K, the surface temperature of the M0V star, the opacity is less dependent on temperature and on introducing magnetic fields, there is only a small change in radiative properties of the medium as seen in Figures 2.17, 2.18 and 2.19.

This explains why the G starspot has the highest temperature contrast, and the M spot is not as cool as one would naively expect it to be. The radiative properties of the K star atmosphere lie in between the M and the G star and this is reflected in the K spot temperature contrast as well.

### 2.5.2 Wilson Depression

The Wilson Depression of the starspots varies significantly with spectral type - 500 km for the G2V spot to around 30 km for the M0V spot. This can be explained largely by the difference in pressure scale height between the stars. The pressure scale heights, near the surface, of the quiet star atmospheres are 230 (G2V), 100 (K0V) and 40 km(M0V). However, the Wilson depression when expressed in terms of pressure scale height also exhibits significant differences - the G2V umbra is more than 2 pressure scale heights deep, whereas the M0V umbra is less than a pressure scale height deep. Similar variations of the Wilson depression with spectral type, were also observed in small flux tubes embedded

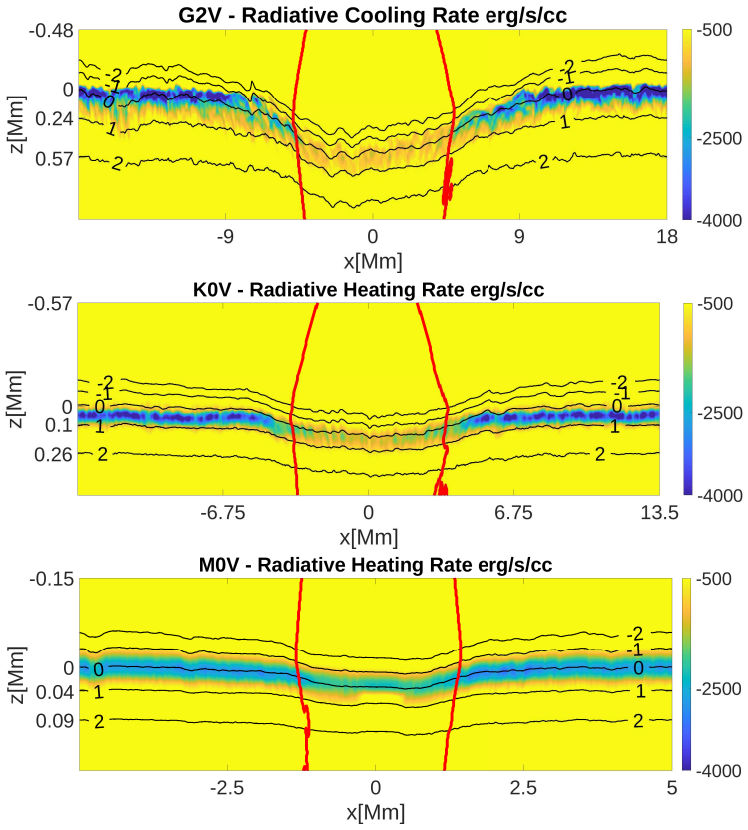


Figure 2.19: Radiative heating rates, averaged horizontally, in erg cm$^{-3}$ s$^{-1}$. The black and red contours are the same as in Fig: 2.14.

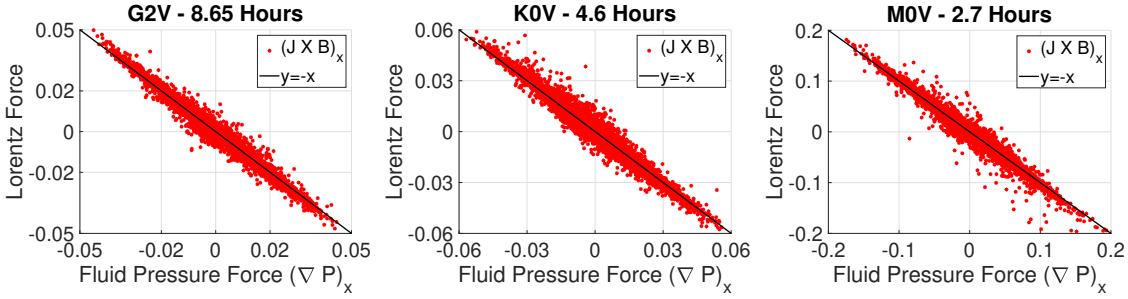


Figure 2.20: Scatter plots of the magnetic forces against the fluid pressure forces at constant geometrical depths. The horizontal cuts were taken at depths which corresponded to the average Wilson depression of the umbrae

.

in the intergranular regions in the simulations of Beeck et al. (2013b) and Salhab et al. (2018b).

The substantial depression of the optical surface in the G2V spot compared to the M0V spot can be explained by the difference in the absorption coefficient inside and outside the spot. At the same geometrical height, the absorption coefficient (plotted in Figure 2.17) drops by several orders of magnitude inside the G2V spot. This is not the case for the M0V spot. The M0V star has a higher surface pressure ($\sim$ 5 times that of the G2V star)

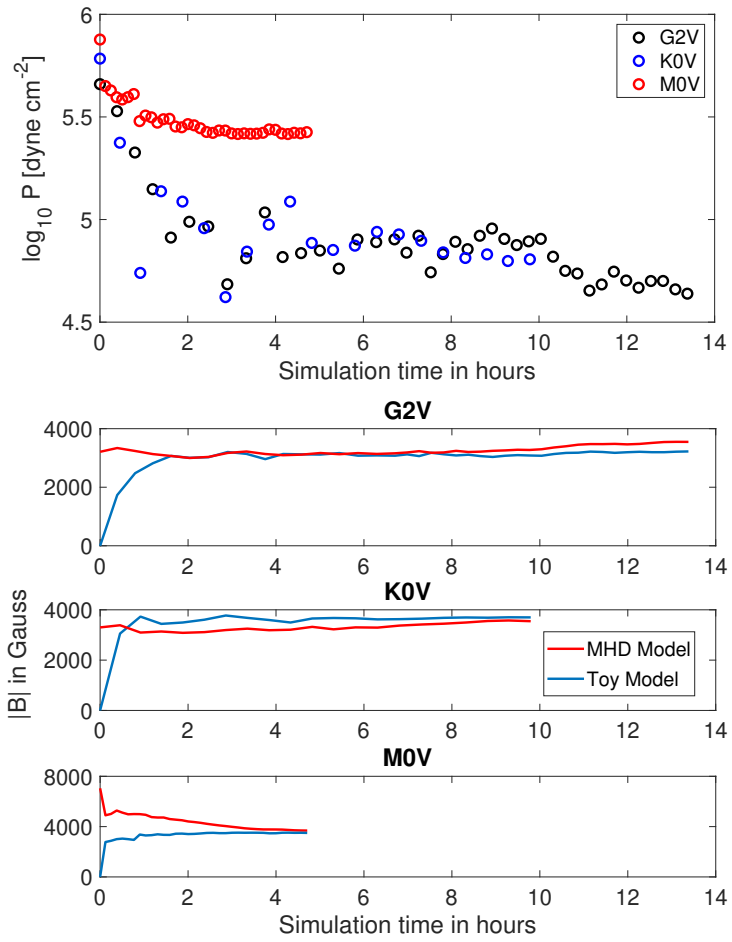


Figure 2.21: The first panel shows the evolution of average fluid pressure with time in a box close to the optical surface inside the starspots. The three bottom panels plot the average magnetic field strength in the box (red curves) and the field strength one would expect (blue curves) from the drop in fluid pressure ( $\sqrt{8\pi(P_t - P_{initial})}$).

and therefore the gas is less evacuated in the M spot atmosphere, in spite of its larger field strength. This is reflected in the plasma-$\beta$ ratio - $8\pi P/B^2$ (see Figure 2.15) above the M0V spot. In addition, the weaker dependence of opacity on temperature in the 3000 - 4000 K range means that the opacity inside and outside the M0V spot are comparable. This results in the much smaller depression of the M-spot optical surface.

### 2.5.3 Umbral Magnetic Field Strength

The umbral field strengths of the starspots lie between 3 and 4.5 kG. The difference between the average umbral field strengths of the M0V spot and the G2V spot is only around 700 Gauss despite the surface pressure of the M star being 5 times higher. This is related to the change in the magnitude of the Wilson Depression with spectral type.

In Figure 2.20 we have plotted the $x$-component of the Lorentz force against the $x$-component of the fluid pressure force at a constant geometrical depth close to the optical surface of the spots. If we assume magnetostatic equilibrium, $\nabla(P)$ and $J \times B$ should

have equal values and opposite signs. The $y = -x$ line shows a good fit to the points and this shows the simulated spots are close to magnetostatic equilibrium at their respective optical surfaces.

Further, we have constructed a simple model to predict the umbral field strength assuming pressure balance. For each of the three spots, we take a small region inside the starspots near the optical surface and plot the fluid pressure with time (top panel in Figure 2.21).

If $P_0$ is the initial pressure, then $P_0$ - $P_t$ (pressure at time t) would give us the pressure of the displaced gas. Equating $P_0$ - $P_t$ with $\frac{B^2}{8\pi}$ would give us an expected magnetic field strength. In the lower three panels of Figure 2.21, we have plotted the expected magnetic field strength and the actual field strength obtained in this box, with time. After an initial transient phase, the field strengths we obtain from our simulations are comparable to what is predicted by a simple pressure equilibrium model.

The measured umbral field strength is thus a result of two competing effects – the gas pressure of the star and how deep we are seeing into the star. As we move from the G2V to the M0V star the surface pressure increases, which would mean higher umbral field strengths, while the atmosphere becomes less vacuous and more opaque, which would lower the measured umbral field strengths. In the case of the K0V star, the effect of the absorption coefficient becoming higher wins over the competing effect of increased surface pressure ( 1.8 times the G2V case) and therefore the umbral field strength of the K0V starspots (2D and 3D) is lower than the G2V starspots. Whereas for the M0V star, the gas pressure is high enough ( 5 times the G2V case) that we still record higher umbral field strengths. We have further demonstrated this with a simple calculation.

Let the pressure at the surface of the G2V star be Po. So the surface pressures of the K0V and the M0V stars would roughly be 1.8Po and 5Po respectively. The Wilson depressions of the G2V, K0V, and M0V starspots, when expressed in terms of pressure scale height (Hp) are – 2.25, 1.61, and 0.85 respectively. This means, at the heights where the optical surfaces of the three spots form, the ambient gas pressures would be approximately Po exp(2.25), 1.8Po exp(1.61) and 5Po exp(0.85). This yields values of 9.5Po, 9.0Po, and 11.7Po for the G2V, K0V, and M0V stars respectively. Although this calculation is very simplistic, it explains the trend in umbral field strengths very well.

## 2.6 Summary and Conclusion

We have performed the first-ever, ab-initio radiative MHD simulations of spots on cool main-sequence stars of the spectral types G2V, K0V and M0V. We investigated the variation of fundamental spot properties - temperature, intensity and magnetic field strength with spectral type. Our main findings can be summarized as follows -

1) Our simulations show that the temperature contrast between a starspot and its surrounding photospheric environment is a function of the stellar surface temperature. The hotter the stellar surface, the higher is the spot temperature contrast. Obviously, this trend is reproduced in the intensity contrast as well. Our analysis has revealed that the variation in spot contrast with spectral type can be attributed to radiative processes playing an increasingly dominant role in the atmospheres of cooler stars. This is because as we

progress to cooler stars the ionisation of $H^-$ takes place at greater pressure scale depths, making the atmosphere near the surface more transparent, thereby smoothing out both horizontal and vertical fluctuations in temperature. Our starspot simulation results are consistent with the larger picture that cooler the stellar surface, lower are the variations in temperature and intensity.

2) Our simulated umbral field strengths for all the spectral types lie in the 3-4.5 kG range. The umbral field strength is largely determined the fluid pressure at the depth where the $\tau = 1$ surface of the spots form. The optical surface of the G2V starspot is more than 2 pressure scale heights deep whereas the optical surface of the M0V starspot is less than 1 pressure scale height deep. This explains why M stars and G stars have umbral field strengths that are not too different.

3) Prior to conducting 3D simulations, we carried out 2D studies, where we varied the initial conditions of our magnetic flux tubes extensively. Although our 2D starspots display slightly different values of temperature and field strength, they reproduce the trends seen in the intensity contrasts in our 3D simulations very well. In addition, they also show that our obtained trends in spot temperatures and magnetic field strengths do not depend crucially on our choice of initial conditions.

4) All the simulated starspots develop penumbral filament-like structures. The filaments of the K0V spot look similar to solar penumbral fiaments, with thin dark cores running along the centre of the filaments. The M0V penumbral filaments are more homogeneous and do not develop such dark cores. The Evershed speeds decrease progressively from the G2V spot to the M0V spot.

We expect our calculations to help understand the variability of G-M main-sequence stars, which is largely determined by starspots on rotational timescales. Conversely, our starspot models provide useful priors for reconstructing stellar spottedness based on light-curve modeling and (Zeeman) Doppler Imaging. Our results will also aid the hunting of exo-planets. Starspot intensity contrasts are important in the exoplanet detection process as spots and planets both reduce the amount of light we receive from a star. Our constraints on spot temperatures should also be useful in interpreting maps of stellar magnetic fields derived using Zeeman Doppler Imaging. In addition, we expect our starspot properties to help improve estimates of the total magnetic flux on lower main-sequence stars, thus setting improved constraints on the efficiencies of stellar dynamos.

Future work may involve using non-grey radiative transfer to enable the synthesis of spectral lines. Additionally, simulating spot pairs of opposite polarities would facilitate the formation of more expansive penumbrae and therefore better constraints on starspot properties.

# 3 3D Radiative MHD simulations of starspots II: Synthetic spectral lines, Effect on Radial Velocity

## 3.1 Introduction

The mapping of temperature and magnetic field inhomogeneities on stars, other than the Sun, is a notoriously difficult endeavour. The difficulty stems primarily from the lack of spatial resolution and one has to solve inverse problems, that often hinge on a priori assumptions, to glean information concealed in disk integrated spectra. Fortunately, the Doppler effect can be exploited to disentangle surface features of a rapidly rotating star. Different longitudes have different line-of-sight velocities and therefore they leave their imprints at different wavelength points on a rotationally broadened absorption line profile. The Doppler effect, combined with the modulation of the Stokes I profile brought about by temperature variations, is used by the Doppler Imaging technique (Goncharskii et al. 1977a, Vogt and Penrod 1983) to infer stellar surface temperature maps. The same principle is applied to Stokes V profiles in the Zeeman Doppler Imaging method to generate surface magnetic field maps (Semel 1989a, Donati et al. 1989, Brown et al. 1991). Both these techniques rely on synthesizing Stokes I and V profiles of magnetic and non-magnetic regions at different disk locations, which serve as initial input profiles to the inversions. These profiles are currently poorly constrained due to insufficient knowledge about starspot atmospheres and temperatures.

The spectrum emerging from a star has applications beyond stellar physics. It is also used (Mayor and Queloz 1995) to detect exoplanets orbiting a star. As a planet orbits around its host star, the gravitational pull of the planet makes the star wiggle about its axis. This can be measured through changes in the radial velocity (RV), which leaves its signature in the star's spectral lines. However, variations in RV can also be induced by stellar hydrodynamic activity like granulation and oscillations (Butler et al. 2004, Dumusque et al. 2011), and magnetic activity in the form of spots and active regions (Lagrange et al. 2010, Meunier et al. 2010, Dumusque et al. 2014b, Borgniet et al. 2015, Bauer et al. 2018). In fact, what was once thought to be a rocky planet in the habitable zone of an M dwarf, later turned out to be starspots rotating across the stellar disk (Robertson et al. 2014). The most obvious way a starspot rotating across the disk changes the RV signal, is by causing a reduction in the number of photons coming from one side of the star and thereby breaking the rotationally induced symmetry between red and blue shift. Further, starspots locally suppress convective motions and this causes a change in the

net convective blueshift. Although, there have been efforts towards quantifying the RV caused by convective motions using realistic MHD simulations (Cegla et al. 2013), the effect that starspots have on RV has been studied only using simplistic 1D atmospheres or blackbody spectra (Hatzes 2002b, Desort et al. 2007, Lagrange et al. 2010). Also, the possible contribution from the penumbra to the RV signal (on the Sun, a spot is typically 80 % penumbra (Solanki 2003)) has been completely ignored so far. The penumbra harbours flows both along the line-of-sight and perpendicular to it (Tiwari et al. 2013). As a spot gradually moves across the disk, the horizontal Evershed flow (typically in the km/s range) begins to have a line-of-sight component. Whether penumbral flows near the limb can significantly affect RV signals has not been explored yet.

The discussion above makes it abundantly clear that better constraints on Stokes I and V profiles of individual starspots on different spectral types are the need of the hour. The recent 3D radiative MHD simulations of starspots (Panja et al. 2020) presents us with the unique opportunity to do just that - compute realistic Stokes I and V line profiles of individual starspots and their components - the umbra and the penumbra at different locations on the stellar disk. Further we can combine them with quiet star line profiles to study the effect of starspots on disk-integrated stellar absorption line profiles.

For this study, we have chosen atomic absorption lines from two different parts of the spectrum, a Fe-I line pair from the visible range (630.2 nm) and a Ti-I line from the near infrared (2231.06 nm). While magnetic field measurements are much easier towards the infrared as the Zeeman effect is proportional to the square of the central wavelength of the line, temperature contrasts are poorly captured in the infrared because the Planck function changes slowly at larger wavelengths. This is not the case for lines in the visible range and these lines are often exploited to determine starspot temperature contrasts (see Catalano et al. (2002c), Frasca et al. (2008)). We specifically chose the Fe I pair at 630.2 nm for our synthesis in this chapter because of its widespread use in solar physics. The *Hinode* mission (Kosugi et al. 2008) provided the full Stokes parameters of this Fe-pair and they have been extensively studied for both magnetic and non-magnetic regions on the Sun. The Ti-I line at 2231.06 nm, besides being a useful tool in solar physics (for example, see Rüedi et al. (1998)), is routinely used to infer magnetic field strengths on T Tauri stars, which comprises G, K and M stars (for example, Lavail et al. (2019)).

In this chapter, we present the first computations of Stokes I and V profiles of the above-mentioned atomic lines using realistic 3D starspot atmospheres that properly capture the effect of temperature, magnetic field, velocity and their gradients. We set out to answer the following questions in this chapter - 1) What do absorption line profiles of spots on early K and M stars look like and how do they differ from sunspot line profiles? 2) How do these line profiles change as starspots move across the stellar disk? 3) How much do spots affect disk integrated line profiles emerging from a star? 4) At what filling factors do starspots induce RV changes large enough to hinder the detection of exoplanets?

The methods employed are described in Section 3.2, followed by a brief discussion of continuum contrasts of the starspots at various viewing angles in Section 3.3. The line profiles synthesized at disk centre are discussed in 3.4, and their centre-to-limb variations in 3.5. In Section 3.6 we have mixed average spot line profiles with quiet star line profiles and computed the effect of spots on radial velocity and finally in Section 3.7 we have summarized this chapter and presented our conclusions.

## 3.2 Methods

We use non-gray simulations to recompute the stellar atmospheres starting from the gray MURaM simulations presented in Panja et al. (2020). We ran our simulations until the net outgoing radiative flux stabilizes, after its initial drop. This stabilization happens in less than 5 mins of stellar time and we ran all three spectral types for more than 10 mins of stellar time. Nonetheless, the $T_{\rm eff}$ of the non-gray simulations are cooler by around 20-30 K compared to the gray runs, for all of the spectral types. We subsequently calculate synthetic spectral lines using the STOPRO (STOkes PROfiles) code (Solanki 1987, Solanki et al. 1992, Frutiger et al. 2000), which operates under the assumption of local thermodynamic equilibrium. We computed the Stokes profiles of two Fe-I lines at 630.15 and 630.25 nm, with Landé g factors of 1.67 and 2.50 respectively. The Ti-I line at 2231.06 nm has a Landé factor of 2.50. The line parameters fed into STOPRO were downloaded from the VALD database (http://vald.astro.uu.se/).

We have computed the average Stokes I and V profiles of four distinct regions - the umbra, the penumbra, the quiet star and the magnetic quiet star, representing facular or plage regions. To demarcate these regions, we used the continuum intensity images of the three starspots, at 630 nm, normalized by the quiet star continuum intensity (shown in the left panels of Figure 3.1). We first smoothed the images and then applied intensity thresholds to find the contours of the penumbral and umbral boundaries (marked in red). Then we used Stokes V maps to further designate areas as quiet star and plage regions. We define our quiet star regions such that the spatially averaged $\frac{V}{I_{cont}}$ in that region does not exceed 2 %, and the plage regions such that the average $\frac{V}{I_{cont}}$ is always less than 10 %. In order to calculate the effect of spots on the RV, we chose the Fe 630.25 nm line, similar to Cegla et al. (2013). Since the RV caused by exoplanets can be less than 100m/s, we chose a higher spectral resolution and focussed on just one line. We computed 2000 points for a wavelength interval of 0.1 nm as opposed to the first study where we used 300 points for a wavelength interval of 0.4 nm.

## 3.3 Continuum Contrasts

In Figure 3.1 we have presented continuum intensity images of the three simulated starspots at 630 nm and 2231 nm at the disk centre. The Planck function changes more sharply with temperature at lower wavelengths and the contrasts are therefore higher at 630 nm. The umbral (penumbral) relative intensities at 630nm are 0.27 (0.56), 0.37 (0.66) and 0.61 (0.85) for the G2V, K0V and M0V spots respectively. The relative intensities at 2231 nm are 0.71 (0.85), 0.76 (0.89) and 0.87 (0.97). Naturally, the relative intensities at 630 nm are lower than the bolometric relative intensities computed in Panja et al. (2020), while the reverse is true for the intensities at 2231 nm. It is interesting that at 2231 nm, the umbral dots become more visible and further add to the decrease in contrast. Note that the penumbra of the M0V spot becomes almost indistinguishable from the quiet star in the infrared. This means, if we assume that in the M0V spot, the 1:4 umbra-penumbra ratio typically observed on the Sun holds, the spot contrast (0.05) in the infrared becomes almost negligible. Also, in the M0V starspot, the spines (dark excursions into the penumbra), although appearing roughly as dark as the umbra at 630nm, are considerably brighter

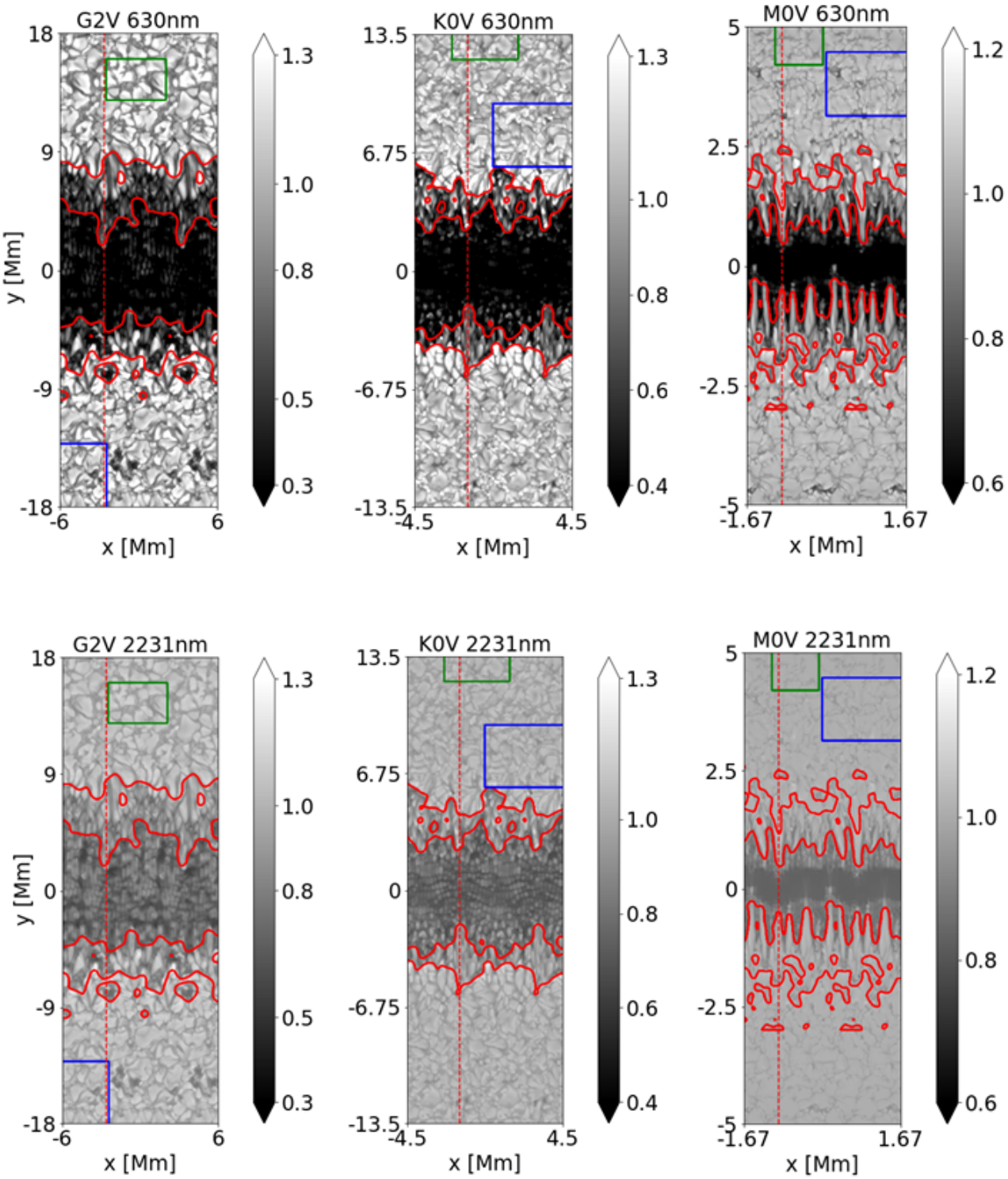


Figure 3.1: Continumm intensity of the G2V, K0V and M0V starspot non-grey simulations at 630nm (top panel) and at 2231 nm (bottom panel).

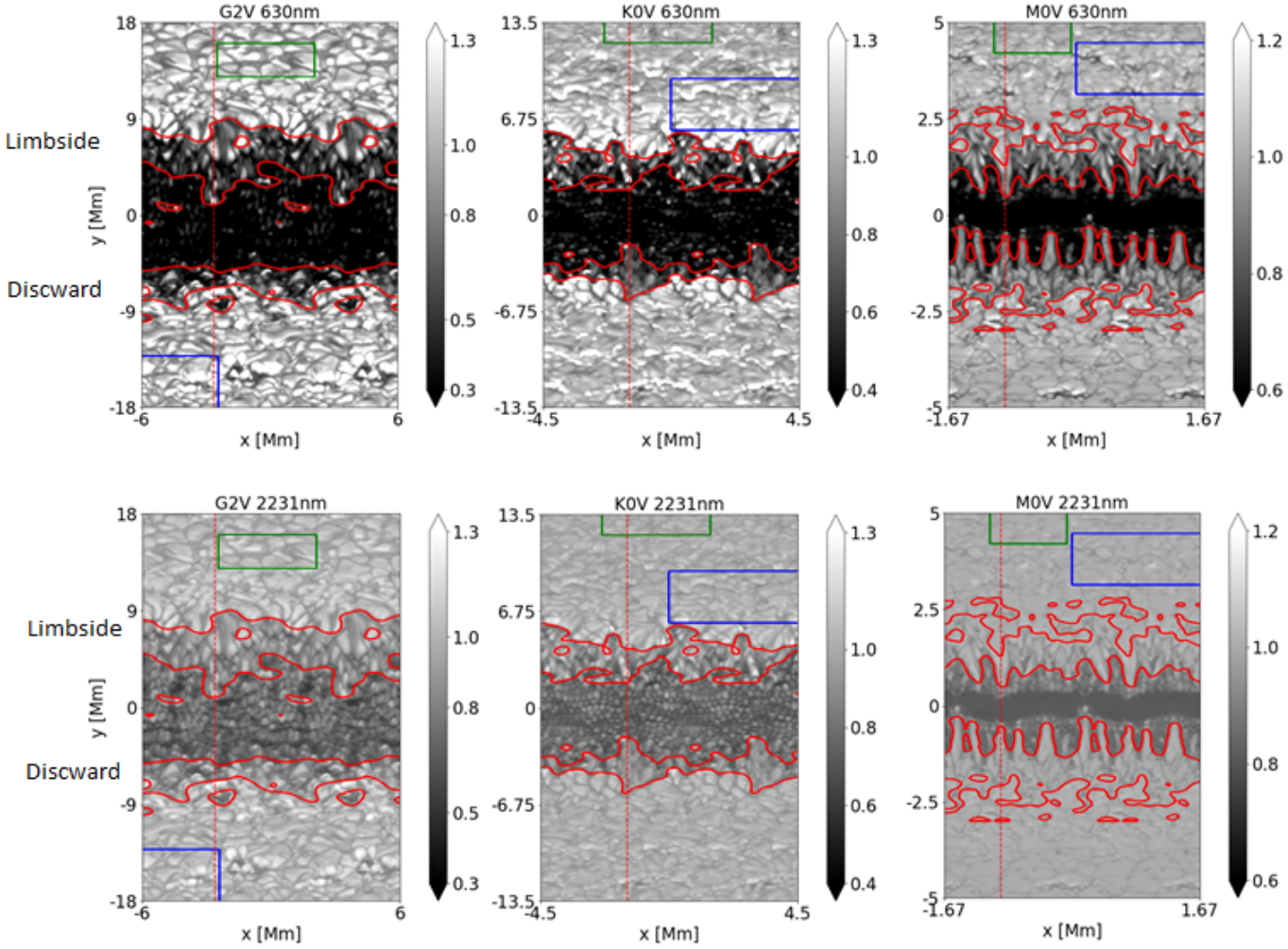


Figure 3.2: Continumm intensity of the G2V, K0V and M0V starspot non-grey simulations at 630nm (top panel) and at 2231 nm (bottom panel) at a viewing angle of 60 degrees. The boxes have been tilted such that the penumbrae in the upper halves of the images become the limb-side penumbrae.

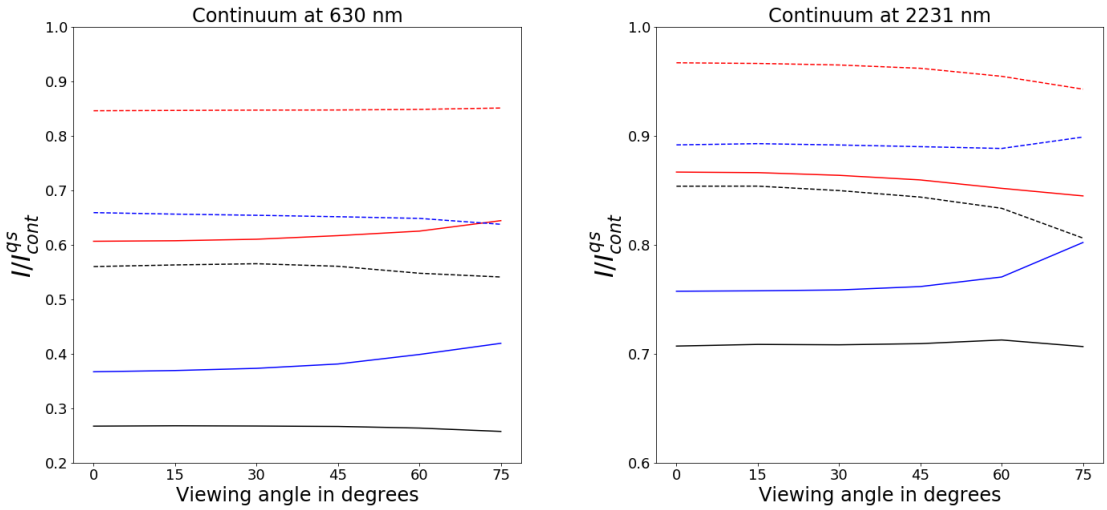


Figure 3.3: The intensity of spots as a fraction of the local quiet star intensity with changing viewing angle, at two different wavelength points on the continuum. Black - G2V, Blue - K0V, Red - M0V. Solid - Umbra, Dashed - Penumbra.

in the infrared.

In Figure 3.2 we have plotted the continuum contrasts at a viewing angle of $\mu = 0.5$. The change in viewing angle is equivalent to a spot moving across the stellar disk. We have tilted our simulation boxes such that the penumbrae in the lower halves of the images in Fig. 3.1 become discward penumbrae in Fig. 3.2 while the penumbrae in the upper halves of the images become limbside penumbrae. Choosing this geometry has the advantage that the horizontal Evershed flow in the penumbra now has a LOS component. There are several key differences between Figure 3.1 and Figure 3.2 that arise purely because of geometrical reasons. In the quiet star region, at a viewing angle of 60 degrees, the rays traverse along a longer, more slanted path and probe the inner hot walls of pores. This means pores which appear dark at the disk centre, now resemble bright faculae. This is a well studied area in stellar surface simulations and has been discussed in detail by Beeck et al. (2015a), Steiner (2005). The slanted ray path also causes the disk side penumbra to appear shorter while we see more of the limb side penumbra. The reason is purely geometrical and is principally similar to the hot wall effect. We can think of the penumbra as the walls of the spot (a much gentler slope than a pore wall) and naturally the slanted ray path blocks a part of the disk-side penumbra out of view while we see deeper into the limb-side penumbra. It is this phenomenon that led Alexander Wilson in 1769 to conclude that sunspots are saucer shaped depressions on the solar surface. See Wilson and Cannon (1968) for an observational study of the Wilson effect on a sunspot traversing the solar disk. However as the Wilson depression of the spots vary with spectral type - maximum for the G2V spot and minimum for the M0V spot (see Panja et al. (2020)), this effect is the most pronounced for the G2V spot while for the M0V spot which has a shallow umbra, the disk-side penumbra and the limb-side penumbra are of comparable sizes.

At higher viewing angles, the longer ray paths also mean that they probe higher layers

of the atmosphere. This is what causes the limbs of a star to appear darker than the disk centre. In both the figures, we have normalised the images by the local quiet star intensity, which is why the effect of limb darkening is not visible. This allows us to study the change in spot contrast with respect to the local quiet star intensity at various viewing angles. At higher viewing angles, since we are seeing higher layers of the atmosphere for both the spot and the quiet star, the local spot contrast would depend on how fast the spot temperature decreases with decreasing optical depth, compared to the quiet star. We have plotted this change in Figure 3.3 and it turns out that starspot contrast with respect to the local quiet star intensity is more or less invariant with viewing angle, especially in the visible wavelengths. Sunspot umbral contrasts are known to show no appreciable centre-to-limb variation (Maltby et al. 1986). It is reassuring that our simulations reproduce this observational effect for the Sun. They also show that this holds true for spots on other stars. Limb darkening is the only effect one has to worry about when modelling starspot contrasts at various positions on the disk. Note that in the infrared the contrasts of the K0V and the M0V spots do show a mild variation (less than 10 %) near the limb.

## 3.4 Spectral lines at Disk centre

### 3.4.1 Fe I 630.15 and 630.25 nm

In Figure 3.4 we have plotted the Stokes I and V profiles of the Fe I pair of lines along the red dashed lines of Fig: 3.1, mimicking spectro-polarimetric data taken through a slit. This allows us to visualize how the line profiles at individual spatial points vary as we move from the quiet star to the penumbra and then to the umbra. We notice several things immediately in the Stokes I plots -

1) The 630.15 nm line is stronger than the 630.25 nm line for all the spectral types. Both the lines become weaker as we move from the G2V star to the M0V star.

2)The more magnetically sensitive 630.25 nm line shows more splitting. The splitting is maximum in the M0V umbra. The 630.25 nm is split into three wherever there are strong horizontal fields (penumbra and umbral edge).

3) The bright horizontal stripes outside the spots correspond to granules and darker (yellow in the adopted color scale) stripes correspond to the intergranular lanes where the lines show a redshift.

The Stokes V profiles appear wherever there are vertical magnetic fields. The Stokes V (normalized by the local Stokes I continuum) is the strongest in the G2V umbra ($\approx 0.3$ times the Stokes I continuum for the 630.25 line) and it is much weaker in the M0V umbra ($\approx 0.1$ of Stokes I continuum for the 630.25 line). Notice that the Stokes V lobes show both blue and redshifts in the G2V spot whereas the Stokes V lobes in the M0V spot do not show any discernible shifts, signifying the presence of convective activity in the G2V spot, but its absence in the M0V umbra.

In Figure 3.5 we have plotted the spatially averaged Stokes I (left panel) and the Stokes V (right panel) profiles of the Fe I line pair. We divided our box into four distinct regions - the umbra (red), the penumbra (red dashed), the quiet star (green), and plage regions (blue). All the Stokes I profiles have been normalised to the continuum of the non-magnetic quiet star region. The left column shows the Stokes I of these four distinct

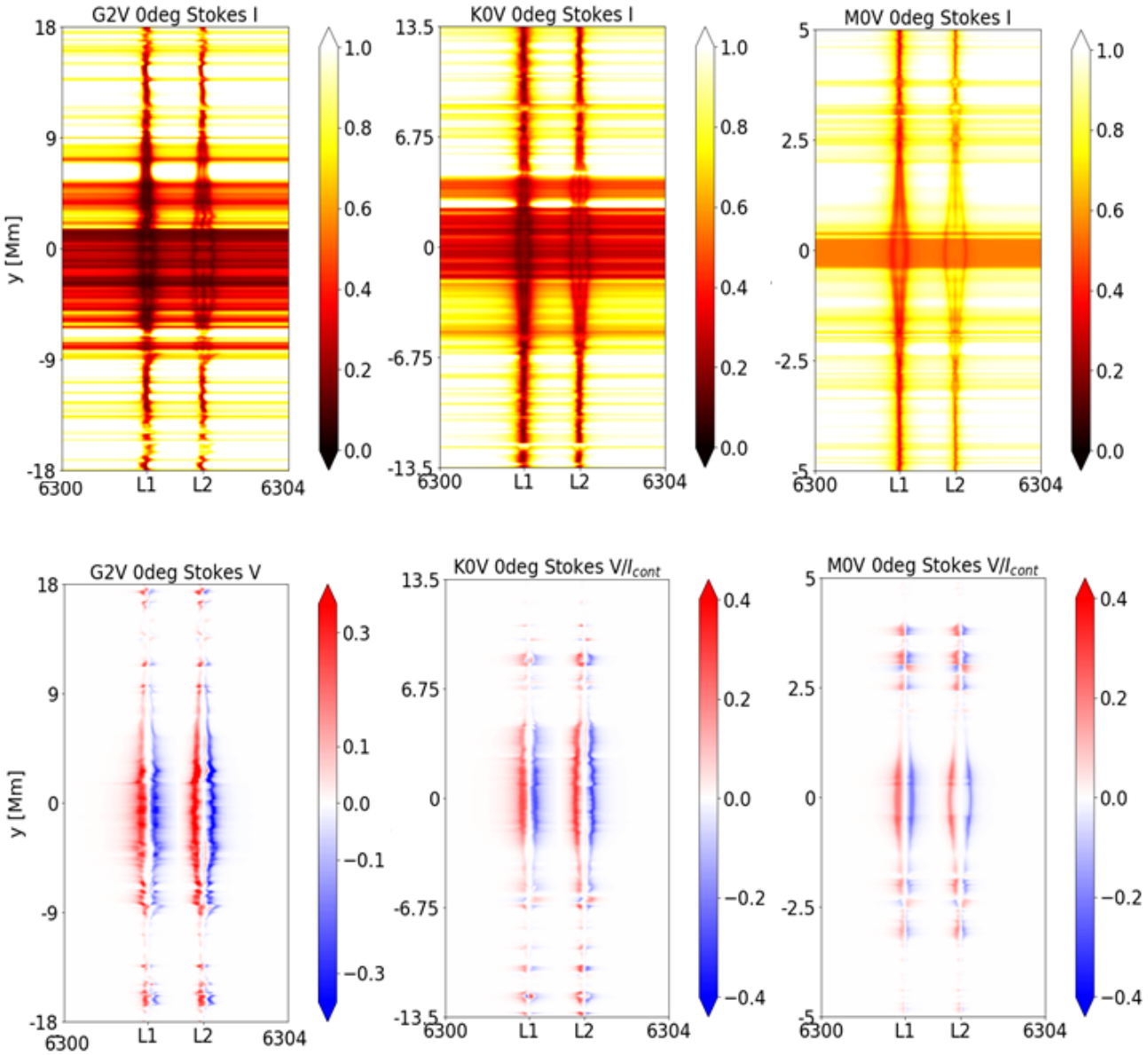


Figure 3.4: Stokes I (top) and Stokes V (bottom) profiles of the Fe I pair of lines along a slice (red dashed lines in Fig 3.1) cut through each of the simulations, resembling spectro-polarimetric data obtained with a split spectrograph. The points marked L1 and L2 correspond to the centers of the 630.15 and 630.25 lines respectively.

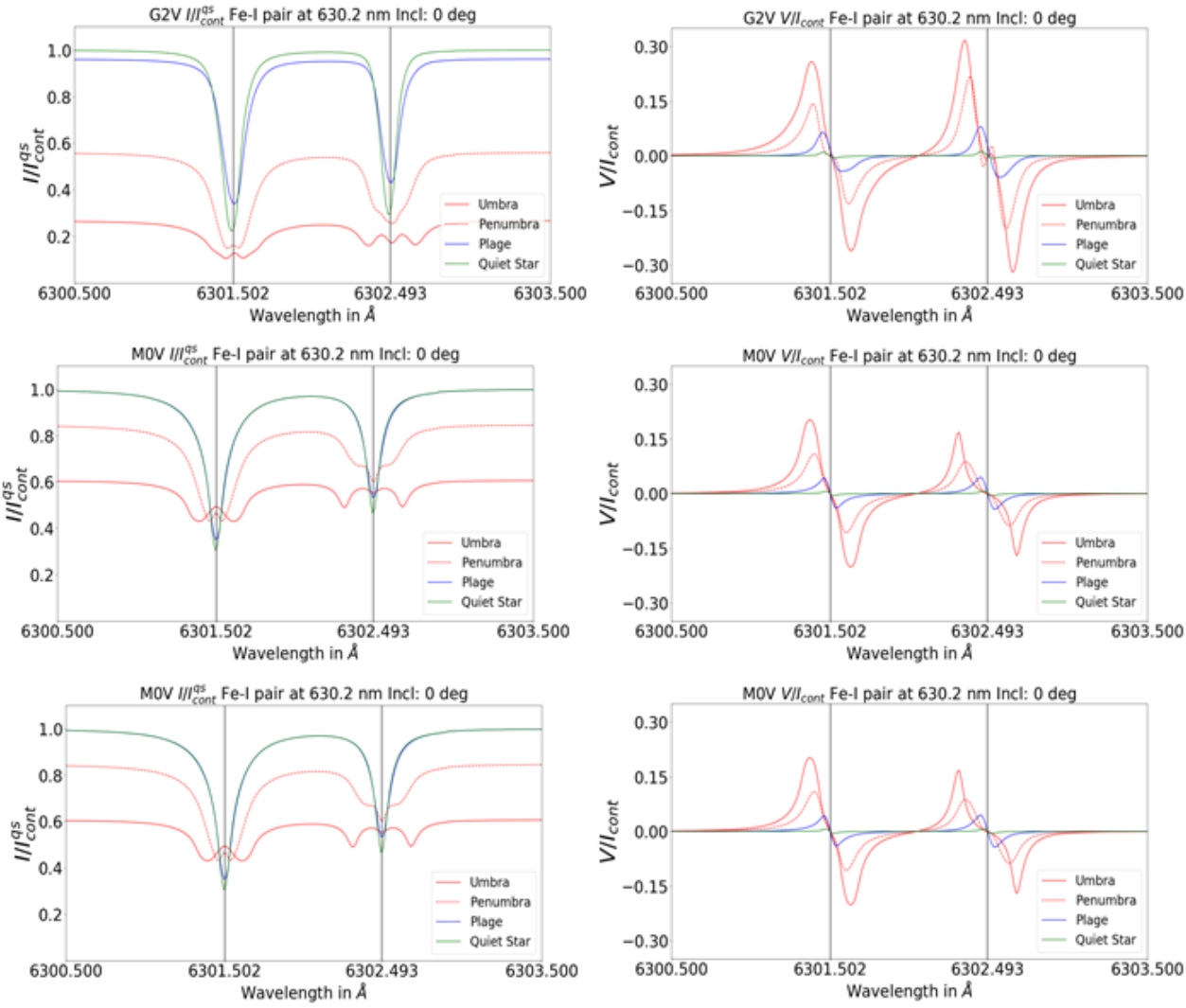


Figure 3.5: Left Panel: Stokes I profiles, normalized by the continuum intensity at 630 nm in quiet star regions, for the umbra (red), penumbra (red-dashed), quiet star (green) and plage regions (blue). Right Panel: Stokes V profiles, normalized by the local continuum intensity at 630 nm.

regions. The quiet star regions show the expected convective blueshift, best visible for the G2V star. Similar to the slit spectra plot, the 630.15 nm line is stronger on average in all the three quiet star regions. The continuum drops for the umbral and penumbral profiles and owing to the splitting of the lines and their lower temperatures the lines are shallower than their quiet star counterparts. A flatter temperature stratification in the umbrae could also play a role.

The penumbral regions have mostly horizontal field and they are dominated by the $\pi$ component. The umbral Stokes I profiles have both the $\sigma$ and $\pi$ components. The 630.25 nm line in the G2V umbral case has all the three components and they are equally prominent, while the M0V umbral Stokes I for this line has only the $\sigma$ components, indicating that umbral fields are the most vertical in the M0V umbra, while the G2V umbra also has some horizontal fields.

The right panel shows the Stokes V profiles of the spots normalised by the local Stokes I continuum. It is interesting to note that the amplitude of Stokes V (both the 630.15 and 630.25 nm) drops from the G2V to the M0V star also seen in Fig: 3.4). This is because the Stokes V amplitude is not only determined by the magnetic field strength but also by the line strength. The lines become weaker as we move from the G2V star to the M0V star and this might contribute to the difference in the degree of polarisation between the spectral types. Other factors like formation heights of the lines might also play a role. Within each spectral type, the Stokes V profiles show their expected behaviour - the umbra has the strongest Stokes V while the quiet star has the weakest.

### 3.4.2 Ti - I 2231.06 nm

Figure 3.6 shows "slit spectra" (similar to Fig: 3.4) for the Ti I line. The first thing we notice is that the Zeeman splitting, owing to the larger wavelength of the line, is much more severe than the Fe 630.25 line. The splitting is considerably larger in the M0V spot than the G2V spot. The amount of splitting, the line undergoes, fluctuates in the G2V and the K0V umbrae, whereas in the M0V umbrae the splitting is maximum at the centre of the umbra and decreases at the umbral edge. This tells us that the M0V umbral magnetic field has a smooth gradient in the y-direction and the G2V and K0V umbral field strengths have random variations . Another interesting feature of the Ti line is that in the G2V star it is very weak in the quiet star and forms primarily in the spot. The Ti line is extremely sensitive to temperature. Owing to the low ionisation potential, the Ti I line cannot form at temperatures higher than 5000 K, whereas in very cold regions Ti combines with oxygen to form TiO molecules (Rüedi et al. 1998). This strong temperature sensitivity makes the Ti I line a very useful tool to study cool spots on relatively hotter (G and above) stars. However this is not the case in the cooler M0V star, where the line is in fact stronger in the quiet star. This is because the M0V spot is cold enough for TiO molecules to start forming thereby weakening the Ti I line inside the spot.

In Figure 3.7 we have plotted the spatially averaged Stokes I (left panel) and the Stokes V (right panel) profiles of the Ti I line. Like in the Fe I line, the Ti I line in the M0V umbra shows only the $\sigma$ components whereas the G2V umbra exhibits also the $\pi$ component. Note that the two $\sigma$ lobes of the M0V umbra are highly asymmetric - the wing of the left lobe is highly blueshifted while the wing of the right lobe is redshifted. This indicates a strong vertical gradient in the the magnetic field: the Zeeman splitting is much stronger

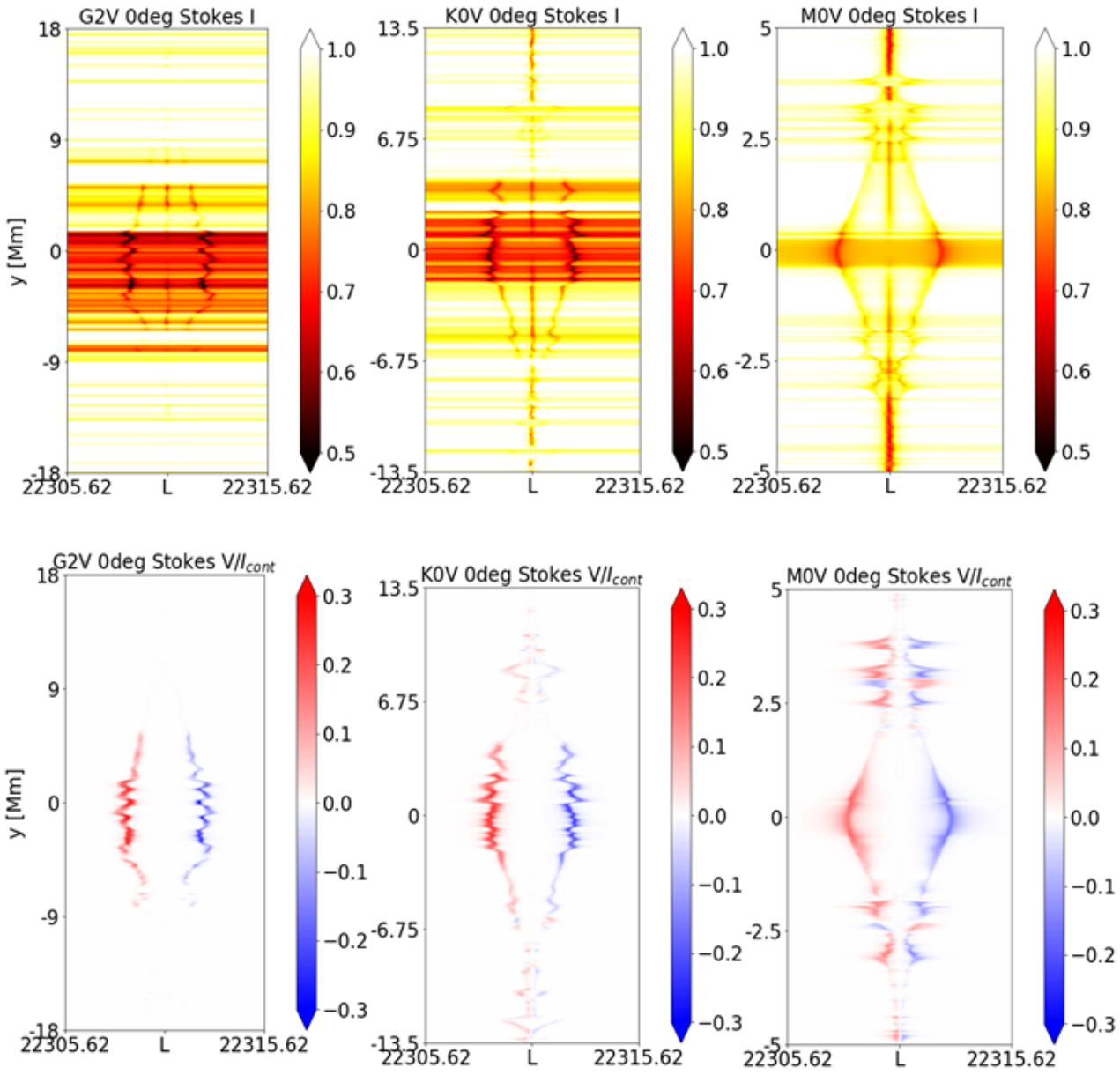


Figure 3.6: Same as Fig: 3.4, but for the Ti I line. The point L marks the line centre.

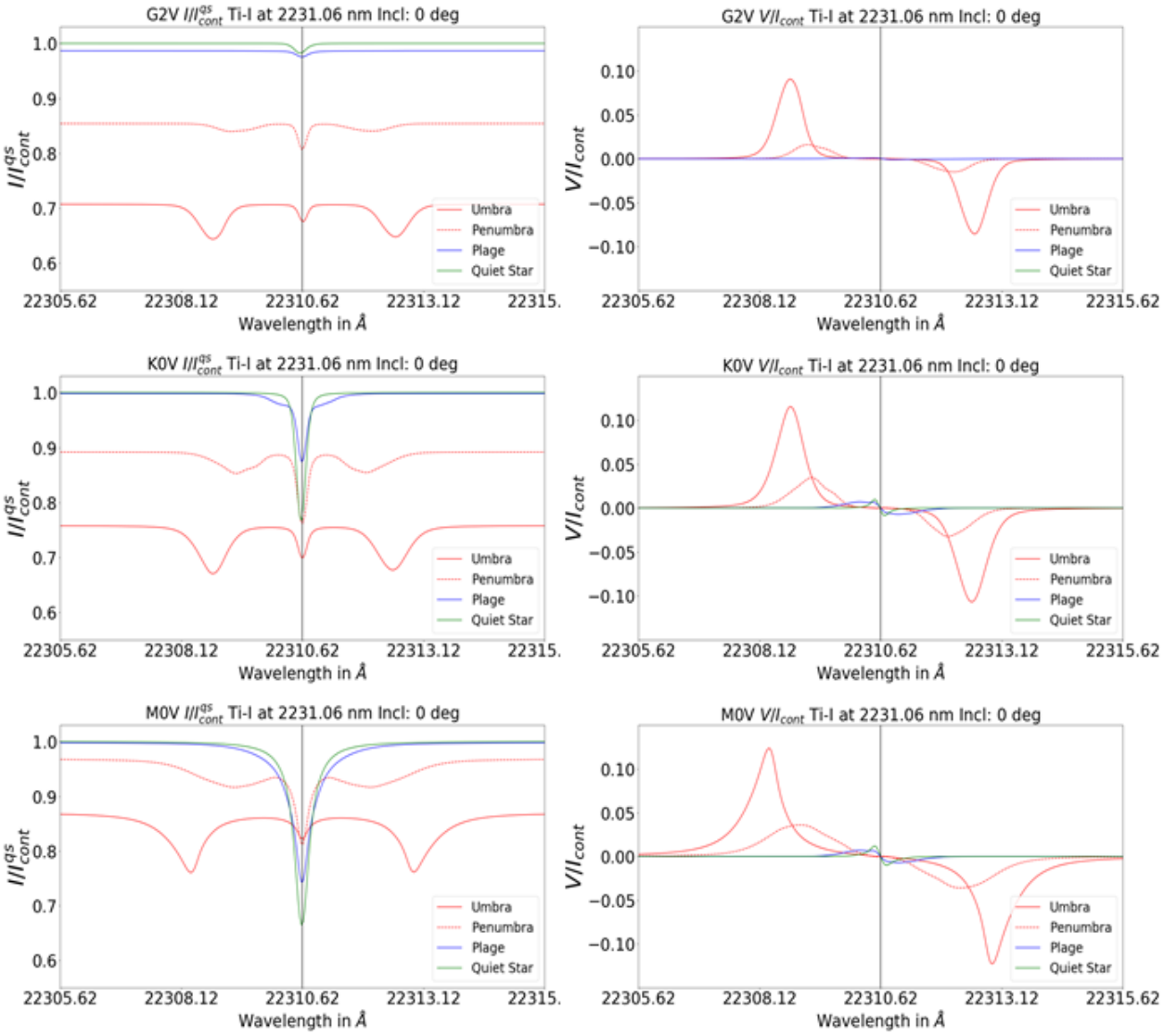


Figure 3.7: Same as Figure 3.5, but for the Ti I line.

closer to the stellar surface than higher up.

The normalised Stokes V signal shows a monotonic increase from the G2V umbra to the M0V umbra, unlike what we saw for the Fe-I line pair. This is probably because the line is not saturated in the M star umbra.

## 3.5 Centre-to-Limb Variation

In Figure 3.8 we have plotted the spatially averaged Stokes I profiles (Fe 630.25 nm line ) of the penumbra and umbra of G2V and M0V spots at different viewing angles. The profiles have been normalised with respect to the continuum of the quiet star at disk centre so the limb darkening effect is accounted for. Here we have considered the discward and the limbside penumbra separately. As we discussed in Section 3.3, a significant portion of the discward penumbra is blocked out of view while we see deeper into the limbside penumbra and therefore they ought to be analysed separately.

For both the discward and limbside penumbra of the G2V spot, the relative line strength decreases with an increase in viewing angle. The penumbra has strong horizontal fields, and at disk centre both the penumbra show $\pi$ components. As we increase the viewing angles, the mostly out-of-view discward penumbra shows a decrease in the $\pi$ component and at 75 $^\circ$ the 630.25 nm is split into two weak $\sigma$ components.

In the colder M starspot, the penumbral line profiles show minimal change with viewing angle. We do not see a discernible increase in the $\sigma$ components in the Stokes I profiles. The M0V umbral profile (630.25 nm), however, does show a significant increase of the $\pi$ component with increasing viewing angle, in accordance with what one would expect for a change in LOS.

We have plotted the CLV of the Stokes I profiles of the Ti - I line in Figure 3.9. The discward penumbra which is mostly blocked out of view assumes a complicated profile at higher viewing angles. In the G2V umbra we see an increase in the $\pi$ component relative to the $\sigma$ components and this can be easily explained by change in LOS. However in the limbside penumbra there is an apparent increase in the both $\pi$ and $\sigma$ components with viewing angle. A possible explanation is this - as we approach the limb, the rays emerge from the upper cooler layers of the atmosphere and the Ti -I line in the penumbra actually becomes stronger. It could also be that at very large angles, 75 deg, the rays also pass through the very cold umbra, making the line stronger. Only a careful comparison of spatially resolved line profiles with the structure of the magnetic field (and other physical quantities) in the MHD simulation will provide reliable guidance, which we will do in the future.

In the M0V umbra we see the expected increase of the $\pi$ component of the magnetic field.

## 3.6 Effect of a spot on the host star's Radial Velocity

As we have discussed before, the simplest way a spot can affect the radial velocity of a star is by reducing the flux of photons coming from the hemisphere on which it is located. This will break the balance between the rotationally induced redshift and blueshift integrated over the stellar surface. However, starspots can also affect the RV in another less studied,

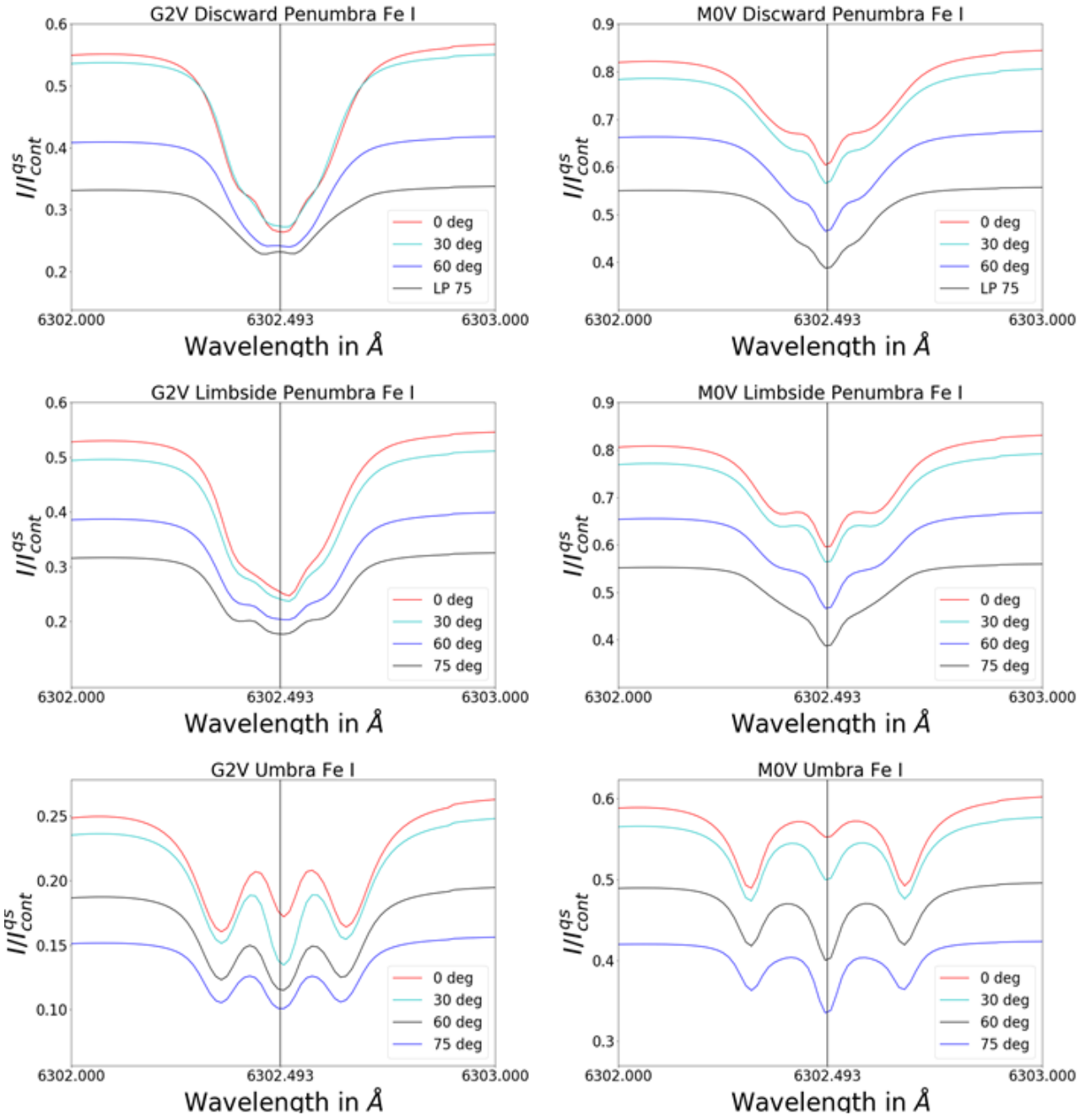


Figure 3.8: CLV of the Fe I 630.25 nm Stokes I profiles. Left Panel: G2V Stokes I profiles, normalized by the quiet star (disk-centre) continuum intensity at 630nm, of the discward penumbra (top), limbside penumbra (middle) and the umbra (bottom), at different viewing angles - 0 (red), 30 (green), 60 (blue), and 75 (black) degrees. Right Panel: Same as the left panel but for the M0V case.

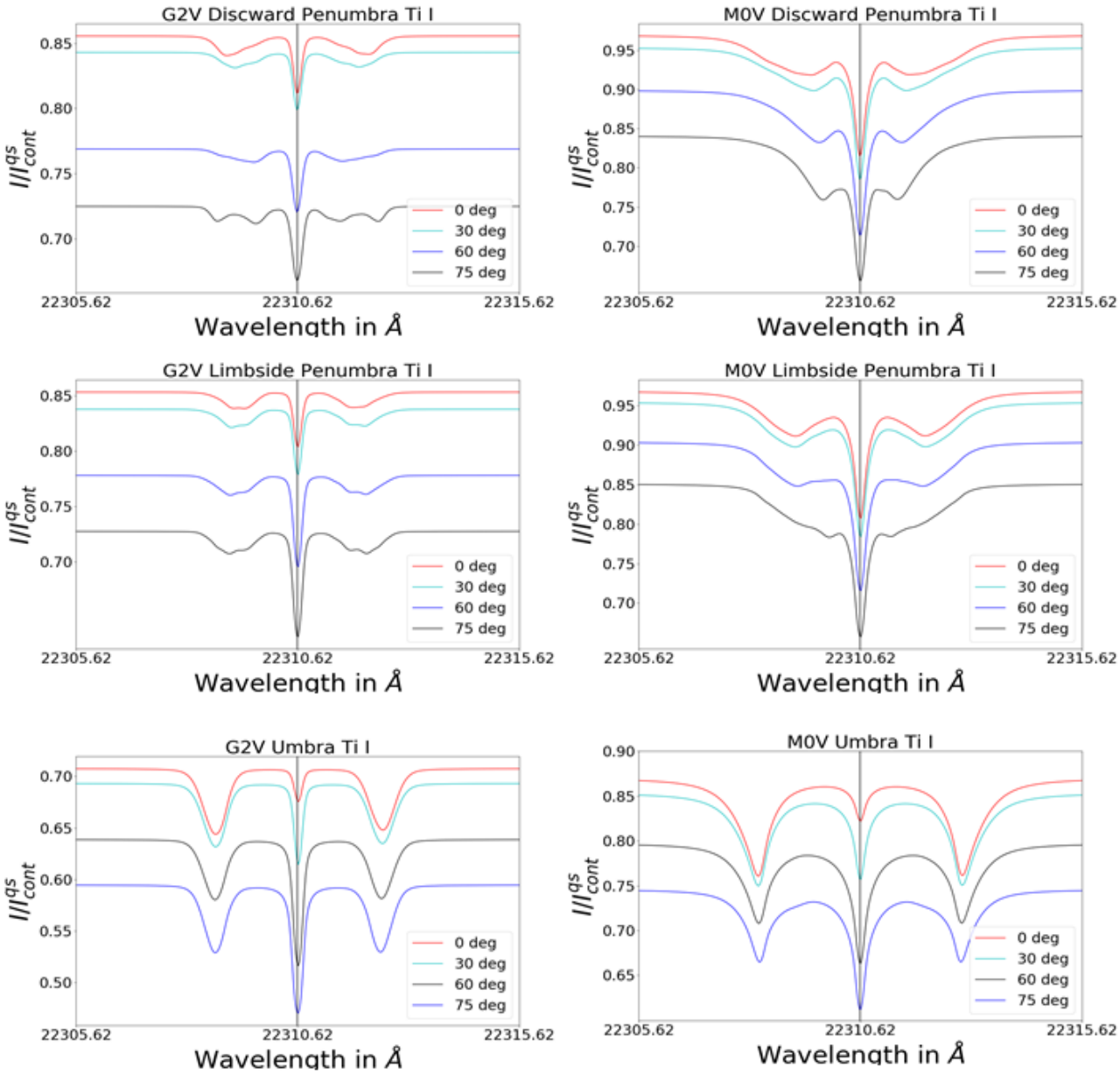


Figure 3.9: Same as 3.8, but for the Ti - I line. Left panel - G2V, Right panel - M0V.

but crucial way. Spots are inhibitors of convection and may harbour flows of their own. Thus, their presence will affect a star's net convective blueshift. Desort et al. (2007) showed that when the *v sin i* of a star is smaller than the resolution of the spectrograph even moderately sized spots (1 %) do not change the shape the bisector but merely shifts the bisector and therefore may cause RV changes similar to that of a planet. Obviously for stars with significant rotational broadening of their lines, a higher spectrograph resolution means a smaller portion of the disk is sampled. In this study, we have not considered the effects of rotation, as we want to estimate the RV changes caused by spot for reasons other than a loss of radiative flux.

To compute the effect of spots on the stellar radial velocity, we must first create disk-integrated stellar line profiles and estimate their net convective blueshift. The next step, is to add spot line profiles to the disk-intergated spectra. We did this by placing spots at three different positions on the disk - at the disk centre, and at viewing angles of 30 degrees and 60 degrees. Figure 3.10 illustrates how this has been done. We divide the stellar surface into concentric rings. It is assumed that all points within an area of a particular color have the same line profile. For example, all points within the central ring (green) are assumed to be at disk-centre. Then, we sum up the different profiles weighted by the fraction of the stellar disk they cover. Finally, we place spots of different sizes at different disk locations. This is done by simply replacing some fraction of the quiet star spectra with an equal amount of spot spectra. We calculated the spot spectra by combining the umbral and penumbral profiles at a 1:4 ratio.

### 3.6.1 G2V

In the leftmost panel of Figure 3.11 we have plotted the profiles of the Fe 630.25 nm line averaged over the quiet G2V star, at 5 different viewing angles. All the lines have been normalized by the quiet star continuum intensity at disk-centre and the limb darkening is clearly visible. The middle panel shows the bisectors of the profiles plotted on the left. The right panel shows the bisector of the disk-integrated quiet star line profile. The bisector at the disk centre has a C shape. Our synthetically computed line bisector shapes at various viewing angles, although slightly blueshifted, match well with observations (see Fig:8 of Löhner-Böttcher et al. (2018b)). The blueshift is maximum at the disk centre, as the upflow area coverage is significantly more than the downflow area coverage. As we move away from the stellar disk centre, due to geometrical effects we start seeing into the intergranular lanes, which are regions of strong downflows and therefore the blueshift decreases with viewing angle. In the rightmost panel we have computed the bisector of the disk-integrated quiet star profile. The net convective blueshift of the G2V star comes out to 167 m/s at the line core.

Figure 3.12 shows bisectors for the disk-integrated G2V star with spots of different filling factors (0, 0.1 %, 1 % and 5 % ), placed at different viewing angles (0, 30 and 60 degrees). It is clear that spots placed at the disk centre have the maximum effect on RV, if we neglect stellar rotation. The spot which covers only 0.1 % of the disk-area naturally has the smallest effect on the disk-integrated profile. At all disk positions it affects the RV by less than 1 m/s. The 1 % spot shifts the RV by more than 3 m/s at disk centre. As expected, the spot with 5 % disk coverage has the maximum effect on RV. At the disk centre it shifts the RV towards the red by 16 m/s. When this spot is placed at 60

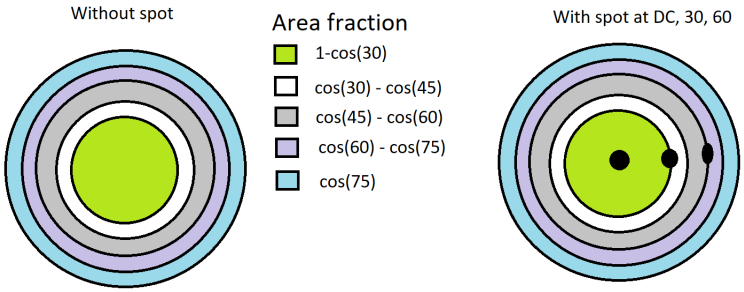


Figure 3.10: A cartoon explaining the disk-integration process. All points within an area of a particular colour are assumed to have the same line profile. We then sum up the line profiles weighted by their fractional area coverage. To calculate the effect of spots, we replace some of the disk-integrated quiet star by average spot spectra.

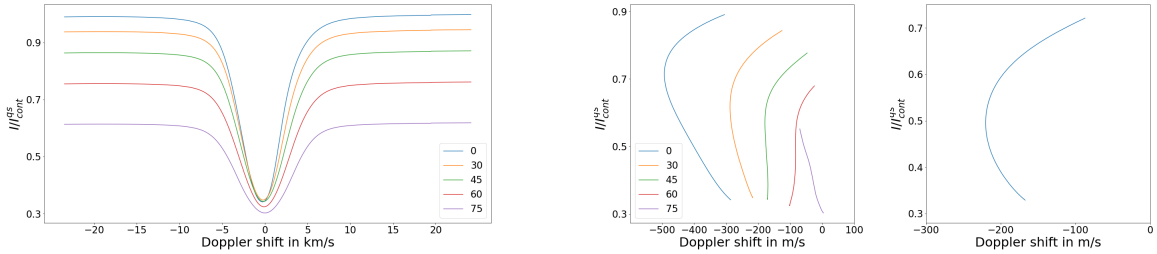


Figure 3.11: Left: High resolution (2000 points) synthetic Fe 630.25 nm spectral line, calculated for the G2V quiet star at different viewing angles. Middle: Line bisectors of the quiet star line profiles. Right: Line bisector of the disk-integrated quiet star profile

degrees it induces a tiny blueshift of about 0.5 m/s. It is interesting that a spot adds to the blueshift; it contradicts the simplistic idea that spots merely block convection and cause a loss in radiative flux (both of which would only reduce the convective blueshift). This emphasizes the need for properly accounting for flows within spots, as the net effect of spots on RV does not seem to simply linearly depend on spot size and viewing angle.

### 3.6.2 M0V

In Figure 3.13 we have plotted the line profiles of the M0V quiet star at different viewing angles (left), their bisectors (middle), and the bisector of the disk-integrated line profile (right). The convective blueshift is much smaller than the G2V star. The bisector shapes are also significantly different. The bisectors are flatter near the disk-centre, but become more S shaped near the limb. This could be because of many possible reasons.

Like the G2V star, the spots have the most impact when they are at the disk-centre. The spot with 1 % coverage affects the RV by only 0.04 m/s whereas the 5 % spot redshifts the RV by almost 3 m/s at the disk centre. Unlike the G2V spot, at 60 degrees the 5 % M0V spot does not add to the convective blueshift.

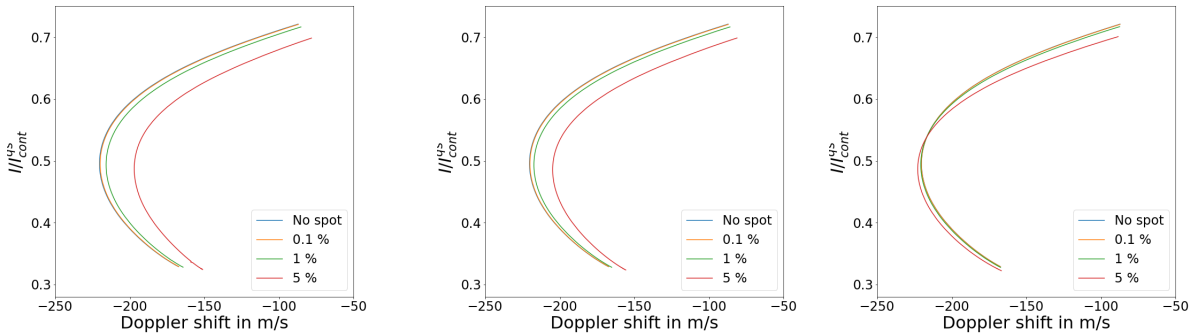


Figure 3.12: Left: Line bisector of the disk-integrated G2V star with a spot placed at the disk centre. We have used three spot filling factors- 0.1%, 1% and 5%. Middle: Same as left image, but with a spot placed at 30 degrees. Right: Same as left and middle images, but with a spot placed at 60 degrees.

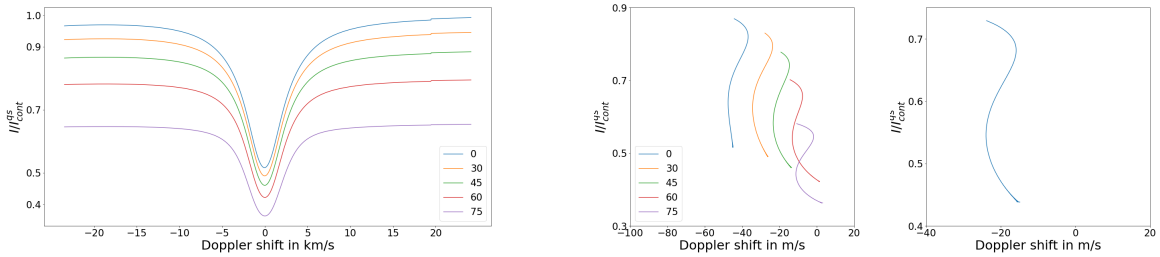


Figure 3.13: High resolution (2000 points) synthetic Fe 630.25 nm spectral line, calculated for the M0V quiet star at different viewing angles. Middle: Line bisectors of the quiet star line profiles Right:Line bisector of the disk-integrated quiet star profile

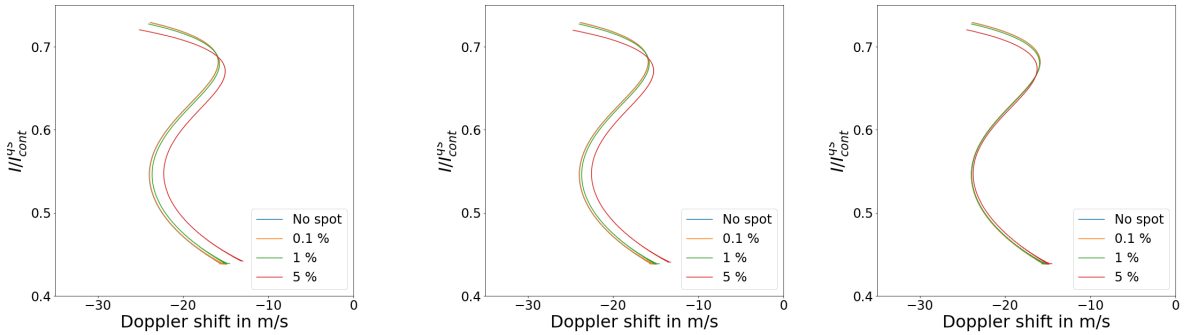


Figure 3.14: Left: Line bisector of the disk-integrated M0V star with a spot placed at the disk centre. We have used three spot filling factors- 0.1%, 1% and 5%. Middle: Same as left image, but with a spot placed at 30 degrees. Right: Same as left and middle images, but with a spot placed at 60 degrees.

## 3.7 Summary and Conclusions

In this chapter we have calculated continuum contrasts of G2V, K0V and M0V starspots at the visible (630 nm) and the infrared (22310 nm). We concluded the following from the continuum contrast calculations at various viewing angles: -

1) As expected, starspot contrasts are weak in the infrared because of the weak dependence of the Planck function on temperature at larger wavelengths. This is especially problematic for the M0V spot, whose penumbra is almost indistinguishable from its quiet star. However for exoplanet hunters observing in the infrared this can be seen as good news.

2) In the G2V starspot which has a large Wilson depression, geometrical effects become important as the spot traverses the stellar disk. The disk-side is partially blocked while we see deeper into the limb-side penumbra. This is not the case for the M0V spot.

3) Continuum contrasts of starspots, regardless of wavelength, do not change much with viewing angle.

From the synthesized line profiles, our findings can be summarised as follows -

1) Local thermodynamic properties affects line strengths which in turn could affect the degree of polarization.

2) The Ti-I line can prove to extremely useful to study cool spots on G and hotter stars, as its high temperature sensitivity ensures that it only picks up signals from cool spots.

We further calculated disk integrated line profiles and estimated the effects spots can have on a star's RV. We found that spots can significantly affect the convective blueshift not just because they inhibit convection but also because they themselves carry flows. An interesting case is the G2V spot adding to the blueshift at a large viewing angle. Even on the M0V star, where convective velocities are low, we computed spot induced RV shifts of about 3 m/s, for a filling factor of 5 %.

To put this in context, an Earth-like planet revolving around a Sun-like star will induce RV variations of only $\approx$ 0.1 m/s (see http://exoplanets.astro.yale.edu/workshop/EPRV/Bibliography_files/Radial_Velocity.pdf for a table of RV signals induced by different kinds of planets). Therefore, we emphasize the need to properly constrain motions within starspots - both umbral and penumbral. In this preliminary study, we have considered only one snapshot of a starspot for each of the stellar types. Starspots will have oscillations, (as are observed in sunspots (Bogdan and Judge 2006)) and a study involving a number of snapshots is required to fully constrain their effects on the RV. We are in the process of generating spectra over a period long enough to cover several oscillations. Nonetheless, our preliminary results show the importance of this effort.

# 4 Sunspot simulations: penumbra formation and the fluting instability

The contents of this chapter were authored by Mayukh Panja, Robert Cameron, and SamiK. Solanki and published in the Februrary 2021 edition of The Astrophysical Journal (Panja et al 2021 ApJ 907 102, DOI: https://doi.org/10.3847/1538-4357/abccbf)

## Abstract

The fluting instability has been suggested as the driver of the subsurface structure of sunspot flux tubes. We conducted a series of numerical experiments where we used flux tubes with different initial curvatures to study the effect of the fluting instability on the subsurface structure of spots. We used the MURaM code, which has previously been used to simulate complete sunspots, to first compute four sunspots in the slab geometry and then two complete circular spots of opposite polarities. We find that the curvature of a flux tube indeed determines the degree of fluting the flux tube will undergo - the more curved a flux tube is, the more fluted it becomes. In addition,sunspots with strong curvature have strong horizontal fields at the surface and therefore readily form penumbral filaments. The fluted sunspots eventually break up from below, with lightbridges appearing at the surface several hours after fluting commences.

## 4.1 Introduction

It is not known what the magnetic field associated with sunspots looks like underneath the solar surface. Cowling (1946) proposed that a sunspot extends below the surface as a magnetic flux tube - field lines bound tightly together in a single monolithic column resisting deformation against pressure from the surrounding gas. However, the sharp vertical gradient in the ambient gas pressure at the surface necessitates that the magnetic field lines fan out rapidly. This would make a flux tube highly concave near the surface, and therefore susceptible to the fluting instability. This prompted Parker (1979) to suggest an alternative configuration in which the field underneath the surface may be structured - a sunspot, in this view, is a cluster of numerous small flux tubes that are held together by a converging flow below a certain depth. However, Meyer et al. (1977) had used a vacuum model of a flux tube to study the stability of spots against the fluting instability, and concluded that spots should not break up into smaller flux tubes up to a depth of 5

Mm. Spruit (1981) built on the work of Meyer et al. (1977) and constructed a cluster model of a sunspot which is similar to a tethered balloon model (see Figure 1 of Spruit (1981)) - the tube remains coherent upto a certain depth, beyond which it is fragmented into small individual flux tubes that are tied together at the base of the convection zone. It differed from Parker (1979), in that the tying of the flux tube to the base of the convection zone removed the necessity of a converging flow to explain the stability of sunspots. For a discussion on the merits and demerits of both the monolithic and cluster models, see Chapter 1 of Thomas and Weiss (1992).

The fact that penumbral filaments often invade a spot's umbra and fragment it ( Louis et al. (2012b), Benko et al. (2018b)), suggest that the fluting instability might play a role in determining the subsurface structure of spots and therefore, by extension, their appearance on the surface. However, the probing of sunspot subsurface structure using helioseismic techniques has not been able to distinguish between the cluster and monolithic models (Moradi et al. 2010). Existing MHD simulations of complete sunspots, (Rempel et al. 2009a, Rempel 2011c,a) using the radiative-MHD code MURaM (Vögler et al. 2005, Rempel et al. 2009b), correspond to the monolithic model. Rempel (2011c) specifically addressed the question of whether a sunspot is monolithic or cluster-like underneath the surface and concluded that sunspots are closer to the monolithic model, but can become highly fragmented in its decay stage. However these models have field lines that are too vertical near the spot periphery to form penumbral filaments naturally. This is overcome by increasing the horizontal field strength at the top boundary by a factor of two compared to a potential field configuration, and the extent of the penumbra is solely determined by the magnetic top boundary condition (Rempel 2012). Recently, Jurčák et al. (2020) presented a sunspot simulation with a decent sized penumbra without modifying the top boundary, by using a strongly compressed flux tube at the lower boundary. Their penumbra, however, is dominated by the counter-Evershed flow. Also their umbral field strength is higher than what is observed.

In this paper, we conduct numerical experiments using the MURaM code to investigate the susceptibility of flux tubes to the fluting instability by varying the initial magnetic field structure. We focus on the question - would sunspots with field lines inclined strongly enough to form penumbral filaments, result in flux tubes that become highly fluted under the surface? To this end, we constructed initial sunspot flux tube configurations where the field lines are curved near the surface, such that they form penumbral filaments without having to change the top boundary condition, and become close to vertical below a certain depth.

We describe our simulation setups and detailed descriptions of our initial conditions for our magnetic flux tubes in Section 4.2. We conducted four runs in the computationally inexpensive slab geometry, where we systematically varied the radius of curvature ($R_c$) to check if we can control the degree of fluting. Then we computed two complete circular spots of opposite polarities in a shallow computational domain. We present our results in Section 4.3 and discuss the implications of our results in Section 4.4.

## 4.2 Simulation Setup

We used the MURaM radiative MHD code for our simulations. For our four slab geometry runs, we chose simulation boxes with dimensions of 36 Mm ($x$) × 6 Mm ($y$) × 10.3 Mm ($z$) and resolutions of 48 km × 48 km × 25.8 km. We conducted a further run where we computed complete circular spots of opposite polarities. We used a relatively shallow domain with a vertical extent of 6 Mm which had a resolution of 20 km. The horizontal extents of this run were 72 Mm × 36 Mm with a resolution of 48 km in both directions. All of our boxes were periodic in the horizontal directions and the upper boundaries were kept open to plasma flows. When our hydrodynamic runs achieved thermal equilibrium, we introduced magnetic flux tubes in the simulation domains. We initialized our magnetic runs by damping all three components of the velocity field by a factor of $(1+(|B|^2/80000))$. We do this only at the timestep where our magnetic flux tubes are introduced, and thereafter we let the convective flow field develop naturally. In the following paragraphs we have described the initial structure of these flux tubes.

### 4.2.1 Slab Geometry Runs

As discussed, our initial conditions are designed to serve two purposes - 1) they should result in the formation of penumbral filaments, and 2) have a small radius of curvature ($R_c$) that induces the fluting instability. Since these are numerical experiments, we are free to choose the initial conditions to achieve these goals. For our slab geometry runs, we define the three components of the magnetic field inside the initial flux tubes, in conformity with the $\vec{\nabla} \cdot \vec{B} = 0$ constraint, as follows:

$$\begin{aligned} B_z &= f(z), \\ B_x &= -x f'(z), \\ B_y &= 0, \end{aligned} \tag{4.1}$$

where,

$$f(z) = B_{bot} \exp \frac{-z}{\sigma}. \tag{4.2}$$

At $z = 0$ (the lower boundary) we set $B_z$ to $B_{bot}$ and at $z = h_{opt}$ (optical surface) , we set $B_z$ to $B_{opt}$. $B_{opt}$ and $B_{bot}$ are parameters that we are free to choose. Using these constraints and eqn. 4.2 we can express $\sigma$ as,

$$\sigma = h_{phot} / \log(\frac{B_{bot}}{B_{opt}}). \tag{4.3}$$

Keeping $B_{\rm opt}$ at 3000 Gauss, we conducted three runs with $B_{\rm bot}$ as 10000, 20000 and 30000 Gauss. We labeled these runs as R10, R20 and R30 respectively. The top 3 panels of Figure 4.1 depict the initial $B_z$ and their corresponding $R_c$, for these runs.

In order to quantify $R_c$ we have to first calculate the curvature vector ($\vec{\kappa}$), which is given by:

$$\vec{\kappa} = \vec{b} \cdot \vec{\nabla} \vec{b} \tag{4.4}$$

where,

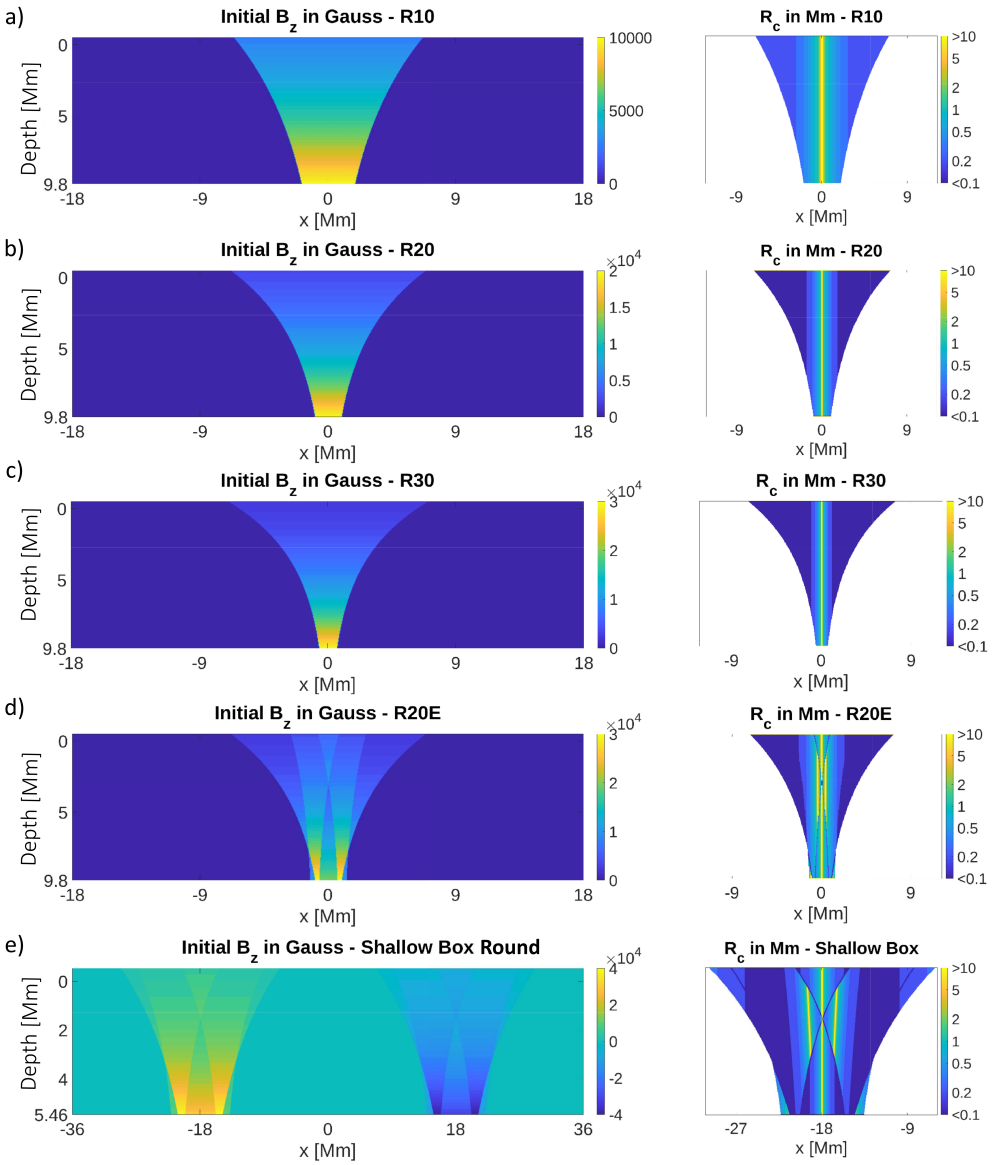


Figure 4.1: Panels a-d: Vertical slices of $B_z$ (x-z plane, here Depth = $h_{\mathrm{phot}}$ - z) used as initial conditions for the slab geometry runs, with their corresponding $R_c$ shown on the right. The initial magnetic conditions for the slab geometry runs were invariant in the y direction. Panel e: Vertical slice of $B_z$ used as initial condition for the circular spot simulation. The circular spot had an axisymmetric initial condition, with its corresponding $R_c$ shown on the right.

$$\vec{b} = \frac{\vec{B}}{|\vec{B}|} \tag{4.5}$$

The inverse of the magnitude of $\vec{\kappa}\,(\frac{1}{|\vec{\kappa}|})$ at any point, gives the local $R_c$. We have plotted the corresponding $R_c$ of our initial magnetic fields in the right hand column of Figure 4.1. In all of the cases, $R_c$ is very high at the centre, implying near vertical fields, while at the edges the fieldlines are significantly curved. Clearly, the fieldlines become more curved as we progress from R10 to R30 (panels a - c). Note how the brighter band in the centre, becomes narrower from R10 to R30. One can predict thus, fluid elements can penetrate the furthest into the flux tube of R30 before meeting any resistance from strong vertical fields. A side effect of decreasing $R_c$ simply by continuously increasing the field strength at the lower boundary is that it keeps making the flux tube narrower at its base. We, therefore, carried out another experiment where we tried out a different initial condition. We superimposed two additional flux tubes on either side of the main flux tube used in R20, as shown in panel d of Figure 4.1. We did this because - 1) the enhanced field strength at the edges, close to the lower boundary, would help keep the flux tube coherent at the base of the simulation box (note that this run has the highest $R_c$ at the base) 2) the additional magnetic pressure around the centre of the flux tube, near the surface, would help the fieldlines fan out more and become even more inclined once the flux tube achieves pressure equilibrium, facilitating penumbral filament formation. We labeled this run R20E. Note that due to the superposed smaller tubes, the initial field strength at the base of the computational domain in this run locally reaches 30 kG at the edges.

### 4.2.2 Round spots

For our shallow round spot simulation we use an initial condition, which has a vertical cut similar to the vertical cut of the initial condition used in R20E. Two flux sheets were superimposed on either side of the main flux sheet and this was rotated axisymmetrically, while ensuring that $\nabla \cdot B = 0$. A vertical cut of the initial condition through the centre of the simulation box is shown in panel e of Figure 4.1.

### 4.2.3 Boundary Condition for the magnetic field

In the shallow sunspot simulation presented in Rempel (2011c), a lower boundary open to plasma flows inside the magnetic flux tube caused the sunspot to disintegrate completely within 6 hours. In our simulations, for all of the runs, we set all velocities to zero at the lower boundary for $|B| > 1000$ Gauss. This allows us to study the effects of the fluting instability with minimal interference from the lower boundary. At the upper boundary the magnetic field was made to have a potential field configuration.

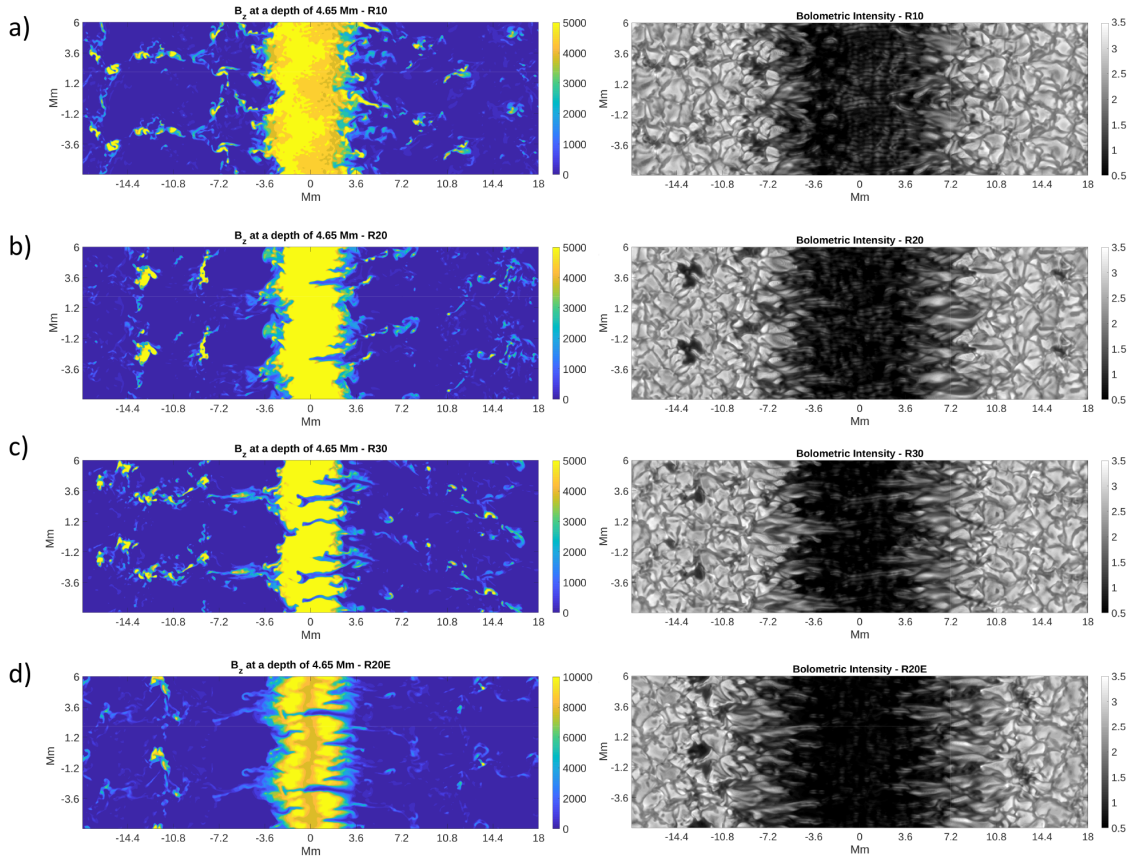


Figure 4.2: Left Panel: Horizontal cuts of $B_z$ of the slab geometry runs - R10, R20, R30, R20E, in Gauss at a depth of 4.65 Mm after 8 hours of solar runtime. Right Panel: The corresponding bolometric intensity maps in units of $10^{10}$ erg cm$^{-2}$ ster$^{-1}$ s$^{-1}$. The images have been repeated twice in the y-direction.

## 4.3 Results

### 4.3.1 Slab Geometry Runs

The left panel of Figure 4.2 shows horizontal cuts of $B_z$ at a depth of 4.65 Mm below the visible surface. It is clear that both the number of filament-like intrusions of the surrounding plasma and the lengths of such intrusions, increase as we increase the curvature of the initial flux tubes, as seen in the results of R10, R20 and R30. In all of the runs, the instability originates close to the middle of the box, where the curvature is maximum, and propagates both upwards and downwards. Some of these intrusions eventually manifest themselves at the surface in the intensity images as long penumbral filaments with thin dark cores (see right panel of Figure 4.2). The purpose of the runs in the slab geometry was to vary $R_c$ and see if it results in different amounts of fluting. Our results confirm that $R_c$ indeed controls the degree of fluting.

The run R20E exhibits properties that lie between R20 and R30 - the intrusions are plentiful but only a couple of them manage to reach the centre of the flux tube. At the surface, it develops the most expansive penumbra among the four cases, while having

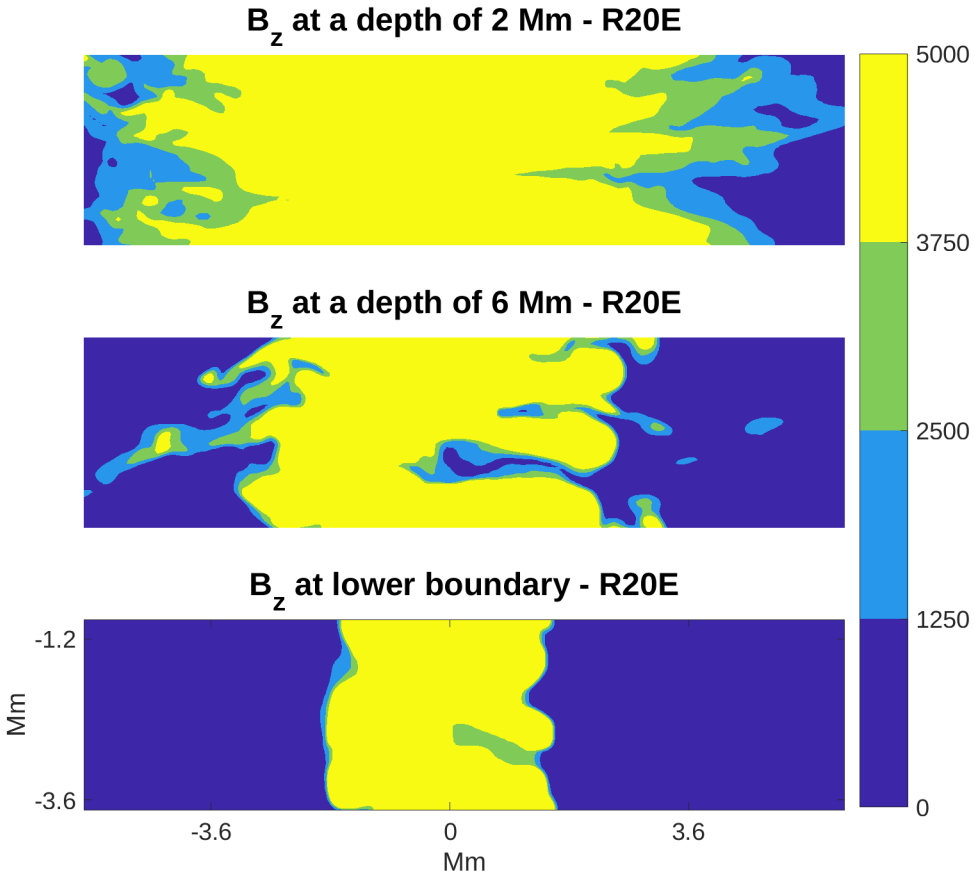


Figure 4.3: Zoomed in horizontal cuts of $B_z$ (Gauss) of the run R20E at different depths below the photosphere, after 8 hours of solar runtime. We have intentionally chosen only 4 contour levels to draw attention to the tongue like weak field regions at the edge of the flux tube caused by fluid penetrating from outside.

an umbra that is not distorted by intruding filaments. This indicates that our numerical experiment of superimposing two additional flux tubes achieved its intended purpose. This prompted us to choose the initial condition for the next circular spot simulation such that its vertical slice is similar to run R20E.

A side effect of the higher field strengths in the lower boundary is that the runs R30 and R20E have comparatively cleaner umbrae with fewer umbral dots.

In Figure 4.3 we have plotted horizontal cuts of $B_z$ at different depths of the R20E run. We have zoomed in on only a part of the flux tube so that we can investigate individual filaments. We have chosen only 4 contour levels so that we can easily discern the penetrating tongues of the external fluid. Notice that the tongue-like weak field regions are the most prominent at a depth of 6 Mm, while at the lower boundary and at a depth of 2 Mm only traces of the intrusions have appeared. It is clear that the fluting originates near the middle of the box and propagates both upwards and downwards through diffusive processes and pressure differences generated by the penetrating plasma. This demonstrates that the fluting is not merely a boundary effect.

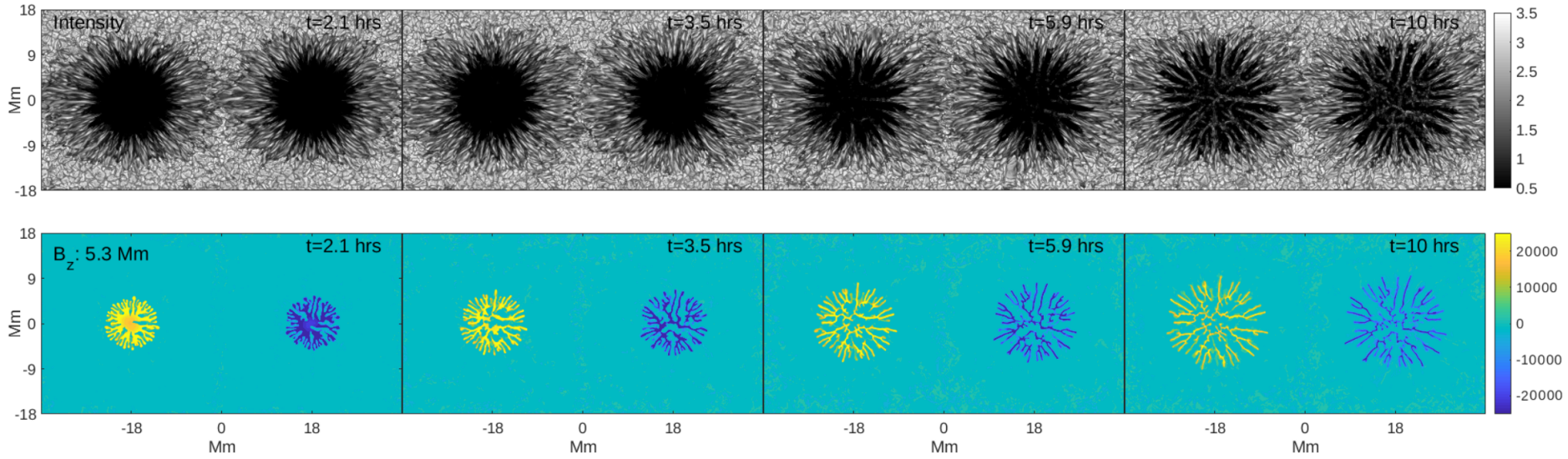


Figure 4.4: Temporal evolution of the circular spot simulation showing the advancement of the fluting instability. The top panel shows the emerging bolometric intensity in units of $10^{10}$ erg cm$^{-2}$ ster$^{-1}$ s$^{-1}$ at different stages of the evolution. The lower panel shows horizontal cuts of $B_z$ in Gauss at a depth of 5.3 Mm below the photosphere.

### 4.3.2 Round spots

For our circular spot simulation, we used initial conditions that are similar to the one used in run R20E. Close to the surface, the initial flux tube had strong vertical fields near the centre, while below a certain depth the field strength at the edges of the flux tube were enhanced. We have plotted in Figure 4.4 (part a) the evolution of the circular spot simulation in the shallow box. The top panel shows a series of intensity images at different stages of the evolution, while the bottom panel shows the corresponding horizontal cuts of $B_z$ at a depth of 5.3 Mm. As seen in the intensity image panel, the inclined fields near the surface and the presence of opposite polarities result in the formation of penumbral structures of considerable extent in both the positive and negative spots 2 hours into the run. By this time, the corresponding flux tubes already show a very high degree of fluting. In the subsequent time frames, the flux tubes get more and more distorted and 6 hours into the simulation they are no longer coherent and break up into disconnected fragments. The instability propagates upwards and we see the head of the filaments gradually penetrating the umbral regions. The last snapshot has been taken 10 hours into the run and by this time the umbra in the intensity image is completely covered with protruding filaments whose heads have migrated all the way to the center. The corresponding horizontal cut shows that the flux tubes are completely distorted and they are both reminiscent of the spaghetti-like structure hypothesized by Parker (1979). In our simulations, we see multiple flux sheets form, some of them loosely connected. It is important to note that in addition to being fluted the flux tubes are also continuously pulled apart by convection and we see the circumferences of both the tubes expanding with time. This accelerates the breaking up of the flux tubes into individual components which in turn facilitates the filaments at the surface to penetrate further into the umbrae. This is in agreement with Parker (1979) who suggested that in order to prevent a fluted flux tube from being completely pulled apart there must be a converging flow that holds the different parts together and in the absence of a converging flow in our simulations, the flux tubes simply break up. It is important to bear in mind that we had set all velocities at points with $|B| > 1000$ at the lower boundary to zero. However, the magnetic field at the lower boundary can still be transported by the external flow field and be weakened by filamentary intrusions from above, mediated by diffusive processes.

In Figure 4.5, we have presented after 3.5 solar hours the bolometric intensity image (panel a), horizontal cuts of the magnetic field at different depths (panels b-d), the vertical velocity profile at a depth of 2.5 Mm (panel e) and the velocity along the x direction at the $\tau = 1$ surface (panel f). At a depth of 5.3 Mm, the flux tubes are almost completely shredded after 3.5 hours of runtime. The instability, in this case, had originated closer to the lower boundary and propagated upwards as is evidenced by the decreasing severity of the fluting at depths of 2.5 Mm and the $\tau$=1 surface. In panel e, we have plotted $v_z$ at a depth of 2.5 Mm. We find that in the areas that correspond to the penetrating fluid at the edge of the flux tube, there is a systematic upflow. These upflows eventually help the intrusions manifest at the surface as lightbridges. At the centre of the flux tube $v_z$ becomes negligible. A noticeable feature in the intensity image is the extent of the penumbra. We have achieved an umbra:penumbra area ratio of around 1:4 which is in the range of what is observed on the Sun (Solanki 2003). This is a significant result since sunspot simulations typically use the upper boundary to achieve respectable penumbral

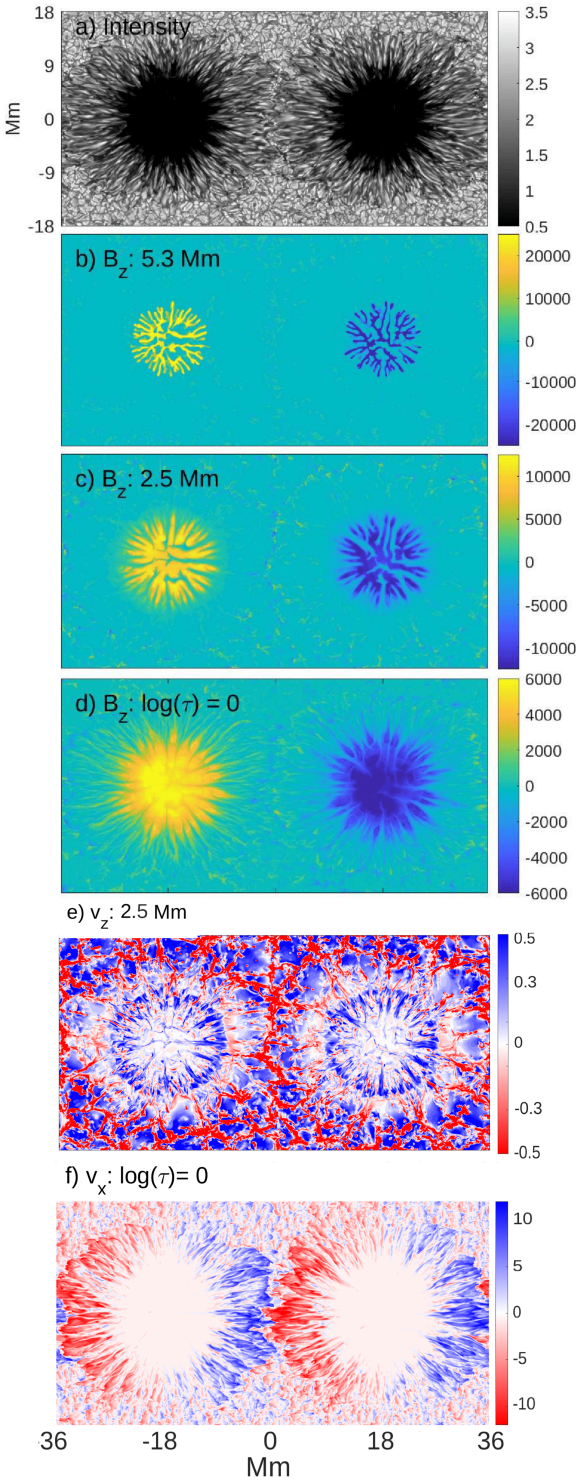


Figure 4.5: Snapshot of the circular spot simulation after 3.5 hours of solar runtime with the bolometric intensity image in the top panel (a), horizontal cuts of $B_z$ at two different depths (b-c) and at the $\tau$=1 surface (d). Panel *e* shows the vertical velocity profile at a depth of 2.5 Mm and panel *f* plots $v_x$ at the $\tau$=1 surface. The velocities are in units of km/s.

proportions. In contrast to Jurčák et al. (2020), who also used the subsurface structure of the sunspot to produce a penumbra, we obtain Evershed flows that have the correct orientation (panel f). We, however, also obtain umbral field strengths that are higher than what is what is typically observed, like Jurčák et al. (2020). The periodicity of the horizontal boundaries makes the penumbra slightly asymmetric and it is more elongated in the x-direction, where the opposite polarities meet.

## 4.4 Conclusion

We have simulated complete sunspots that naturally form penumbral filaments and have further demonstrated that sunspots with highly curved flux tubes may have subsurface structures which are close to the cluster model proposed by Parker (1979). Our simulations lead us to make the following conclusions about the nature of sunspots -

1) It is quite clear that the initial subsurface structure plays an important role in the formation of penumbral filaments and the stability of sunspots. Highly curved flux tubes are indeed vulnerable to the fluting instability, as had been speculated by many authors before. Our experiments in the slab geometry where we systematically varied the curvature of the initial flux tube confirm that the intrusions of plasma into the flux tubes are indeed due to the fluting instability and we could control the degree of fluting to some extent by continuously decreasing the radius of curvature.

2) Our circular spot simulation has strong horizontal fields and consequently develops extended penumbral filaments that harbour the Evershed flow.

3) Our simulations suggest that even sunspots with little structuring at the surface might already be highly fluted underneath and eventually the subsurface structuring is manifested at the surface through penumbral filaments encroaching into the umbra. The nearly field-free material typical of such intruding filaments reach down 5 Mm or more in our simulations. Whether sunspots anchored deep in the convection zone can keep the spaghetti-like structure from being torn apart, as predicted by Spruit (1981), remains an open question. Sunspot simulations that cover the full convection zone, such as the one by Hotta and Iijima (2020), can be used to answer this question.

# 5 Conclusion and Outlook

## 5.1 Conclusion

We performed the first radiative-MHD simulations of spots on stars other than the Sun, namely the spectral types - K0V and M0V. Here I state our most important findings:

1. **Temperature contrast**: Starspot temperature is dependent on the host star's photospheric temperature. Hotter stars harbor spots with higher temperature contrasts. This is because the continuum opacity has a strong dependence on temperature in the 4000-6000 K range. In less opaque (or more transparent) atmospheres, radiative processes play a role in energy transport even below the photosphere and this changes how much the presence of strong magnetic fields affects energy transport.

2. **Wilson Depression**: The Wilson Depression has a larger value in hotter stars with rarefied atmospheres. In the colder and denser M0V star, the Wilson Depression of its spot is an order of magnitude less than that of the spot on the G2V star.

3. **Magnetic field strength**: The umbral magnetic field strength is largely determined by the external gas pressure at the height where the $\tau$ =1 surface of the umbra forms. Thus, two competing factors are at play here - 1) surface pressure of the star (increases from G to M) and 2) the Wilson depression (decreases from G to M). All of our umbral field strengths lie in the range 3-4.5 kG.

Further, we used our simulated starspot atmospheres to take steps towards modelling quantities that can be directly observed - continuum spot contrasts in the visible and the infrared, Stokes profiles, and stellar RV with the effect of spots included. These are the key points we learned from this exercise:

1. Spot intensity contrast with respect to their surrounding photospheric brightness is fairly independent of the viewing angle for all of the spectral types.

2. The strength of lines and their degree of polarization is strongly affected by both magnetic field strength, temperature and often their gradients. This indicates that synthetic spectral lines calculated from simple 1D atmospheres are likely to be inaccurate.

3. We find that spots can significantly affect RV measurements not just because they cause a loss in the flux of photons, but because they inhibit convection and harbour flows of their own. We recommend constraining flows inside spots more accurately through simulations and observations.

Our efforts to constrain the initial conditions of magnetic fields in the starspot simulations lead to an interesting discovery - initial magnetic conditions that allow starspots to have penumbral filaments also make them susceptible to interchange instabilities. We conducted a separate study on the nature of sunspot flux tubes underneath the visible surface. We drew the following conclusions from this study -

1. The subsurface structure of sunspots plays a role in their stability. Highly curved flux tubes are susceptible to the fluting instability and the instability manifests itself as lightbridges at the photosphere.

2. The presence of strong horizontal fields at the surface in our simulations, a consequence of a highly curved initial flux tube, facilitated the formations of expansive penumbral filaments.

## 5.2 Outlook

This thesis marks the beginning of an exciting new field of research - near surface starspot simulations. Naturally, there are plenty of problems to explore and I will discuss the ways that we can build on the work presented in this thesis.

1. **Complete starspots** - An obvious next step is to compute complete circular spots. The main limitation of the slab geometry is that it results in stunted penumbral filaments. In Figure 5.1 we have plotted the intensity images of a circular G2V spot and a M0V spot. The penumbral filaments are clearly much more expansive than the slab geometry simulations and the G2V spot looks much more similar to observed sunspots. This geometry therefore not only provides more realistic starspots, but will also allow us to compare more easily the large scale penumbral properties on different spectral types. Reassuringly, the circular spots have intensity contrasts similar to what we obtained in our slab geometry simulations. Note the difference between the penumbra of the two spots. While the sunspot penumbra shows a wide range of intensities and alternating bright and dark bands, the penumbra of the M spot is much more homogeneous. Also, the G2V penumbra is visibly darker than the quiet star while the M0V is almost as bright as its surroundings.

2. **More spectral types: dwarfs and subgiants** - We found a relationship between spot temperature contrast and stellar surface temperature for the spectral types G2V, K0V and M0V. We have to simulate more spectral types to find out if this relationship holds true for a wider range of stellar temperatures and luminosity classes. It will be also interesting to study how penumbral properties vary with stellar type. Simulating spots on subgiants are also important as our knowledge on starspots primarily stems from studies on RS CVn stars (typically luminosity class IV). The Wilson depressions will be huge on these stars which might effect the contrast and magnetic field strength in unforseeable ways.

3. **Spots of different sizes** - On the sun, the brightness of a spot is dependent on spot size. Larger spots tend to be darker (Mathew et al. 2007, Schad 2014a). In this thesis, we have compared spots of similar granule sizes. Does size have an impact

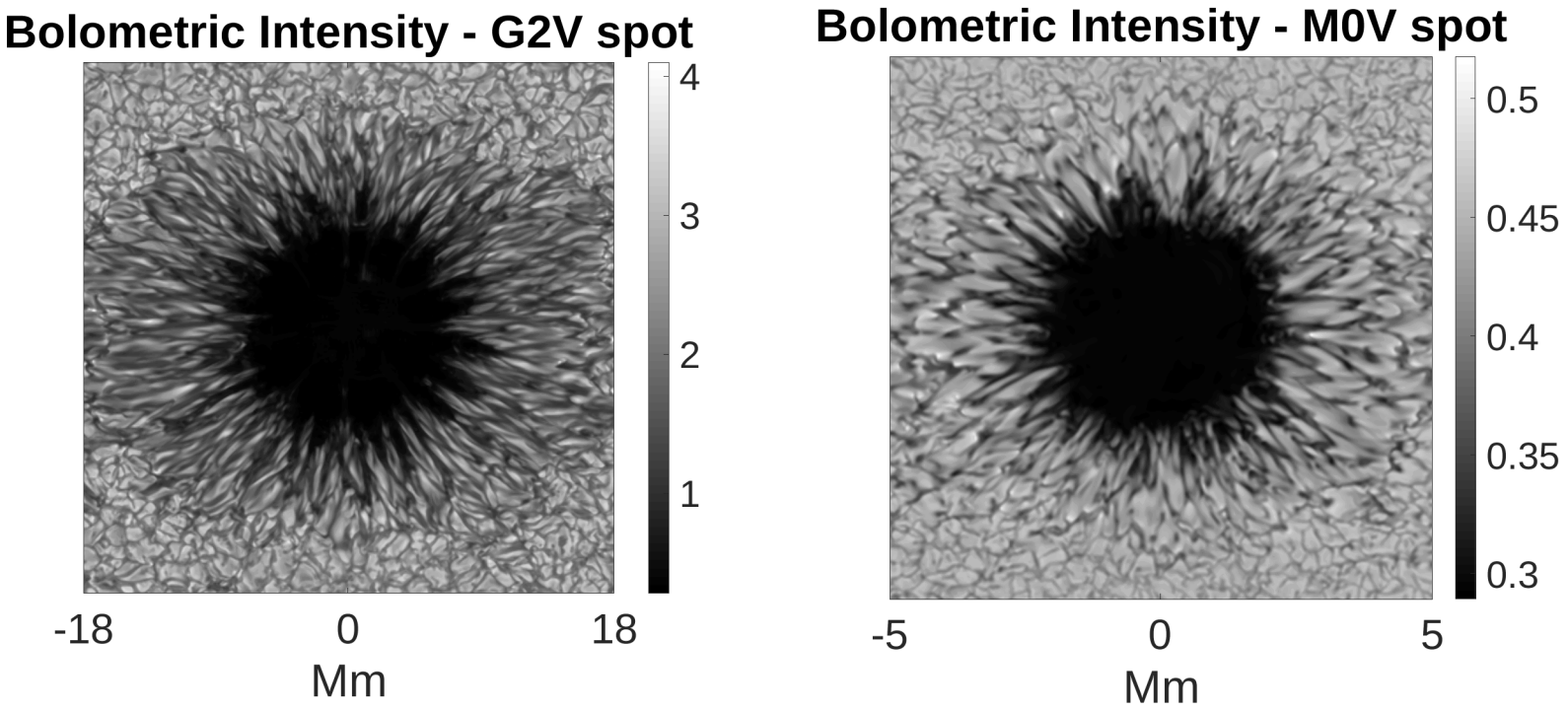


Figure 5.1: Bolometric intensity images of complete G2V and M0V spot simulations in units of $10^{10}$ erg cm$^{-2}$ ster$^{-1}$ s$^{-1}$.

on spot contrast on other spectral types? If so, how much does size affect spot brightness, magnetic field and internal velocities?

4. **Spot Lifetimes** - Recently Giles et al. (2017) found that starspot lifetimes depend on spectral type. Spots seem to last longer on cooler stars. They speculated that stars that are hotter have higher convective velocities at their photosphere which enables faster diffusion of magnetic flux. We can study this problem using simulation boxes with large horizontal extents and putting in spots of different radii. Since we are not interested in the fine structure of spots for this problem, we can use a lower spatial resolution for the simulations.

5. **Massive Spots** - ZDI has detected very large spots on other stars that cover significant fractions of the stellar disk (for example, see Flores et al. (2020), Cang et al. (2020)). Also average field strengths in the kiloGauss range are regularly found on M stars. Therefore, an interesting numerical experiment to conduct would be to insert kiloGauss order vertical magnetic fields in boxes of large horizontal extents (several super-granules) and see if such large magnetic structures are stable against convection. Similar to the previous problem this can be carried out in low resolution.

6. **Effect of spots on RV** - We conducted some preliminary studies on how spots can affect stellar RV. In order to make our calculations more realistic we can take the following steps:

   (a) Add the contribution of plages to the disk-integrated line profiles.

   (b) Add the effects of rotation.

7. **Synthetic Lightcurve modulations** - We can compute the brightness contrasts of the spots in the various wavelength bands in which planet-hunting telescopes, such as Kepler, TESS, in future PLATO (but also ground based telescopes) observe. Then we can put artificial spots on stellar surfaces and see how large the modulation of the lightcurves are.

8. **Observational Diagnostics** - We can test and show how strongly spots contribute to the DI and ZDI signals on different types of stars. We can further compute molecular bands (primarily TiO, but also CH, CO, CN) to calibrate these as diagnostics of starspot properties, including polarisation to determine magnetic field. Since molecular lines are stronger in the spots, they partly overcome the problem of the continuum being lower in spots.

# Bibliography


Afram, N. and Berdyugina, S. V.: 2015, *A&A* **576**, A34

Afram, N. and Berdyugina, S. V.: 2019, *A&A* **629**, A83

Afram, N. and Berdyugina, S. V.: 2015, *A&A* **576**, A34

Afram, N. and Berdyugina, S. V.: 2019, *A&A* **629**, A83

Albregtsen, F. and Maltby, P.: 1978, *Nature* **274(5666)**, 41

Basri, G. and Shah, R.: 2020, *The Astrophysical Journal* **901(1)**, 14

Bauer, F. F., Reiners, A., Beeck, B., and Jeffers, S. V.: 2018, *A&A* **610**, A52

Beeck, B., Cameron, R. H., Reiners, A., and Schüssler, M.: 2013a, *A&A* **558**, A48

Beeck, B., Cameron, R. H., Reiners, A., and Schüssler, M.: 2013b, *A&A* **558**, A49

Beeck, B., Collet, R., Steffen, M., Asplund, M., Cameron, R. H., Freytag, B., Hayek, W., Ludwig, H. G., and Schüssler, M.: 2012, *A&A* **539**, A121

Beeck, B., Schüssler, M., Cameron, R. H., and Reiners, A.: 2015a, *A&A* **581**, A42

Beeck, B., Schüssler, M., Cameron, R. H., and Reiners, A.: 2015b, *A&A* **581**, A43

Beeck, B., Schüssler, M., and Reiners, A.: 2011a, *MHD Simulations Reveal Crucial Differences Between Solar and Very Cool Star Magnetic Structures*, Vol. 448 of *Astronomical Society of the Pacific Conference Series*, p. 1071

Beeck, B., Schüssler, M., and Reiners, A.: 2011b, in C. Johns-Krull, M. K. Browning, and A. A. West (eds.), *16th Cambridge Workshop on Cool Stars, Stellar Systems, and the Sun*, Vol. 448 of *Astronomical Society of the Pacific Conference Series*, p. 1071

Bellot-Rubio, L. R., Tsuneta, S., Ichimoto, K., Katsukawa, Y., Lites, B. W., Nagata, S., Shimizu, T., Shine, R. A., Suematsu, Y., Tarbell, T. D., Title, A. M., and del Toro Iniesta, J. C.: 2007, *The Astrophysical Journal* **668(1)**, L91

Benko, M., González Manrique, S. J., Balthasar, H., Gömöry, P., Kuckein, C., and Jurčák, J.: 2018a, *A&A* **620**, A191

Benko, M., González Manrique, S. J., Balthasar, H., Gömöry, P., Kuckein, C., and Jurčák, J.: 2018b, *A&A* **620**, A191

Berdyugina, S. V.: 2005, *Living Reviews in Solar Physics* **2(1)**, 8

Berdyugina, S. V. and Usoskin, I. G.: 2003, *A&A* **405**, 1121

Bharti, L., Joshi, C., and Jaaffrey, S. N. A.: 2007, *ApJ* **669(1)**, L57

Bogdan, T. J. and Judge, P. G.: 2006, *Philosophical Transactions of the Royal Society of London Series A* **364(1839)**, 313

Borgniet, S., Meunier, N., and Lagrange, A. M.: 2015, *A&A* **581**, A133

Borrero, J. M., Franz, M., Schlichenmaier, R., Collados, M., and Asensio Ramos, A.: 2017, *A&A* **601**, L8

Borrero, J. M. and Ichimoto, K.: 2011, *Living Reviews in Solar Physics* **8(1)**, 4

Brown, S. F., Donati, J. F., Rees, D. E., and Semel, M.: 1991, *A&A* **250**, 463

Bruls, J. H. M. J., Solanki, S. K., and Schuessler, M.: 1998, *A&A* **336**, 231

Budding, E.: 1977, *Ap&SS* **48(1)**, 207

Butler, R. P., Bedding, T. R., Kjeldsen, H., McCarthy, C., O'Toole, S. J., Tinney, C. G., Marcy, G. W., and Wright, J. T.: 2004, *ApJ* **600(1)**, L75

Cang, T. Q., Petit, P., Donati, J. F., Folsom, C. P., Jardine, M., Villarreal D'Angelo, C., Vidotto, A. A., Marsden, S. C., Gallet, F., and Zaire, B.: 2020, *arXiv e-prints* p. arXiv:2008.12120

Carroll, T. A., Kopf, M., Ilyin, I., and Strassmeier, K. G.: 2007, *Astronomische Nachrichten* **328(10)**, 1043

Castellanos Durán, J. S., Lagg, A., Solanki, S. K., and van Noort, M.: 2020, *ApJ* **895(2)**, 129

Catalano, S., Biazzo, K., Frasca, A., and Marilli, E.: 2002a, *A&A* **394**, 1009

Catalano, S., Biazzo, K., Frasca, A., and Marilli, E.: 2002b, *A&A* **394**, 1009

Catalano, S., Biazzo, K., Frasca, A., and Marilli, E.: 2002c, *A&A* **394**, 1009

Cegla, H. M., Shelyag, S., Watson, C. A., and Mathioudakis, M.: 2013, *ApJ* **763(2)**, 95

Chabrier, G. and Baraffe, I.: 1997, *A&A* **327**, 1039

Cheung, M. C. M., Rempel, M., Title, A. M., and Schüssler, M.: 2010, *ApJ* **720(1)**, 233

Choudhuri, A. R.: 2010, *Astrophysics for Physicists*

Collier Cameron, A. and Unruh, Y. C.: 1994, *MNRAS* **269**, 814

Cowling, T. G.: 1946, *MNRAS* **106**, 218

Demircan, O. and Kahraman, G.: 1991, *Ap&SS* **181(2)**, 313

Desort, M., Lagrange, A. M., Galland, F., Udry, S., and Mayor, M.: 2007, *A&A* **473(3)**, 983

Donati, J. F., Brown, S. F., Semel, M., Rees, D. E., Dempsey, R. C., Matthews, J. M., Henry, G. W., and Hall, D. S.: 1992, *A&A* **265**, 682

Donati, J. F. and Landstreet, J. D.: 2009, *ARA&A* **47(1)**, 333

Donati, J. F. and Semel, M.: 1990, *Solar Physics* **128(1)**, 227

Donati, J. F., Semel, M., and Praderie, F.: 1989, *A&A* **225**, 467

Dorren, J. D. and Guinan, E. F.: 1994, *ApJ* **428**, 805

Dumusque, X., Boisse, I., and Santos, N. C.: 2014a, *ApJ* **796(2)**, 132

Dumusque, X., Boisse, I., and Santos, N. C.: 2014b, *ApJ* **796(2)**, 132

Dumusque, X., Udry, S., Lovis, C., Santos, N. C., and Monteiro, M. J. P. F. G.: 2011, *A&A* **525**, A140

Eddington, A. S.: 1930, *The Internal Constitution of the Stars*, Cambridge Science Classics, Cambridge University Press

Eker, Z., Soydugan, F., Soydugan, E., Bilir, S., Yaz Gökçe, E., Steer, I., Tüysüz, M., Şenyüz, T., and Demircan, O.: 2015, *AJ* **149(4)**, 131

Espinoza, N., Rackham, B. V., Jordán, A., Apai, D., López-Morales, M., Osip, D. J., Grimm, S. L., Hoeijmakers, J., Wilson, P. A., Bixel, A., McGruder, C., Rodler, F., Weaver, I., Lewis, N. K., Fortney, J. J., and Fraine, J.: 2018, *Monthly Notices of the Royal Astronomical Society* **482(2)**, 2065

Evershed, J.: 1909, *Monthly Notices of the Royal Astronomical Society* **69(5)**, 454

Flores, C., Reipurth, B., and Connelley, M. S.: 2020, *ApJ* **898(2)**, 109

Franz, M., Collados, M., Bethge, C., Schlichenmaier, R., Borrero, J. M., Schmidt, W., Lagg, A., Solanki, S. K., Berkefeld, T., Kiess, C., Rezaei, R., Schmidt, D., Sigwarth, M., Soltau, D., Volkmer, R., von der Luhe, O., Waldmann, T., Orozco, D., Pastor Yabar, A., Denker, C., Balthasar, H., Staude, J., Hofmann, A., Strassmeier, K., Feller, A., Nicklas, H., Kneer, F., and Sobotka, M.: 2016, *A&A* **596**, A4

Frasca, A., Biazzo, K., Taș, G., Evren, S., and Lanzafame, A. C.: 2008, *A&A* **479(2)**, 557

Freytag, B., Steffen, M., Ludwig, H. G., Wedemeyer-Böhm, S., Schaffenberger, W., and Steiner, O.: 2012, *Journal of Computational Physics* **231(3)**, 919

Frutiger, C., Solanki, S. K., Fligge, M., and Bruls, J. H. M. J.: 2000, *A&A* **358**, 1109

García-Alvarez, D., Lanza, A. F., Messina, S., Drake, J. J., van Wyk, F., Shobbrook, R. R., Butler, C. J., Kilkenny, D., Doyle, J. G., and Kashyap, V. L.: 2011, *A&A* **533**, A30

Giles, H. A. C., Collier Cameron, A., and Haywood, R. D.: 2017, *MNRAS* **472(2)**, 1618

Goncharskii, A. V., Stepanov, V. V., Kokhlova, V. L., and Yagola, A. G.: 1977a, *Soviet Astronomy Letters* **3**, 147

Goncharskii, A. V., Stepanov, V. V., Kokhlova, V. L., and Yagola, A. G.: 1977b, *Soviet Astronomy Letters* **3**, 147

Gray, D. F.: 1984, *ApJ* **277**, 640

Gray, D. F.: 1996, *Symposium - International Astronomical Union* **176**, 227–236

Gray, D. F.: 1996, in K. G. Strassmeier and J. L. Linsky (eds.), *Stellar Surface Structure*, Vol. 176 of *IAU Symposium*, p. 227

Griffiths, S. C., Hicks, R. B., and Milone, E. F.: 1988, *JRASC* **82**, 1

Guglielmino, S. L., Zuccarello, F., and Romano, P.: 2014, *ApJ* **786(2)**, L22

Hansen, C. J. and Kawaler, S. D.: 1994, *Stellar Interiors. Physical Principles, Structure, and Evolution.*

Hatzes, A. P.: 2002a, *Astronomische Nachrichten* **323**, 392

Hatzes, A. P.: 2002b, *Astronomische Nachrichten* **323**, 392

Hatzes, A. P. and Vogt, S. S.: 1992, *MNRAS* **258**, 387

Heinemann, T., Nordlund, Å., Scharmer, G. B., and Spruit, H. C.: 2007, *ApJ* **669(2)**, 1390

Hotta, H. and Iijima, H.: 2020, *MNRAS* **494(2)**, 2523

Hotta, H. and Toriumi, S.: 2020, *arXiv e-prints* p. arXiv:2008.07741

Huenemoerder, D. P. and Ramsey, L. W.: 1987a, *ApJ* **319**, 392

Huenemoerder, D. P. and Ramsey, L. W.: 1987b, *ApJ* **319**, 392

Hussain, G. A. J.: 2002, *Astronomische Nachrichten* **323**, 349

Işık, E., Shapiro, A. I., Solanki, S. K., and Krivova, N. A.: 2020, *ApJ* **901(1)**, L12

Järvinen, S. P., Berdyugina, S. V., Tuominen, I., Cutispoto, G., and Bos, M.: 2005, *A&A* **432(2)**, 657

Johns-Krull, C. M.: 1996, *A&A* **306**, 803

Jurčák, J., Schmassmann, M., Rempel, M., Bello González, N., and Schlichenmaier, R.: 2020, *A&A* **638**, A28

Keller, C. U., Schssler, M., Vgler, A., and Zakharov, V.: 2004, *The Astrophysical Journal* **607(1)**, L59

Kiess, C., Rezaei, R., and Schmidt, W.: 2014, *A&A* **565**, A52

Kopp, G. and Rabin, D.: 1992, *Sol. Phys.* **141(2)**, 253

Kosugi, T., Matsuzaki, K., Sakao, T., Shimizu, T., Sone, Y., Tachikawa, S., Hashimoto, T., Minesugi, K., Ohnishi, A., Yamada, T., Tsuneta, S., Hara, H., Ichimoto, K., Suematsu, Y., Shimojo, M., Watanabe, T., Shimada, S., Davis, J. M., Hill, L. D., Owens, J. K., Title, A. M., Culhane, J. L., Harra, L. K., Doschek, G. A., and Golub, L.: 2008, *The Hinode (Solar-B) Mission: An Overview*, pp 5–19, Springer New York, New York, NY

Lagg, A., Solanki, S. K., van Noort, M., and Danilovic, S.: 2014, *A&A* **568**, A60

Lagrange, A. M., Desort, M., and Meunier, N.: 2010, *A&A* **512**, A38

Langhans, K., Scharmer, G. B., Kiselman, D., and Löfdahl, M. G.: 2007a, *A&A* **464(2)**, 763

Langhans, K., Scharmer, G. B., Kiselman, D., and Löfdahl, M. G.: 2007b, *A&A* **464(2)**, 763

Lanza, A. F., Bonomo, A. S., Moutou, C., Pagano, I., Messina, S., Leto, G., Cutispoto, G., Aigrain, S., Alonso, R., Barge, P., Deleuil, M., Auvergne, M., Baglin, A., and Collier Cameron, A.: 2010, *A&A* **520**, A53

Lanza, A. F., Pagano, I., Leto, G., Messina, S., Aigrain, S., Alonso, R., Auvergne, M., Baglin, A., Barge, P., Bonomo, A. S., Boumier, P., Collier Cameron, A., Comparato, M., Cutispoto, G., de Medeiros, J. R., Foing, B., Kaiser, A., Moutou, C., Parihar, P. S., Silva-Valio, A., and Weiss, W. W.: 2009, *A&A* **493(1)**, 193

Lavail, A., Kochukhov, O., and Hussain, G. A. J.: 2019, *A&A* **630**, A99

Leka, K. D. and Skumanich, A.: 1998, *ApJ* **507(1)**, 454

Lites, B. W., Elmore, D. F., Seagraves, P., and Skumanich, A. P.: 1993, *ApJ* **418**, 928

Livingston, W.: 2002, *Sol. Phys.* **207(1)**, 41

Löhner-Böttcher, J., Schmidt, W., Schlichenmaier, R., Doerr, H. P., Steinmetz, T., and Holzwarth, R.: 2018a, *A&A* **617**, A19

Löhner-Böttcher, J., Schmidt, W., Stief, F., Steinmetz, T., and Holzwarth, R.: 2018b, *A&A* **611**, A4

Löptien, B., Lagg, A., van Noort, M., and Solanki, S. K.: 2020, *A&A* **635**, A202

Louis, R. E., Mathew, S. K., Bellot Rubio, L. R., Ichimoto, K., Ravindra, B., and Raja Bayanna, A.: 2012a, *ApJ* **752(2)**, 109

Louis, R. E., Ravindra, B., Mathew, S. K., Bellot Rubio, L. R., Raja Bayanna, A., and Venkatakrishnan, P.: 2012b, *ApJ* **755(1)**, 16

Louis, R. E., Ravindra, B., Mathew, S. K., Rubio, L. R. B., Bayanna, A. R., and Venkatakrishnan, P.: 2012, *The Astrophysical Journal* **755(1)**, 16

Magic, Z., Collet, R., Asplund, M., Trampedach, R., Hayek, W., Chiavassa, A., Stein, R. F., and Nordlund, Å.: 2013a, *A&A* **557**, A26

Magic, Z., Collet, R., Asplund, M., Trampedach, R., Hayek, W., Chiavassa, A., Stein, R. F., and Nordlund, Å.: 2013b, *A&A* **557**, A26

Maltby, P., Avrett, E. H., Carlsson, M., Kjeldseth-Moe, O., Kurucz, R. L., and Loeser, R.: 1986, *ApJ* **306**, 284

Mancini, L., Ciceri, S., Chen, G., Tregloan-Reed, J., Fortney, J. J., Southworth, J., Tan, T. G., Burgdorf, M., Calchi Novati, S., Dominik, M., Fang, X. S., Finet, F., Gerner, T., Hardis, S., Hinse, T. C., Jørgensen, U. G., Liebig, C., Nikolov, N., Ricci, D., Schäfer, S., Schönebeck, F., Skottfelt, J., Wertz, O., Alsubai, K. A., Bozza, V., Browne, P., Dodds, P., Gu, S. H., Harpsøe, K., Henning, T., Hundertmark, M., Jessen-Hansen, J., Kains, N., Kerins, E., Kjeldsen, H., Lund, M. N., Lundkvist, M., Madhusudhan, N., Mathiasen, M., Penny, M. T., Prof, S., Rahvar, S., Sahu, K., Scarpetta, G., Snodgrass, C., and Surdej, J.: 2013, *MNRAS* **436(1)**, 2

Mancini, L., Ciceri, S., Chen, G., Tregloan-Reed, J., Fortney, J. J., Southworth, J., Tan, T. G., Burgdorf, M., Calchi Novati, S., Dominik, M., Fang, X.-S., Finet, F., Gerner, T., Hardis, S., Hinse, T. C., Jørgensen, U. G., Liebig, C., Nikolov, N., Ricci, D., Schäfer, S., Schönebeck, F., Skottfelt, J., Wertz, O., Alsubai, K. A., Bozza, V., Browne, P., Dodds, P., Gu, S.-H., Harpsøe, K., Henning, T., Hundertmark, M., Jessen-Hansen, J., Kains, N., Kerins, E., Kjeldsen, H., Lund, M. N., Lundkvist, M., Madhusudhan, N., Mathiasen, M., Penny, M. T., Prof, S., Rahvar, S., Sahu, K., Scarpetta, G., Snodgrass, C., and Surdej, J.: 2013, *Monthly Notices of the Royal Astronomical Society* **436(1)**, 2

Martinez Pillet, V. and Vazquez, M.: 1993, *A&A* **270(1-2)**, 494

Mathew, S. K., Martínez Pillet, V., Solanki, S. K., and Krivova, N. A.: 2007, *A&A* **465(1)**, 291

Mayor, M. and Queloz, D.: 1995, *Nature* **378(6555)**, 355

Meunier, N., Desort, M., and Lagrange, A. M.: 2010, *A&A* **512**, A39

Meyer, F., Schmidt, H. U., and Weiss, N. O.: 1977, *MNRAS* **179**, 741

Moore, R. L.: 1981, *Space Sci. Rev.* **28(4)**, 387

Moradi, H., Baldner, C., Birch, A. C., Braun, D. C., Cameron, R. H., Duvall, T. L., Gizon, L., Haber, D., Hanasoge, S. M., Hindman, B. W., Jackiewicz, J., Khomenko, E., Komm, R., Rajaguru, P., Rempel, M., Roth, M., Schlichenmaier, R., Schunker, H., Spruit, H. C., Strassmeier, K. G., Thompson, M. J., and Zharkov, S.: 2010, *Sol. Phys.* **267(1)**, 1

Morris, B. M., Hebb, L., Davenport, J. R. A., Rohn, G., and Hawley, S. L.: 2017, *ApJ* **846(2)**, 99

Muller, R.: 1976, *Sol. Phys.* **48(1)**, 101

Murabito, M., Romano, P., Guglielmino, S. L., Zuccarello, F., and Solanki, S. K.: 2016, *ApJ* **825(1)**, 75

Namekata, K., Maehara, H., Notsu, Y., Toriumi, S., Hayakawa, H., Ikuta, K., Notsu, S., Honda, S., Nogami, D., and Shibata, K.: 2019, *The Astrophysical Journal* **871(2)**, 187

Neff, J. E., O'Neal, D., and Saar, S. H.: 1995a, *ApJ* **452**, 879

Neff, J. E., O'Neal, D., and Saar, S. H.: 1995b, *ApJ* **452**, 879

Nordlund, A.: 1982, *A&A* **107**, 1

Nordlund, A.: 1984, in S. L. Keil (ed.), *Small-Scale Dynamical Processes in Quiet Stellar Atmospheres*, p. 181

Nordlund, A.: 1985, *Sol. Phys.* **100**, 209

Nordlund, A. and Dravins, D.: 1990a, *A&A* **228**, 155

Nordlund, A. and Dravins, D.: 1990b, *A&A* **228**, 155

Nordlund, Å., Stein, R. F., and Asplund, M.: 2009, *Living Reviews in Solar Physics* **6(1)**, 2

Norton, A. A. and Gilman, P. A.: 2004, *ApJ* **603(1)**, 348

Okamoto, T. J. and Sakurai, T.: 2018, *ApJ* **852(1)**, L16

Olah, K., Hall, D. S., and Henry, G. W.: 1991, *A&A* **251**, 531

O'Neal, D., Neff, J. E., Saar, S. H., and Cuntz, M.: 2004, *AJ* **128**, 1802

O'Neal, D., Saar, S. H., and Neff, J. E.: 1996a, *ApJ* **463**, 766

O'Neal, D., Saar, S. H., and Neff, J. E.: 1996b, *ApJ* **463**, 766

Panja, M., Cameron, R., and Solanki, S. K.: 2020, *ApJ* **893(2)**, 113

Parker, E. N.: 1979, *ApJ* **230**, 905

Pelt, J., Brooke, J. M., Korpi, M. J., and Tuominen, I.: 2006, *A&A* **460(3)**, 875

Penn, M. J. and Livingston, W.: 2006, *ApJ* **649(1)**, L45

Petrovay, K. and van Driel-Gesztelyi, L.: 1997, *Sol. Phys.* **176(2)**, 249

Reiners, A.: 2012, *Living Reviews in Solar Physics* **9(1)**, 1

Reiners, A., Basri, G., and Browning, M.: 2009, *ApJ* **692(1)**, 538

Rempel, M.: 2011a, *The Astrophysical Journal* **729(1)**, 5

Rempel, M.: 2011b, *The Astrophysical Journal* **740(1)**, 15

Rempel, M.: 2011c, *The Astrophysical Journal* **740(1)**, 15

Rempel, M.: 2012, *The Astrophysical Journal* **750(1)**, 62

Rempel, M.: 2015, *ApJ* **814**, 125

Rempel, M., Schüssler, M., Cameron, R. H., and Knölker, M.: 2009a, *Science* **325**, 171

Rempel, M., Schüssler, M., and Knölker, M.: 2009b, *ApJ* **691**, 640

Rezaei, R., Beck, C., Lagg, A., Borrero, J. M., Schmidt, W., and Collados, M.: 2015, *A&A* **578**, A43

Riethmüller, T. L., Solanki, S. K., and Lagg, A.: 2008, *ApJ* **678(2)**, L157

Riethmüller, T. L., Solanki, S. K., van Noort, M., and Tiwari, S. K.: 2013, *A&A* **554**, A53

Rimmele, T.: 2008, *ApJ* **672(1)**, 684

Robertson, P., Mahadevan, S., Endl, M., and Roy, A.: 2014, **345(6195)**, 440

Roettenbacher, R. M., Monnier, J. D., Korhonen, H., Aarnio, A. N., Baron, F., Che, X., Harmon, R. O., Kővári, Z., Kraus, S., Schaefer, G. H., Torres, G., Zhao, M., Ten Brummelaar, T. A., Sturmann, J., and Sturmann, L.: 2016, *Nature* **533(7602)**, 217

Rogers, F. J., Swenson, F. J., and Iglesias, C. A.: 1996, *ApJ* **456**, 902

Romano, P., Frasca, D., Guglielmino, S. L., Ermolli, I., Tritschler, A., Reardon, K. P., and Zuccarello, F.: 2013, *ApJ* **771(1)**, L3

Rüedi, I., Solanki, S. K., Keller, C. U., and Frutiger, C.: 1998, *A&A* **338**, 1089

Saar, S. H. and Donahue, R. A.: 1997, *ApJ* **485(1)**, 319

Salhab, R. G., Steiner, O., Berdyugina, S. V., Freytag, B., Rajaguru, S. P., and Steffen, M.: 2018a, *A&A* **614**, A78

Salhab, R. G., Steiner, O., Berdyugina, S. V., Freytag, B., Rajaguru, S. P., and Steffen, M.: 2018b, *A&A* **614**, A78

Schad, T. A.: 2014a, *Sol. Phys.* **289(5)**, 1477

Schad, T. A.: 2014b, *Sol. Phys.* **289(5)**, 1477

Schad, T. A. and Penn, M. J.: 2010, *Sol. Phys.* **262(1)**, 19

Scharmer, G. B., Gudiksen, B. V., Kiselman, D., Löfdahl, M. G., and Rouppe van der Voort, L. H. M.: 2002, *Nature* **420(6912)**, 151

Schüssler, M. and Vögler, A.: 2006, *ApJ* **641(1)**, L73

Semel, M.: 1989a, *A&A* **225**, 456

Semel, M.: 1989b, *A&A* **225**, 456

Shimizu, T., Ichimoto, K., and Suematsu, Y.: 2012, *ApJ* **747(2)**, L18

Shulyak, D., Reiners, A., Nagel, E., Tal-Or, L., Caballero, J. A., Zechmeister, M., Béjar, V. J. S., Cortés-Contreras, M., Martin, E. L., Kaminski, A., Ribas, I., Quirrenbach, A., Amado, P. J., Anglada-Escudé, G., Bauer, F. F., Dreizler, S., Guenther, E. W., Henning, T., Jeffers, S. V., Kürster, M., Lafarga, M., Montes, D., Morales, J. C., and Pedraz, S.: 2019, *A&A* **626**, A86

Siu-Tapia, A. L., Rempel, M., Lagg, A., and Solanki, S. K.: 2018, *The Astrophysical Journal* **852(2)**, 66

Sobotka, M., Brandt, P. N., and Simon, G. W.: 1999, *A&A* **348**, 621

Solanki, S. K.: 1987, *Ph.D. thesis*, Max Planck Institute for Solar System Research, Justus-von-Liebig-Weg 3, 37351 Göttingen, Germany

Solanki, S. K.: 2003, *A&A Rev.* **11(2-3)**, 153

Solanki, S. K., Rüedi, I. K., and Livingston, W.: 1992, *A&A* **263(1-2)**, 312

Spruit, H. C.: 1976, *Sol. Phys.* **50(2)**, 269

Spruit, H. C.: 1981, in L. E. Cram and J. H. Thomas (eds.), *The Physics of Sunspots*, pp 98–103

Stein, R. F. and Nordlund, Å.: 1998, *ApJ* **499(2)**, 914

Steiner, O.: 2005, *A&A* **430**, 691

Steiner, O., Salhab, R., Freytag, B., Rajaguru, P., Schaffenberger, W., and Steffen, M.: 2014, *PASJ* **66**, S5

Steiner, O., Salhab, R., Freytag, B., Rajaguru, P., Schaffenberger, W., and Steffen, M.: 2014, *Publications of the Astronomical Society of Japan* 66(SP1), S5

Strassmeier, K. G.: 2009, *A&A Rev.* **17(3)**, 251

Strassmeier, K. G.: 2009, *The Astronomy and Astrophysics Review* **17(3)**, 251

Strassmeier, K. G. and Rice, J. B.: 1998, *A&A* **330**, 685

Strassmeier, K. G., Rice, J. B., Wehlau, W. H., Vogt, S. S., Hatzes, A. P., Tuominen, I., Piskunov, N. E., Hackman, T., and Poutanen, M.: 1991, *A&A* **247**, 130

Strassmeier, K. G., Welty, A. D., and Rice, J. B.: 1994, *A&A* **285**, L17

Thomas, J. H. and Weiss, N. O.: 1992, *The Theory of Sunspots*, pp 3–59, Springer Netherlands, Dordrecht

Tiwari, S. K., van Noort, M., Lagg, A., and Solanki, S. K.: 2013, *A&A* **557**, A25

Tiwari, S. K., van Noort, M., Solanki, S. K., and Lagg, A.: 2015, *A&A* **583**, A119

Toriumi, S., Katsukawa, Y., and Cheung, M. C. M.: 2015, *ApJ* **811(2)**, 137

Trampedach, R., Asplund, M., Collet, R., Nordlund, Å., and Stein, R. F.: 2013, *ApJ* **769(1)**, 18

van Noort, M., Lagg, A., Tiwari, S. K., and Solanki, S. K.: 2013, *A&A* **557**, A24

Vögler, A., Shelyag, S., Schüssler, M., Cattaneo, F., Emonet, T., and Linde, T.: 2005, *A&A* **429**, 335

Vogt, S. S.: 1981a, *ApJ* **250**, 327

Vogt, S. S.: 1981b, *ApJ* **250**, 327

Vogt, S. S., Hatzes, A. P., Misch, A. A., and Kürster, M.: 1999, *ApJS* **121(2)**, 547

Vogt, S. S. and Penrod, G. D.: 1983, *Publications of the Astronomical Society of the Pacific* **95**, 565

Vogt, S. S. and Penrod, G. D.: 1983, *PASP* **95**, 565

von Klüber, H.: 1948, *ZAp* **24**, 121

Wang, J. and Zhong, Z.: 2018, *A&A* **619**, L1

Watanabe, H.: 2014, *PASJ* **66**, S1

Watson, F. T., Fletcher, L., and Marshall, S.: 2011, *A&A* **533**, A14

Wedemeyer, S., Ludwig, H. G., and Steiner, O.: 2013, *Astronomische Nachrichten* **334**, 137

Westendorp Plaza, C., del Toro Iniesta, J. C., Ruiz Cobo, B., Martinez Pillet, V., Lites, B. W., and Skumanich, A.: 1997, *Nature* **389**, 47

Wilson, P. R. and Cannon, C. J.: 1968, *Sol. Phys.* **4(1)**, 3

Wray, A. A., Bensassi, K., Kitiashvili, I. N., Mansour, N. N., and Kosovichev, A. G.: 2015, *arXiv e-prints* p. arXiv:1507.07999

Zakharov, V., Hirzberger, J., Riethmüller, T. L., Solanki, S. K., and Kobel, P.: 2008, *A&A* **488(2)**, L17

# Appendix

# A Mass-Luminosity-Temperature Relations

In this chapter I will present the derivation of the mass-luminosity relation (eqn: 1.3) given in the Introduction of this thesis. I will do order-of-magnitude (OOM) calculations on two stellar structure equations- hydrostatic balance and energy transport to arrive at our result. This derivation has been reproduced from Choudhuri (2010).

The hydrostatic balance equation can be written as

$$\frac{dP}{dr} = \frac{-GM_{\rm r}}{r^2}\rho. \tag{A.1}$$

After OOM approximations we can rewrite A.1 as,

$$\frac{P}{R} \propto \frac{M}{R^2}\rho.$$

Plugging in $\rho \propto \frac{M}{R^3}$ we get

$$P \propto \frac{M^2}{R^4}. \tag{A.2}$$

From the equation of state $P \propto \rho T$ we can write

$$P \propto \frac{M}{R^3}T. \tag{A.3}$$

From A.2 and A.3 we can write

$$\frac{M}{R^3}T \propto \frac{M^2}{R^4},$$

$$\implies T \propto \frac{M}{R}.$$

The energy transport equation in a radiative stellar interior is written as:

$$\frac{dT}{dR} = \frac{3\chi\rho L_{\rm r}}{4a_{\rm b}T^3 4\pi r^2}. \tag{A.4}$$

After OOM approximations we get:

$$\frac{T}{R} \propto \frac{M}{R^3T^3}\frac{L}{R^2},$$

$$\implies L \propto \frac{(TR)^4}{M}.$$

Putting in $T \propto \frac{M}{R}$ we get,

$$L \propto M^3. \tag{A.5}$$

# B 2D simulations of starspots

The appendix details the results of our 2D simulations which we used to explore the parameter space more extensively. As discussed before, the two parameters that determine the shape of our flux tubes are the vertical components of the magnetic field at the lower boundary and at the optical surface - $B_{\rm bot}$ and $B_{\rm opt}$. The initial conditions used for the 2D simulations were the 2D analogs of the conditions used for the 3D runs. Table B.1 summarizes our 2D runs. Figure B.1 shows the vertical velocity field before the magnetic field is put in. The upflow areas are in yellow and the downflow areas are in blue. Figure B.2 shows an example of a magnetic field configuration inserted into the hydrodynamic simulation.

## B.1 Selecting the umbra

We have selected the umbral region using two different methods. In the first method we simply set thresholds for the intensity and magnetic field strengths, and all points that satisfy the criteria are considered to be part of the umbra. We set a threshold of 1500 Gauss for the magnetic field strength in all three stars. For the G2V and K0V spots we used a relative intensity threshold of $I_{Umbra}/I_{Quiet} < 0.5$. Since in the M0V spot there were no regions with such low intensities we chose a threshold of $I_{Umbra}/I_{Quiet} < 0.75$. This method which chooses just those points that satisfy the above mentioned criteria excludes the peaks in the intensity inside the spot region as seen in Figure B.3. These intensity peaks seem to be the 2D equivalent of umbral dots. However they are significantly larger and brighter than umbral dots typically seen in 3D simulations. The second method of selecting the umbral region does not ignore these intensity peaks. We choose the first point and last point that satisfy the thresholds and take all points in between as shown in Figure B.4.
Once we have chosen the umbra we average the properties over space and time, such that several granule lifetimes are covered. Each spot was averaged over a few hours.
In all of the plots from B.5 to B.10, the data points in blue exclude the umbral dots, and the data points in red include the umbral dots. The error bars show the standard deviation of the computed spatio-temporal averages.

Table B.1: Summary of the results of the 2D runs.

| Sp. Type | $B_{\rm opt}$ (kG) | $B_{\rm bot}$ (kG) | $I_{umbra}/I_{quiet}$ | $\lvert B\rvert_{\rm umbra}$(kG) |
|---|---|---|---|---|
| G2V | 2.2 | 4 | 0.22, 0.30 | 4.15, 4.00 |
| | 2.2 | 6 | 0.22, 0.27 | 4.70, 4.58 |
| | 2.2 | 8 | 0.18, 0.20 | 5.07, 5.03 |
| | 2.2 | 10 | 0.20, 0.22 | 4.89, 4.84 |
| | 2.2 | 12 | 0.19, 0.23 | 4.95, 4.87 |
| | 2.2 | 14 | 0.19, 0.22 | 5.16, 5.06 |
| | 4.4 | 12 | 0.18, 0.19 | 4.82, 4.78 |
| | 8.8 | 12 | 0.19, 0.19 | 4.98, 4.96 |
| K0V | 3.2 | 6 | 0.34, 0.40 | 4.32, 4.16 |
| | 3.2 | 8 | 0.35, 0.39 | 4.45, 4.23 |
| | 3.2 | 10 | 0.34, 0.38 | 4.22, 4.07 |
| | 3.2 | 12 | 0.33, 0.47 | 4.25, 3.74 |
| | 3.2 | 14 | 0.32, 0.35 | 4.43, 4.33 |
| | 3.2 | 16 | 0.33, 0.37 | 4.33, 4.24 |
| | 6 | 16 | 0.32, 0.33 | 4.57, 4.52 |
| | 12 | 16 | 0.32, 0.35 | 4.53, 4.43 |
| M0V | 3.0 | 5 | 0.68, 0.74 | 4.50, 4.03 |
| | 3.0 | 8 | 0.67, 0.69 | 4.66, 4.54 |
| | 3.0 | 10 | 0.67, 0.69 | 4.91, 4.76 |
| | 3.0 | 12 | 0.68, 0.71 | 5.06, 4.87 |
| | 3.0 | 15 | 0.66, 0.69 | 5.30, 5.05 |
| | 3.0 | 18 | 0.66, 0.71 | 5.40, 4.82 |
| | 6 | 15 | 0.65, 0.69 | 5.36, 5.01 |
| | 12 | 15 | 0.65, 0.67 | 5.57, 5.42 |

The numbers in black indicate averages computed using simple intensity and magnetic field thresholds to define umbral regions.The numbers in red indicate averages computed without ignoring the sharp intensity peaks seen in the umbral regions of our 2D spot simulations. See A.1 for more details.

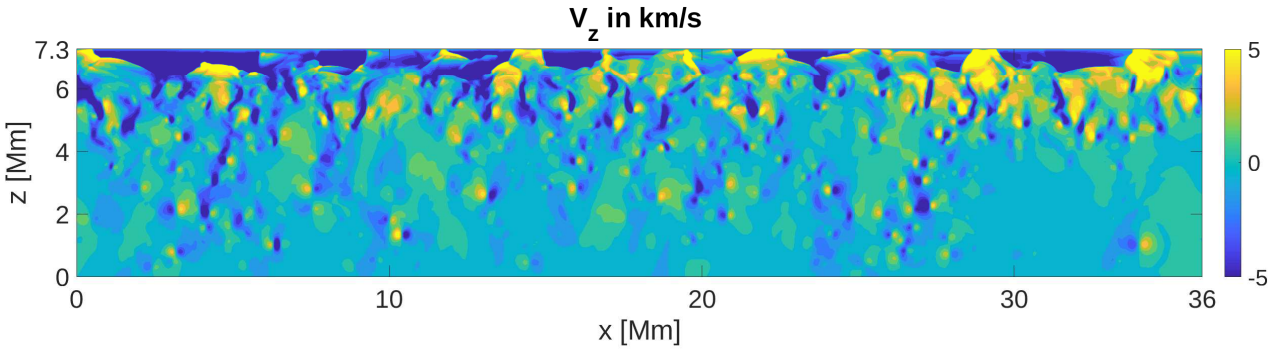


Figure B.1: Vertical velocity in the 2D simulation setup before the magentic field was introduced. The colors show $V_z$ in km $s^{-1}$.

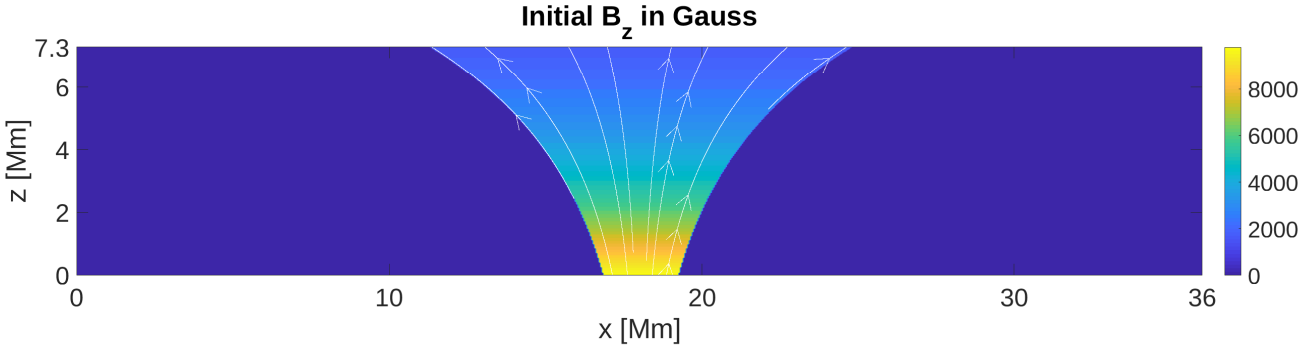


Figure B.2: Initial magnetic field configuration for a 2D G2V spot simulation. The colors show $B_z$ in Gauss and the white lines with arrows mark sample magnetic field lines.

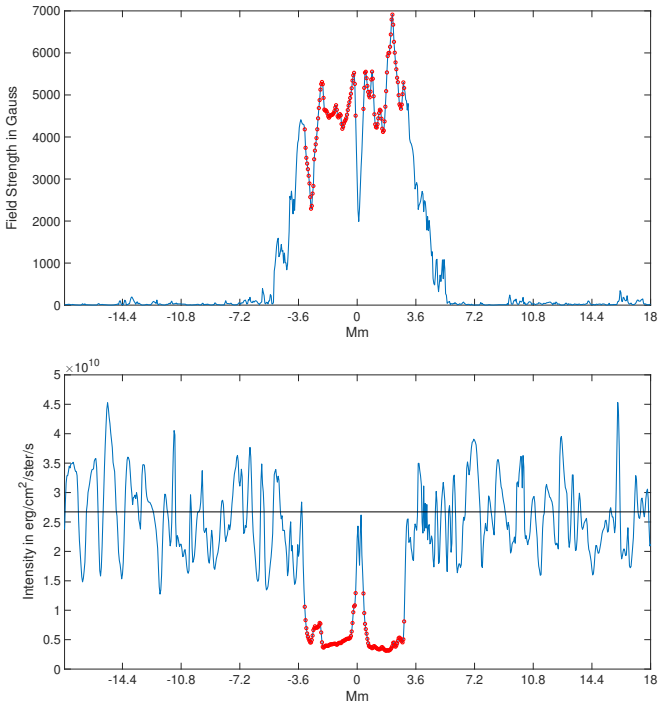


Figure B.3: Umbral field strength at the optical surface and bolometric intensity for a sample G2V spot. The parts in red mark the region defined as the umbra. This definition of the umbra excludes the spike observed in both the intensity and field strength. The black horizontal line represents the average quiet star intensity.

## B.2 Varying $B_{\rm bot}$

For this numerical experiment, we chose a $B_{\rm opt}$ of 2.2 kiloGauss for the G2V spots and slightly higher field strengths of 3.2 kiloGauss and 3 kiloGauss for the K0V and M0V starspots respectively, and varied $B_{\rm bot}$, the field strength at the lower boundary. The choices for $B_{\rm opt}$ were motivated by the fact that average sunspots have field strengths in the 2-3 KiloGauss range, and we began with the assumption that starspot field strengths would not be drastically different.

Plotted in Figure B.5 is the variation in $I_{Umbra}/I_{Quiet}$ with $B_{\rm bot}$ for the all three stars. The initial $B_{\rm opt}$ was the same for spots of the same spectral type. It is clear, in all three spectral types, that the relative intensity of the spots does not have a clear dependence on the field strength at the lower boundary especially when we do not consider the umbral dots. Naturally, the cases where we do not consider the umbral dots (marked in blue) have lower relative intensities. In none of the cases, the $I_{Umbra}/I_{Quiet}$ ratio changes by more than 0.1 even when $B_{\rm bot}$ is changed by a factor of 3.

Figure B.6 shows the variation of the magnetic field strength, finally obtained at the optical surface, with initial $B_{\rm bot}$. Like the relative intensity, this shows no significant dependence on the initially chosen $B_{\rm bot}$. In the G2V case, after an increase in the first 3 cases (i.e. from $B_{\rm bot}$ = 4 kG to 8 kG), the final umbral field strength ceases to be sensitive to an increase in $B_{\rm bot}$. When the field strength at the lower boundary is too weak, we get a lot more spikes in the intensity which weakens the umbral field strength. When we

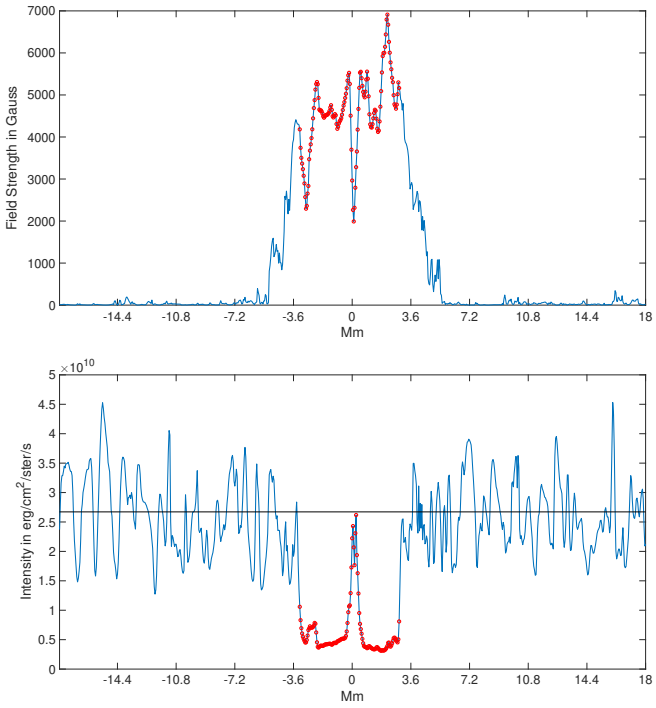


Figure B.4: Umbral field strength at the optical surface and bolometric intensity for the G2V spot shown in Fig. B.3 . The parts in red mark the region defined as the umbra. This definition of the umbra includes the spike observed in both the intensity and field strength. The black horizontal line represents the average quiet star intensity.

increase $B_{\rm bot}$, the spikes in the intensity become rarer and the magnetic field is largely determined by the surface pressure. The M0V spots show the maximum dependence on $B_{\rm bot}$ as seen in the lower panel of Figure 27. The magnetic pressure forces the field lines to fan out until they experience pushback from the ambient gas and the balance between magnetic pressure and fluid pressure determines the umbral field strength. In the case of the M0V star, owing to the pressure scale heights being very small, the vertical extent of the box is only 1.3 Mm compared to the 7.3 Mm of the 2D G2V box. The sharp drop in magnetic field strength with height means that the field lines of the M0V spots are already highly fanned out and the resulting magnetic tension limits how much they can fan out further. Nevertheless, the dependence is marginal, as the final field strength increases by only 25% even when $B_{\rm bot}$ is increased by a factor of 3.6.

Figure B.7 shows the dependence of spot relative intensity on the final magnetic strength obtained at the optical surface. We see that for the G2V spot, the spots become darker with an increase in the photospheric field strength. However for the cooler K0 and M0 spots, the spot brightness shows no decrease with an increase in surface field strength. This is consistent with the fact the radiation plays a more important role in energy transport in the cooler K0 and M0 stars, thereby making the brightness of the spot less dependent on magnetic field strength.

Although the relative intensities of the 2D spots are 5-10 % lower than their 3D counterparts in all three stellar types, the decrease in spot relative intensity with stellar surface temperature is very well reproduced.

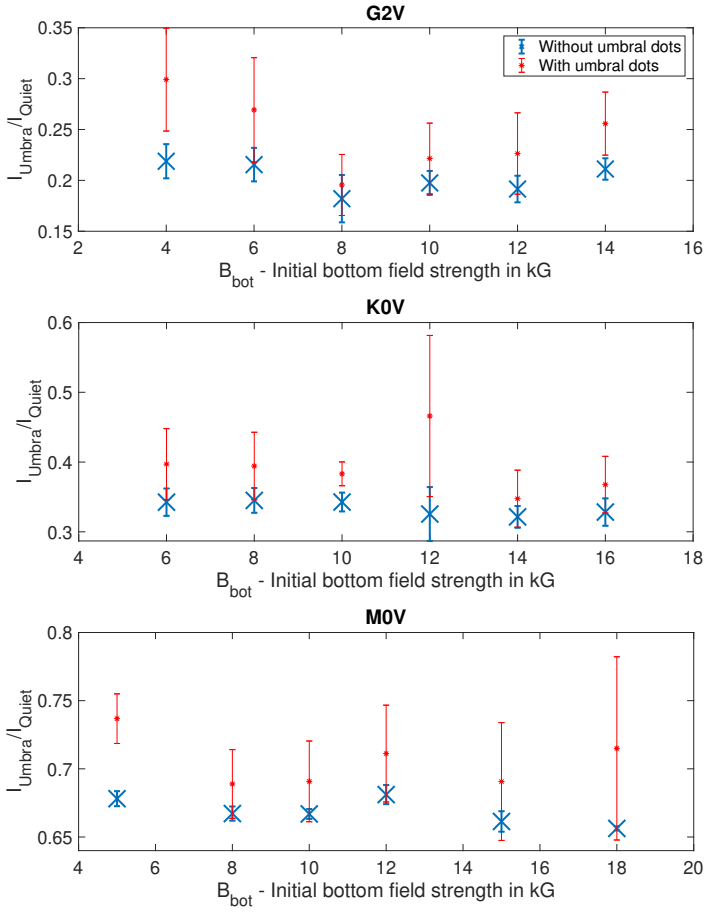


Figure B.5: Relative intensity of spots plotted against initial field strengths at the lower boundary. Top to bottom: G2V, K0V and M0V. Red: with umbral dots. Blue: without umbral dots.

## B.3 Varying $B_{\mathrm{opt}}$

Our very limited knowledge about surface field strengths on other stars, and the fact that M0V and K0V have higher surface pressures, prompted us to conduct further runs, where we kept the field strengths at the lower boundary ($B_{\mathrm{bot}}$) constant and increased the initial field strengths at the optical surface ($B_{\mathrm{opt}}$).

For all of the spectral types we increased the initial $B_{\mathrm{opt}}$ to 2 and 4 times the magnitude used in our studies where we varied $B_{\mathrm{bot}}$. The $B_{\mathrm{bot}}$ used was 12 kiloGauss for the G2V runs, 16 kiloGauss for the K0V runs, and 15 kiloGauss for the M0V runs. We found that despite increasing the initial $B_{\mathrm{opt}}$ by a factor of 4, there is little change in the final relative intensity and magnetic field strength at the surface. This holds for all of the simulated stars as shown in Figures B.8, B.9 and B.10.

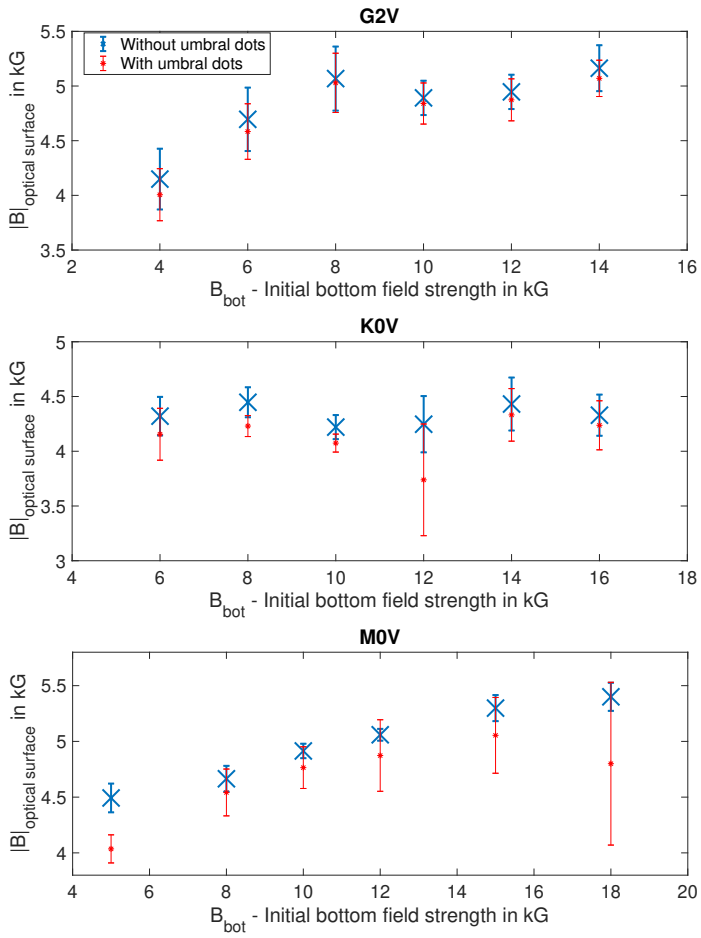


Figure B.6: Final umbral field strength at the optical surface plotted against initial field strengths at the lower boundary. Top to bottom: G2V, K0V and M0V. Red: with umbral dots. Blue: without umbral dots.

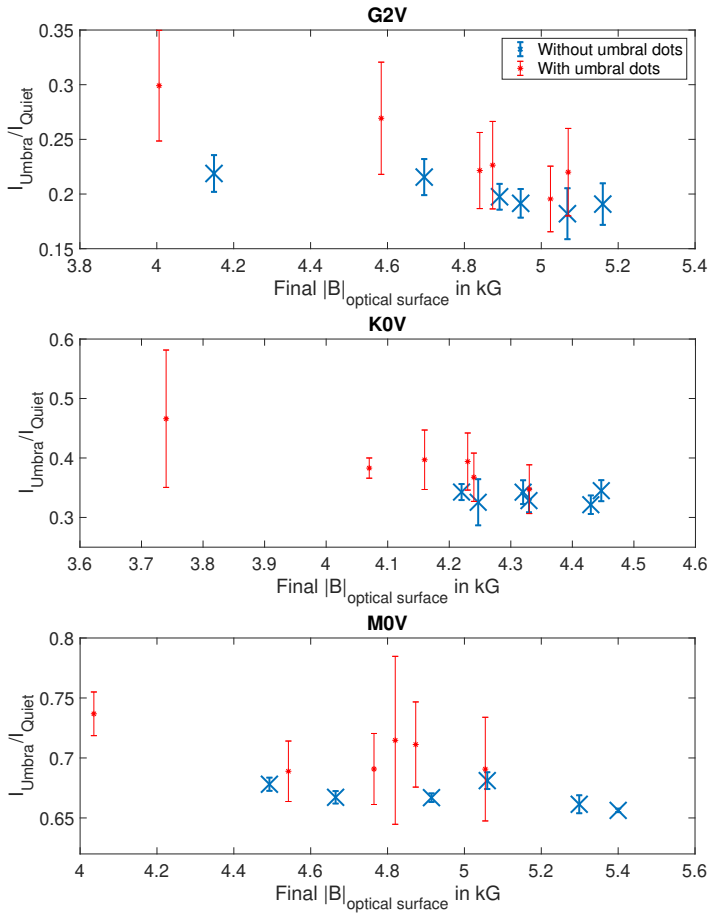


Figure B.7: Relative intensity of spots plotted against final umbral field strengths at the optical surface. Top to bottom: G2V, K0V and M0V. Red: with umbral dots. Blue: without umbral dots.

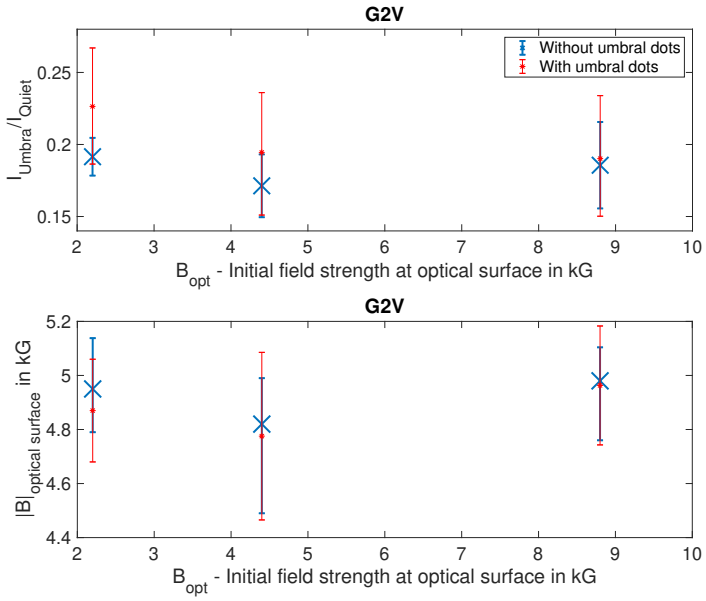


Figure B.8: Both plots are for the G2V star. Relative intensity of spots (upper panel) and their final umbral field strengths (lower panel) plotted against initial field strengths at the optical surface. Red: with umbral dots. Blue: without umbral dots.

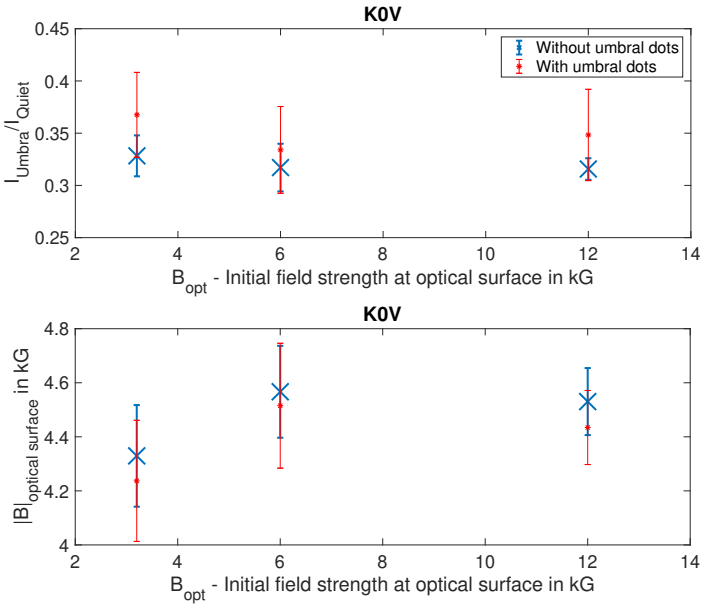


Figure B.9: The same as Figure B.8 but for the K0V star

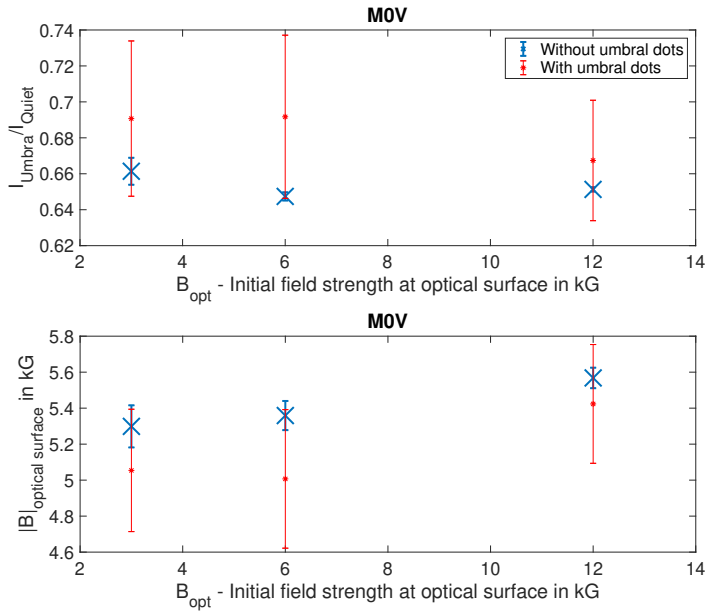


Figure B.10: The same as Figure B.8 but for the M0V star

# Publications

## Refereed publications

- *3D Radiative MHD simulations of starspots.*
  **Mayukh Panja**, Robert Cameron, Sami K. Solanki 2020 ApJ 893 113
- *Sunspot simulations: penumbra formation and the fluting instability*
  **Mayukh Panja**, Robert Cameron, Sami K. Solanki 2021 ApJ 907 102

## Conference contributions

- What do starspots look like? - Talk
  *Cool Stars 2018, Boston, USA*
- Spectral synthesis of simulated starspots - Talk
  *Solar Polarization Workshop 9, Göttingen, Germany*
- Radiaitve MHD simulations of starspots - Poster
  *IAUS 354: Solar and Stellar Magnetic Fields: Origins and Manifestations, Copiapo, Chile*

# Acknowledgements

I will attempt to list the people who made the completion of this thesis and my life infinitely easier -

- My supervisors Robert and Sami. Their suggestions and their vast experience greatly improved the quality of my work and my ability to communicate scientific results effectively. Robert's advice to tell a nice story came in handy when writing papers. Sami often reminded me that simulations ought to be constrained by observations.
- Sonja made both the on-boarding and de-boarding processes very smooth, taking care of many administrative hurdles.
- Pradeep, Jörn, Damien, Cosima, Sudarshan, Ameya, Sihane, Sabrina, and Cilia, with who I had many discussions (often fruitful) on science and life surrounding science. Each of them broadened my horizons with their unique perspectives. Pradeep, who seems to know almost everything, was my go-to-guy during the initial stages of my PhD.
- Cosima very generously translated the summary presented at the beginning of this thesis to German.
- Franziska and Felix, for patiently answering my million questions about the submission process. Franziska unselfishly helped me with adjusting to life in Germany.
- Tal encouraged and helped me transition to Python. Some of the figures in this thesis benefited from her graphics designing skills. Our many discussions about the nuances of writing science were enlightening.

I acknowledge support by the International Max-Planck Research School (IMPRS) for Solar System Science at the University of Göttingen.